The relative contributions of muscle deformation and ischaemia to pressure ulcer development

Document Version:
Publisher's PDF, also known as Version of Record (includes final page, issue and volume numbers)

Please check the document version of this publication:

• A submitted manuscript is the version of the article upon submission and before peer-review. There can be important differences between the submitted version and the official published version of record. People interested in the research are advised to contact the author for the final version of the publication, or visit the DOI to the publisher's website.
• The final author version and the galley proof are versions of the publication after peer review.
• The final published version features the final layout of the paper including the volume, issue and page numbers.

[Link to publication](#)

The relative contributions of muscle deformation and ischaemia to pressure ulcer development

The relative contributions of muscle deformation and ischaemia to pressure ulcer development

PROEFSCHRIFT

door

Sandra Loerakker

geboren te Alkmaar

Dit proefschrift is goedgekeurd door de promotoren:

prof.dr.ir. F.P.T. Baaijens
en
prof.dr. D.L. Bader

Copromotor:
dr.ir. C.W.J. Oomens

Contents

Summary

The relative contributions of muscle deformation and ischaemia to pressure ulcer development

Pressure ulcers are localised areas of soft tissue breakdown that develop over bony prominences as a result of sustained mechanical loading. They are particularly common in bedridden and wheelchair-bound individuals, and represent one of the most common secondary complications in spinal cord injured subjects. A specific form of pressure ulcers is termed deep tissue injury (DTI), which is defined as pressure-related injury to subcutaneous tissues such as skeletal muscle, initially under intact skin. DTI represents a severe problem, because tissue damage at the skin surface only becomes apparent at an advanced stage, and is associated with a variable prognosis. Therefore, early identification and subsequent treatment of DTI are critical to reduce comorbidities and the financial and manpower burdens associated with treatment. This requires a better understanding of its underlying aetiology, in order to develop appropriate risk assessment tools and early detection methods. Therefore, the main goal of the present thesis was to study the aetiology of DTI. In addition, some explorative studies were performed to examine potential methods for the early detection of DTI.

The aetiological factors were investigated using a combination of experiments and numerical models. This involved an established rat model for DTI that has previously been used to study the effects of deformation due to 2 h continuous loading. In the present thesis, different loading regimens were applied to further investigate the role of deformation. In addition, a previously developed finite element model to estimate muscle deformations during loading, was substantially improved to enable a local comparison of

deformation with damage. Furthermore, the duration of the experiments was extended to 6 h to investigate the effects of ischaemia and reperfusion. It was found that deformation is the primary trigger for muscle damage for loading periods up to 2 h when a specific deformation threshold is exceeded. Ischaemia started to cause changes in muscle tissue between 2-4 h loading. Therefore, the damage development in skeletal muscle during prolonged loading is determined by deformation, ischaemia, and reperfusion, each mechanism exhibiting a unique time profile. The developed methods were also applied to a porcine model for DTI to investigate the deformations of the different soft tissues of the buttocks during loading. In this study, it was shown that the relative mechanical properties of the different tissue layers have a large influence on the distribution of the internal deformations.

The release of biochemical damage markers from injured muscle tissue into the circulation was studied to investigate the possibility of using these proteins for the early detection of DTI. Baseline variations of creatine kinase, myoglobin, heart-type fatty acid binding protein, and C-reactive protein were assessed in able-bodied and spinal cord injured human volunteers. These variations were small compared to the predicted increase in biomarker concentrations during DTI development, indicating that this combination of markers may prove appropriate for the early detection of DTI. Moreover, a considerable increase in myoglobin concentrations in blood and urine was observed in a rat model for DTI after 6 h mechanical loading.

The present findings have implications for clinical practice. In particular, it is important to minimise the internal tissue deformations in subjects at risk of DTI, such as present in subjects with spinal cord injury and those positioned on hard surfaces, such as stretchers or operating tables, for prolonged periods. Furthermore, the period of loading should be limited to prevent the accumulation of ischaemic damage. The observation of increased myoglobin levels in blood and urine after mechanical loading demonstrates the potential of using biochemical markers of muscle damage for the early detection of DTI. Moreover, the increase of myoglobin levels in urine suggests that a noninvasive approach for this screening method may be satisfactory.

Samenvatting

De relatieve bijdragen van deformatie en ischemie in spier-weefsel aan de ontwikkeling van doorligwonden

Doorligwonden, ook wel aangeduid als drukwonden of decubitus, zijn lokale beschadigingen van zachte weefsels in de nabijheid van botuitsteeksels, die worden veroorzaakt door aanhoudende mechanische belasting. Doorligwonden komen veel voor bij mensen die bedlegerig zijn of gebonden aan een rolstoel, en behoren tot de meest voorkomende complicaties bij mensen met een dwarslaesie. Diepe weefselschade (Engelse term: deep tissue injury (DTI)) is een specifieke vorm van decubitus, en is gedefinieerd als druk-gerelateerde beschadiging van dieper gelegen weefsels, zoals de skeletspier, waarbij de huidlaag intact is. DTI is een ernstig probleem, omdat weefselschade vaak pas zichtbaar wordt aan het huidoppervlak op het moment dat de schade in een vergevorderd stadium is. Een vroegtijdige ontdekking en behandeling van DTI is daarom zeer belangrijk om complicaties te voorkomen, en om de hoge kosten voor de gezondheidszorg en de belasting van het verplegend personeel te verminderen. Voor het ontwikkelen van geschikte methoden voor de risicoanalyse en vroege detectie van DTI is het belangrijk om een beter begrip te krijgen van de onderliggende schademe-chanismen. Het voornaamste doel van dit proefschrift was daarom het bestuderen van de schademechanismen van DTI. Daarnaast is door middel van een aantal exploratieve studies de mogelijkheid van vroegtijdige opsporing van DTI onderzocht.

De verschillende schademechanismen zijn bestudeerd met een combinatie van experi-menten en numerieke modellen. Hiervoor is een ratmodel voor DTI ingezet, dat al eerder gebruikt is om het effect van deformatie tijdens 2 h continue belasting te bestuderen. In

het huidige proefschrift zijn verschillende soorten belasting opgelegd om de rol van deformatie beter te begrijpen. Voor een gedetailleerde lokale vergelijking van deformatie en schade is gebruik gemaakt van een sterk verbeterd eindige-elementenmodel. Vervolgens is de totale duur van de experimenten verhoogd tot 6 h om de effecten van ischemie en reperfusie te onderzoeken. De resultaten lieten zien dat deformatie de belangrijkste factor voor het onstaan van spierschade is voor belastingen tot 2 h wanneer een specifieke deformatiedrempel wordt overschreden. Ischemie veroorzaakte veranderingen in het weefsel na 2-4 h belasting. De schadeontwikkeling in spierweefsel tijdens langdurige belasting wordt dus bepaald door deformatie, ischemie, en reperfusie, waarbij elk mechanisme zijn eigen karakteristieke tijdsprofiel heeft. De ontwikkelde methoden zijn ook toegepast op een varkensmodel voor DTI om de deformaties in de verschillende weefsellagen onder de zitbeenderen te onderzoeken. De resultaten van deze studie lieten zien dat de relatieve stijfheden van de verschillende weefsellagen een grote invloed hebben op de verdeling van de interne deformaties.

De afgifte van biochemische markers voor spierschade in de bloedbaan is bestudeerd om de toepasbaarheid van deze eiwitten voor de vroege detectie van DTI te onderzoeken. De basale variaties van creatine kinase, myoglobine, heart-type fatty acid binding protein, en C-reactive protein zijn gemeten in vrijwilligers met en zonder dwarslaesie. Deze variaties waren klein ten opzichte van de verwachte stijging in markerconcentraties tijdens de ontwikkeling van DTI, wat aangeeft dat deze combinatie van markers potentie heeft voor de vroegtijdige opsporing van DTI. Bovendien is ook een aanzienlijke toename in myoglobineconcentratie gemeten in zowel bloed als urine in een ratmodel voor DTI na 6 h mechanische belasting.

Deze resultaten hebben implicaties voor de klinische praktijk. Het is belangrijk om de interne weefseldeformaties te minimaliseren bij mensen die een hoog risico hebben op DTI, zoals mensen met een dwarslaesie en personen die langdurig op harde oppervlakken zoals brancards en operatietafels liggen. Daarnaast is het van belang om de belastingsduur te beperken, zodat de ontwikkeling van ischemische schade kan worden voorkomen. De verhoogde myoglobinewaarden in bloed en urine na mechanische belasting tonen aan dat biochemische markers voor spierschade wellicht gebruikt kunnen worden om DTI in een vroeg stadium op te sporen. De verhoogde waarden in urine geven bovendien aan dat het mogelijk moet zijn om een noninvasieve screeningsmethode te ontwikkelen.

Chapter 1

General introduction

1.1   Pressure ulcers

A pressure ulcer is a localised injury to the skin and/or underlying tissue, usually over a bony prominence, as a result of pressure, or pressure in combination with shear (NPUAP and EPUAP, 2009). Pressure ulcers can occur in situations where people are subjected to sustained mechanical loads, and are particularly common in subjects who are bedridden or wheelchair-bound. Prevalence figures remain high (Bours et al., 2002; Schoonhoven et al., 2007), and the treatment of pressure ulcers and related complications represents a financial and human burden in terms of extended hospitalisation and possible surgical interventions (Bennett et al., 2004; Brem et al., 2010). Spinal cord injured individuals are particularly at risk of developing pressure ulcers, which can seriously affect their quality of life. The occurrence of pressure ulcers is a major secondary complication in this population (McKinley et al., 1999; Garber and Rintala, 2003). In addition, a large proportion of ulcers in this population are severe involving deep tissues (Garber and Rintala, 2003), and are associated with poor healing and a high recurrence rate (Rintala et al., 2008; Bates-Jensen et al., 2009).
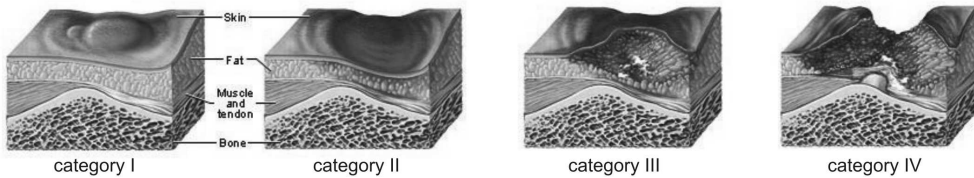
Figure 1.1: Schematic representation of the four categories of pressure ulcers used in Europe. A category I ulcer is characterised by a discoloration of the skin, a category II ulcer by partial loss in thickness of the skin, a category III ulcer by full loss in thickness of the skin, and a category IV ulcer by extensive destruction of muscle, bone, or supporting structures with or without full loss in the thickness of the skin.

Classification systems are used to define the severity of a pressure ulcer regarding the anatomical depth of the injury. Recently, a common international definition and classification system was proposed by the European Pressure Ulcer Advisory Panel (EPUAP) and the American National Pressure Ulcer Advisory Panel (NPUAP) (NPUAP and EPUAP, 2009). A brief description of the different categories is given in table 1.1. Category I and II represent superficial ulcers involving the skin, whereas deep ulcers involving fat or muscle tissue are labelled as category III or IV (figure 1.1). Pressure ulcers can originate at the skin surface and progress toward deeper tissues, but they can also start in deep tissues underneath an intact skin and progress outward. Indeed, in several studies tissue damage due to compression was observed primarily in the muscle tissue as opposed to the skin (Nola and Vistnes, 1980; Daniel et al., 1981; Salcido et al., 1994). This type of injury was recently defined as pressure-related deep tissue injury (DTI) (Ankrom

et al., 2005; Black et al., 2007), and is considered a separate category of pressure ulcers in the United States (table 1.1). The prevalence of DTI is relatively low when compared to other pressure ulcer categories, although the real prevalence may be underestimated due to difficulties in identifying DTI (Kottner et al., 2010; VanGilder et al., 2010). Nevertheless, it represents a severe problem, because tissue damage at the skin surface only becomes apparent at an advanced stage, at which time treatment becomes problematic and several complications can occur (Thomas, 2001; Brem et al., 2010). Therefore, early identification and subsequent treatment of DTI are critical to reduce comorbidities and costs. This requires a better understanding of its underlying aetiology, in order to develop appropriate risk assessment tools and early detection methods. Accordingly, the focus of the present thesis is on the aetiology and early detection of DTI.

Table 1.1: International classification system for pressure ulcers (NPUAP and EPUAP, 2009).

Category	Description
Category I	Intact skin with non-blanchable redness of a localised area usually over a bony prominence. The area may be painful, firm, soft, warmer or cooler as compared to adjacent tissue.
Category II	Partial thickness loss of dermis presenting as a shallow open ulcer with a red pink wound bed, without slough. May also present as an intact or open/ruptured serum-filled blister.
Category III	Full thickness tissue loss. Subcutaneous fat may be visible but bone, tendon, or muscle are not exposed.
Category IV	Full thickness tissue loss with exposed bone, tendon, or muscle. Slough or eschar may be present.
Unstageable/ unclassified[1]	Full thickness tissue loss in which the base of the ulcer is completely obscured by slough and/or eschar in the wound bed.
Suspected deep tissue injury[1]	Purple or maroon localised area of discoloured intact skin or blood-filled blister due to damage of underlying soft tissue from pressure and/or shear. The area may be preceded by tissue that is painful, firm, mushy, boggy, warmer or cooler as compared to adjacent tissue. Evolution may be rapid, exposing additional layers of tissue even with optimal treatment.

[1]Category used in the United States.

1.2   Mechanical loading of soft tissues

Mechanical loading that can lead to the development of pressure ulcers involves pressure, or pressure in combination with shear and/or friction. The distribution of the load plays an important role. As an example, uniformly distributed loads on the skin surface, e.g. during deep-sea diving, are unlikely to cause tissue damage (Neumark, 1981; Bliss, 1993). By contrast, localised pressure causes tissue deformation and blockage of blood vessels, and is therefore far more damaging. The exposure time to a certain load is also an important factor for the development of tissue damage. Animal models have been used to investigate the combination of applied pressure and exposure time, which can lead to the development of pressure ulcers. In early studies, a hyperbolic relation was suggested for this risk curve (figure 1.2a), indicating that small loads applied for a long time can be as harmful for the tissue as a large load applied for a short period (Groth, 1942; Husain, 1953; Kosiak, 1959; Dinsdale, 1974; Daniel et al., 1981). In a retrospective study, a similar hyperbolic curve was also proposed for humans (Reswick and Rogers, 1976). More recently, however, an inverse sigmoidal shape has been suggested (figure 1.2b), implying that certain magnitudes of pressure can directly cause tissue damage (Linder-Ganz et al., 2006; Gefen et al., 2008; Stekelenburg et al., 2008; Gefen, 2009).
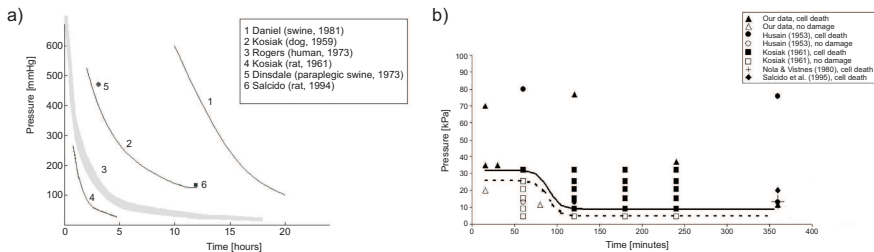
Figure 1.2: a) Hyperbolic risk curves for pressure ulcer development as derived from different studies (adapted from Stekelenburg et al. (2005)). In each study, combinations of pressure and time above the curve caused tissue damage. b) More recently, an inverse sigmoid curve has been suggested, implying that certain magnitudes of pressure can directly cause tissue damage (adapted from Linder-Ganz et al. (2006)).

Large differences are present between the risk curves that were derived in different studies (figure 1.2a), which may be attributed to differences in animal models and experimental conditions. In addition, the internal mechanical state in tissues is not solely determined by the external load, which makes it difficult to compare the different studies based on applied pressures per se. Indeed, numerical simulations demonstrated that the stress and strain distributions within loaded tissues are not uniform in nature, with considerably larger strains at locations adjacent to bony prominences when compared to

locations near the interface between the body and the support surface (Oomens et al., 2003; Linder-Ganz et al., 2007, 2008). In summary, interface pressures should not be used to predict conditions leading to DTI, since they do not provide information about the mechanical state of the deep tissue layers (Chow and Odell, 1978; Dabnichki et al., 1994; Gefen and Levine, 2007; Oomens et al., 2003, 2010).

1.3   Aetiology of DTI

Although it is clear that sustained mechanical loading is the primary cause of pressure ulcers, the underlying pathways whereby mechanical loading leads to tissue breakdown are not completely understood. At the moment, theories involve (Bouten et al., 2003; Mak et al., 2010):

- Compression-induced ischaemia;

- Ischaemia-reperfusion (I-R) injury;

- Impaired lymphatic drainage;

- Sustained tissue deformation.

Traditionally, compression-induced ischaemia is considered to represent the most important aetiological factor (Kosiak, 1959; Daniel et al., 1981). External pressures that are large enough to close blood vessels will cause a lack of oxygen and nutrients and an accumulation of metabolic waste products in the loaded tissue. The lack of oxygen and nutrients leads to disturbed intracellular ion concentrations, resulting in an increased permeability of the cell membrane and cell swelling (Rubin et al., 2005). In general, muscle tissue appears to be tolerant of ischaemia for up to 4 h, whereas fat tissue can tolerate ischaemia up to 13 h, and skin up to 24 h at normothermia (Blaisdell, 2002).

Reperfusion after an ischaemic period can reverse these effects by restoring tissue oxygen and nutrient levels, and removing waste products from the previously ischaemic tissue. However, reperfusion after prolonged ischaemia can also aggravate tissue damage due to the activation of reactive oxygen species, inflammation, and oedema. Indeed, it was shown in a rat model that, for a constant total period of ischaemia, intermittent I-R cycles caused more damage to the skin than continuous ischaemia alone (Peirce et al., 2000). Moreover, a separate study reported that muscle damage was less extensive after 2.5 h ischaemia if gradual reperfusion was used instead of instantaneous reperfusion (Ünal et al., 2001).

The lymphatic system returns large proteins and excess fluid volume from tissues to the circulation. Lymph vessels can collapse during tissue compression, causing an accumulation of waste products and an increase in interstitial fluid volume, which may also contribute to pressure ulcer development (Krouskop et al., 1978; Miller and Seale, 1981; Reddy and Cochran, 1981). There has been a dearth of studies related to this damage mechanism, mainly due to the limited number of appropriate noninvasive measurement techniques.

Tissue compression itself can also directly cause tissue damage and thereby contribute to the aetiology of pressure ulcers. In vitro studies showed that tissue damage in 20 % strained muscle constructs was more extensive than in unstrained controls (Bouten et al., 2001), and that the time period that muscle tissue can tolerate strain depends on the strain level (Gefen et al., 2008). Moreover, Gawlitta et al. (2007a,b) reported that deformation can lead to muscle damage within shorter time periods than hypoxia. The relative contributions of deformation and ischaemia were also investigated in an animal model in which the tibialis anterior muscle of rats was compressed for 2 h (Stekelenburg et al., 2007). The results of this study showed that muscle damage was only present in specific regions of the muscle, despite the fact that the complete muscle was ischaemic during loading. Numerical simulations of these experiments demonstrated that damage coincided with those regions subjected to the largest deformations (Ceelen et al., 2008b). Local tissue deformations can change with time due to a change in mechanical properties of the injured tissue. In a rat model, for example, muscle damage as a result of compression was accompanied by an increase in stiffness, which can subsequently increase local deformations and thereby muscle damage in the surrounding tissue (Linder-Ganz and Gefen, 2004; Gefen et al., 2005).

1.4   Risk assessment

The primary cause of pressure ulcers is the exposure to mechanical loading. However, the ability of an individual to withstand a period of loading determines whether or not a pressure ulcer will develop. The risk of developing pressure ulcers is determined by extrinsic and intrinsic factors, as schematically illustrated in figure 1.3. Examples of extrinsic factors include the temperature and humidity of the environment, and the support surface. For example, internal deformations are influenced by the type of wheelchair cushion (Shabshin et al., 2010) and sitting posture (Hobson, 1992). Intrinsic factors are related to the individual, e.g. age, nutritional state, body weight, and the presence of pathologies. An increase in body weight, for example, was suggested to cause an increase in internal stresses and strains (Elsner and Gefen, 2008; Sopher et al., 2010). The extrinsic and

intrinsic factors influence the mechanical loading conditions, the susceptibility of the individual, and the remodelling capacity of their tissues. The balance between these three factors determines the risk of pressure ulcer development.

As an example, spinal cord injury is associated with a range of events that increase the risk of developing pressure ulcers. One of these features is disuse muscle atrophy (Scelsi, 2001; Liu et al., 2008), which increases the internal deformations in load-bearing soft tissues (Linder-Ganz et al., 2008). In addition, the properties of the muscle tissue change, e.g. including an increase in lipid content, and a change in fibre type from I to II (Scelsi, 2001). These changes may alter the susceptibility of the tissue to mechanical loading and thereby influence the threshold for tissue damage. Moreover, many of the changes that occur upon spinal cord injury have a negative effect on the wound healing cascade, which also increases the risk of developing pressure ulcers (Rappl, 2008).
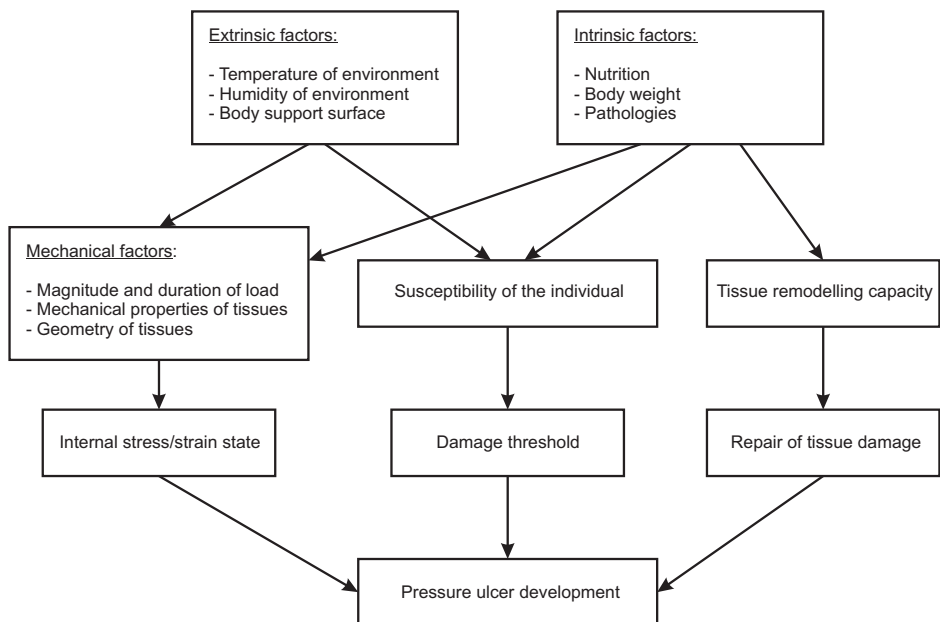
Figure 1.3: Schematic illustration of risk factors that influence pressure ulcer development (partly based on NPUAP and EPUAP (2009)).

1.5   Early detection of DTI

A major problem associated with DTI is that early identification is extremely difficult due to the continued presence of intact skin. In this way, tissue damage can often progress unnoticed by the insensate individual. Once the injury becomes apparent at the skin surface, healing is problematic and a range of complications can occur. Therefore, it is essential to develop a screening method to detect DTI at an early stage, to improve and accelerate healing, to prevent complications, and reduce the high treatment costs. Since DTI often affects the muscle tissue, such a screening method could be aimed at detecting skeletal muscle damage. A frequently used method to assess the presence of muscle damage, is to measure the levels of biochemical markers of muscle damage in blood or urine. If muscle damage occurs, a range of proteins leak out of the damaged fibres into the circulation, at a rate determined partly by their molecular size. Since tissue damage is usually followed by an inflammatory response, it is also useful to monitor the presence of inflammatory markers in blood or urine.

Many proteins have been used as an indirect measure of skeletal muscle damage after exercise, including creatine kinase (CK), myoglobin (Mb), and heart-type fatty acid binding protein (H-FABP) (Kuipers, 1994; Clarkson and Hubal, 2002). In a study with human volunteers, levels of CK, Mb, and H-FABP all increased after eccentric exercise (Sorichter et al., 1998). These markers have also been used to detect cardiac muscle damage. Skeletal muscle damage can be distinguished from cardiac muscle damage by calculating the ratio of Mb over H-FABP, which is considerably higher in case of skeletal muscle damage (20–70) when compared to cardiac muscle damage ($\sim$5) (Van Nieuwenhoven et al., 1995). In most studies, blood samples were obtained for the detection of increased biomarker levels. However, urine might also be used as a noninvasive alternative to detect increases in biomarker release (Volders et al., 1993).

Several studies have reported considerable increases in CK levels in serum and wound exudate in animal studies on DTI after 6 h mechanical loading (Hagisawa et al., 1988; Sari et al., 2008; Minematsu et al., 2010). Furthermore, higher serum levels of inflammatory marker C-reactive protein (CRP) were observed in spinal cord injured subjects with pressure ulcers than in subjects without ulcers (Scivoletto et al., 2004; Frost et al., 2005; Morse et al., 2008).

1.6   Rationale and outline

Spinal cord injured individuals thus have a large risk of developing pressure ulcers. In addition, a large proportion of these ulcers involve deep tissues, for which it is likely that tissue damage also originated at those locations. Therefore, it can be predicted that many pressure ulcers in this population involve DTI. It is essential to understand the underlying mechanisms of DTI, so that clinical methods can be developed to identify this condition at an early stage. Therefore, the goals of this thesis were to obtain a better understanding of the aetiology, and also to explore the possibility of using biochemical markers of muscle damage and inflammation for early detection of DTI. Since DTI often arises in the muscle tissue, the focus of this thesis was on the aetiology and early detection of pressure-induced skeletal muscle damage.

The aetiology was investigated using an animal model for DTI. Since the external mechanical load is not a good measure of the internal loading of the muscle, a finite element model was used to estimate the internal loading conditions in the muscle, which were subsequently compared with the degree of muscle damage. The following questions were addressed:

- Chapter 2: Which factors influence the ability of the finite element model to predict the in vivo deformation behaviour of skeletal muscle?

- Chapter 3: Is deformation the primary trigger for muscle damage for short loading periods?

- Chapter 4: When do ischaemia and reperfusion become involved in the damage process?

- Chapter 5: What are the relative contributions of deformation, ischaemia, and reperfusion in the aetiology of DTI?

- Chapter 6: How does muscle stiffness affect the internal tissue deformations in the buttocks during loading?

With reference to early identification of DTI, the following questions were addressed:

- Chapter 7: How large is the variation in baseline levels of biochemical markers of muscle damage and inflammation in able-bodied and spinal cord injured individuals?

- Appendix A: Is there a correlation between the amount of muscle damage and the biomarker concentrations in blood and urine?

Finally, chapter 8 presents a general discussion of the main findings and some recommendations for future research.

Chapter 2

Which factors influence the ability of a computational model to predict the in vivo deformation behaviour of skeletal muscle?

2.1   Introduction

Deep tissue injury (DTI) is a severe form of pressure ulcer where tissue damage starts in deep tissues, such as skeletal muscle, underneath intact skin. DTI constitutes a serious problem, particularly for the spinal cord injured, because tissue damage is often not detected until it has reached the skin surface, at which time treatment is problematic and associated with a range of complications (Thomas, 2001; Brem et al., 2010). The aetiology of DTI involves several factors, the most well established of which involves compression-induced ischaemia (Kosiak, 1959; Daniel et al., 1981). More recently, it has been suggested that local tissue deformations may also play an important role (Gawlitta et al., 2007a; Ceelen et al., 2008b; Linder-Ganz et al., 2008), especially within short loading periods when ischaemia is not expected to cause any significant muscle damage (Stekelenburg et al., 2007).

Finite element (FE) models with varying levels of sophistication can be used to better understand the underlying phenomena associated with the development of deformation-induced muscle damage and facilitate the interpretation of experiments. Using FE models with relatively simple geometries, it has been shown that the strain distribution in loaded tissues is highly heterogeneous in nature. Spatial analysis revealed larger stresses and strains in tissues underneath bony prominences compared to locations adjacent to the body-support interface (Chow and Odell, 1978; Todd and Thacker, 1994; Oomens et al., 2003). In more recent studies, patient-specific geometries were incorporated to investigate quantitative differences in the stress and strain distribution in the buttocks (Linder-Ganz et al., 2007, 2008).

In animal experiments of Bosboom et al. (2003), the effect of mechanical loading on the development of muscle damage was investigated by compressing the tibialis anterior (TA) muscle of rats with an indenter for 2 h. Muscle damage was evaluated with T_2-weighted magnetic resonance imaging (MRI) and histology. This revealed large differences in the amount and locations of muscle damage between the animals, partly due to the inability to reproduce the loading conditions between experiments. Therefore, an MR-compatible loading device was developed by Stekelenburg et al. (2006a) to improve the reproducibility by controlling the indentation depth, resulting in smaller differences in the amount of muscle damage. Nonetheless, considerable differences between the animals still existed. It was hypothesised that these differences in the degree of tissue damage were caused by differences in local internal deformations between animals. Animal-specific FE models were developed by Ceelen et al. (2008a,b) to simulate these experiments and estimate the internal strain distribution in the muscle tissue during loading. By using a dedicated approach, differences between the animals in geometry of the leg and loading conditions were accommodated. Although there were differences between the strains

estimated by the FE models and strains derived from MR tagging experiments (Ceelen et al., 2008a), the models could be used to demonstrate that regions of muscle damage clearly correlated with the presence of high deformations (Ceelen et al., 2008b).

For a comparison of the effects of different loading conditions on the development of muscle damage, the difference between the strains as predicted by the FE models and the real strains present in the experiments should be as small as possible. In this way, the required sample size to detect significant differences between loading conditions can be minimised, which is for practical as well as ethical reasons clearly relevant in experiments involving the use of animals. A detailed description of the geometry of the rat leg was already incorporated in the original model. In the present study, therefore, the material properties and boundary conditions were adapted to answer the following questions: (1) What is the influence of the material law and the boundary conditions on the ability of the model to describe the experimental observations? (2) What is the influence of these model adaptations on the estimated internal muscle deformations?

2.2   Materials & Methods

2.2.1   Animal model

The rat model for DTI is described in detail in Stekelenburg et al. (2006a,b). At the start of the experiment, the animals were anaesthetised with 0.6 L/min medical air with 3 % isoflurane for induction and 1-2 % for maintenance. Hairs of the left hindlimb were removed by shaving, after which the lower leg was placed in a specially designed mold and fixated with plaster cast. A hole in the cast was created to enable compression of the TA muscle with an MR-compatible cylindrical indenter (diameter 3 mm, length 6 mm, attached to a rod), as described previously (Ceelen et al., 2008b). Each rat was placed supine in the experimental setup, which consists of two concentric tubes, as detailed in Stekelenburg et al. (2006a,b). The inner tube housed the animal, and the outer tube was used to position the animal in a 6.3 T MR scanner (Bruker system, horizontal bore, inner diameter 120 mm) with a 400 mT/m gradient coil. The left foot was positioned within a special holder, and a birdcage radio-frequency coil was placed around the lower leg in a fixed position. Indentation of the TA muscle took place inside the MR scanner to assess the geometry of the leg before and during indentation using high-resolution transversal images (FOV = 25×25 mm^2, matrix size = 256×256). Experiments were approved and supervised by the Animal Care Committee of Maastricht University.

2.2.2   FE model

The reference model of Ceelen et al. (2008a) was used as a starting point to estimate local tissue deformations during loading. Dedicated plane stress FE models were developed for MR slices underneath the indenter. The outer contours of the leg and tibia were derived from the corresponding MR image (figure 2.1a) to create an FE mesh. The tibia was assumed rigid, and the muscle tissue was modelled as an incompressible Neo-Hookean solid with strain energy density function W_n:

$$W_n = C_{10}(\lambda_1^2 + \lambda_2^2 + \lambda_3^2 - 3) \tag{2.1}$$

where $\lambda_i(i = 1, 2, 3)$ are the principal stretch ratios and C_{10} is a material parameter, equal to half the shear modulus G. Because the indenter displacement was prescribed, the deformations are not influenced by the value of C_{10}, and thus an arbitrary value was chosen for this parameter. From the MR image of the deformed leg, the boundary conditions consisting of the movement of the tibia during indentation, and the angle and depth of indentation were derived (figure 2.1b). To simulate the presence of the plaster cast, zero-displacement boundary conditions were applied to the section of the outer boundary of the leg that did not move during loading (figure 2.1b).

As described in Ceelen et al. (2008a), the strain distribution in the TA muscle region was determined using a grid (figure 2.1c). The nodal displacements of the FE model during indentation were interpolated onto the grid points (figure 2.1d). With the configuration of the grid in both undeformed and deformed situations, the 2D deformation gradient tensor $\boldsymbol{F}$ was determined for each grid point, using a second-order method to compute strains from a discrete set of displacements (Geers et al., 1996). From $\boldsymbol{F}$, the principal stretch ratios λ_i and in-plane principal strains E_1 and E_2 (with $E_1 > E_2$) were determined. The in-plane maximum shear strain $\gamma = \frac{1}{2}(E_1 - E_2)$ was calculated for each grid point to obtain a measure for the local deformation of the tissue.

2.2.3   FE model adaptations

In the present study, the influence of three different features of the FE model was investigated (table 2.1). The Neo-Hookean material behaviour was compared with a single-mode
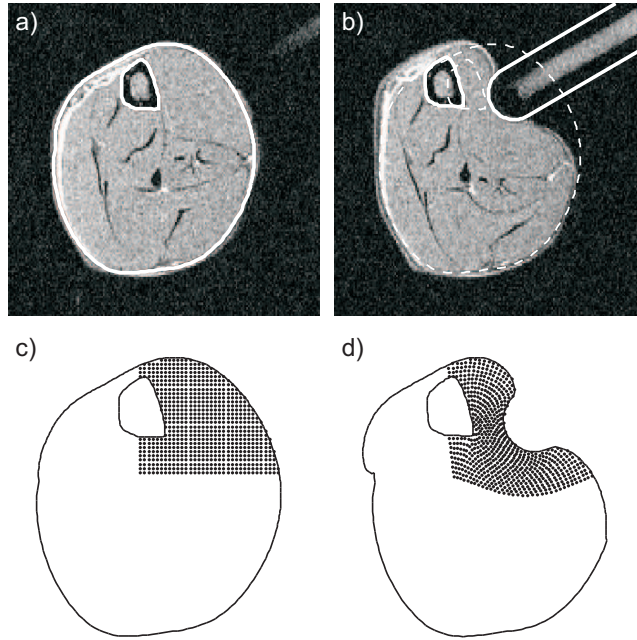
Figure 2.1: a) Transversal MR image of the rat leg before compression. The outer contours (white lines) of the leg and tibia were used for mesh generation. b) The displacement of the tibia and the angle and depth of indentation were derived from the MR image during loading (original mesh contours shown by dashed lines). c) Mesh contours with the grid points in which the local strains were determined. d) Mesh contours and locations of the grid points during indentation.

Ogden model with strain energy density function W_o:

$$W_o = \frac{\mu}{\alpha}(\lambda_1^\alpha + \lambda_2^\alpha + \lambda_3^\alpha - 3) \tag{2.2}$$

Here, $\alpha = 5$ was used to investigate the effect of physically nonlinear material behaviour. As stated earlier, the value of μ was arbitrary since the indenter displacement was prescribed. In Ceelen et al. (2008a,b), frictionless contact was assumed between the leg and the indenter. In the present study, this was compared with simulations with Coulomb friction, where the friction coefficient was adjusted between 0 and 1 to optimise the agreement between experiment and simulation. The boundary conditions that simulate the plaster cast were adapted by modelling the cast as a rigid body in free-slip contact with the leg (figure 2.2b), which was compared to the original zero-displacement boundary conditions in Ceelen et al. (2008a,b) (figure 2.2a). The size of the rigid body in the adapted FE model was larger than the section with zero-displacement boundary conditions in the original model, because this was more in agreement with the experimental conditions.

Table 2.1: FE model adaptations.

FE model feature (p)	(1) Ceelen et al. (2008a,b)	(2) Present study
Material law	Neo-Hookean	Ogden
Friction between tissue and indenter	No	Yes
Boundary conditions plaster cast	Fixed displacement	Rigid body

The influence of the three model features was investigated for six individual FE models simulating the deformation of the TA muscle in six animals, each with unique geometries and loading conditions. For each FE model, four simulations were performed in which the settings of the model features were varied according to a Taguchi orthogonal array as indicated in table 2.2, resulting in a total of 24 simulations (Logothetis and Wynn, 1989). All models were implemented in MSC.Marc (MARC Analysis Research Corporation, 2005).
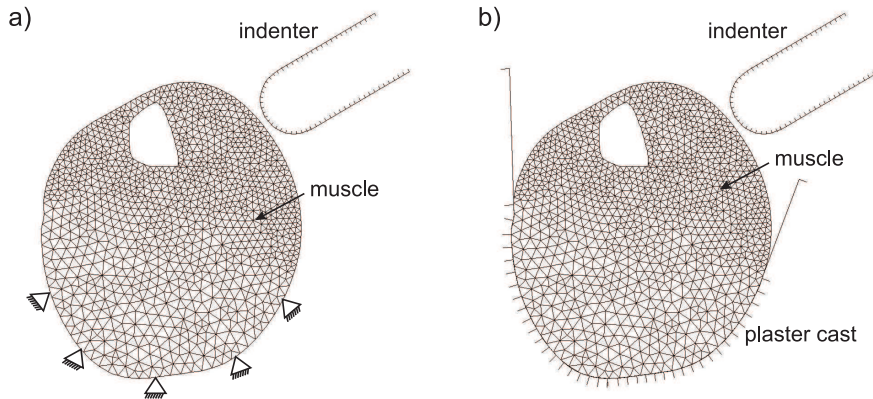
Figure 2.2: a) Original FE model of Ceelen et al. (2008a,b), where the plaster cast was simulated by imposing zero-displacement boundary conditions on part of the outer boundary of the mesh. b) For the adapted boundary conditions, the plaster cast was modelled as a rigid body in free-slip contact with the leg.

Table 2.2: Taguchi orthogonal array to investigate the influence of the material law, friction between the indenter and the leg, and the boundary conditions to simulate the plaster cast.

	Material law	Friction	Plaster cast
Simulation 1	1	1	1
Simulation 2	1	2	2
Simulation 3	2	1	2
Simulation 4	2	2	1

2.2.4 Agreement between model and experiment

To assess the quality of the FE models, the outer contours of the leg in the model were compared with the real contours of the leg as determined from the MR image of the deformed situation. The difference was quantified by calculating the distance between the experimental and mesh contours along 40 equally distributed directions from the centre of the mesh, as illustrated in figure 2.3a. A total measure d for the distance between the model and experimental contours was calculated by adding the squared distances between the contours in all directions (similar to the least squares method):

$$d = \sum_{i=1}^{40} \left((x_{e,i} - x_{m,i})^2 + (y_{e,i} - y_{m,i})^2 \right) \tag{2.3}$$

where $x_{e,i}$ and $y_{e,i}$ are the x- and y-coordinates of the experimental contour at direction i from the centre, and $x_{m,i}$ and $y_{m,i}$ are the corresponding coordinates of the mesh contour.
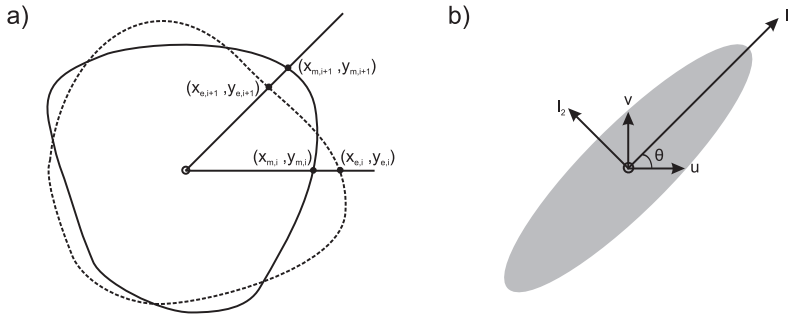
Figure 2.3: a) For 40 equally distributed directions, the distance between the mesh (x_m, y_m) and the experimental contour (x_e, y_e) was determined. A total measure for the distance between the model and experimental contours was calculated by adding the squared distances between the contours in all directions. b) For each high-strain area ($\gamma \geq 0.9\gamma_{max}$, shown in grey), the angle θ ($0° \leq \theta < 90°$) which defines the direction of one of the principal moments of inertia (I_1 or I_2) was calculated to determine the orientation of the high-strain area within the grid for each simulation.

2.2.5   Internal strain distribution

The strain distribution was quantitatively compared between simulations by determining the largest in-plane maximum shear strain γ_{max} in the grid, and the angle of each high-strain area ($\gamma \geq 0.9\gamma_{max}$) in the grid with respect to the horizontal axis (figure 2.3b). The angle was determined by calculating the moments of inertia for the high-strain area. A local coordinate system (u, v), parallel to the original x- and y-axes, was imposed on the centre of the area, and the moments of inertia around the u-axis (I_u), v-axis (I_v), and the product of inertia I_{uv} for the high-strain area A are equal to (Hibbeler, 2001):

$$I_u = \int_A v^2 dA; \quad I_v = \int_A u^2 dA; \quad I_{xy} = \int_A uv dA \tag{2.4}$$

The principal moments of inertia are oriented along and perpendicular to an angle θ with respect to the u-axis, where θ ($0° \leq \theta < 90°$) is given by (Hibbeler, 2001):

$$\tan 2\theta = \frac{-2I_{uv}}{I_u - I_v} \tag{2.5}$$

2.2.6   Effects of adaptations on the model results

The main effects of the three model features on the quality of the model and the resulting strain distribution were investigated by calculating the sum of squares of d, γ_{max}, and θ due to every individual model feature. First, the correction factor (f_c) was calculated (Logothetis and Wynn, 1989):

$$f_c = \frac{(\sum_{i=1}^{N} y_i)^2}{N} \tag{2.6}$$

with y_i the value of y ($y = d, \gamma_{max}, \theta$) for simulation i, and N is the total number of simulations, equal to 24. The sum of squares of d, γ_{max}, and θ due to each model feature p is equal to (Logothetis and Wynn, 1989):

$$S_{y,p} = \frac{y_{p1}^2 + y_{p2}^2}{m} - f_c \tag{2.7}$$

where y_{p1} and y_{p2} are the sum totals of parameter y in which model feature p (material law, friction, or plaster cast) had setting 1 or 2 (table 2.2), respectively, and m is the total

number of simulations for each level, equal to 12. The larger the value of $S_{y,p}$, the larger the influence of model feature p on parameter y.

2.3   Results

In figure 2.4, the mesh contours and strain distribution are shown for the four simulations with one FE model. For this model, clear differences in mesh contours are present, where the overlap with the experimental contour in the MR image is, for example, better in simulation 4 (figure 2.4g) than in simulation 3 (figure 2.4e). There are also differences in the maximum shear strain distribution in the TA muscle region. Larger strains are present in simulations 1 and 2 (figure 2.4b,d) when compared to simulations 3 and 4 (figure 2.4f,h), and the angle of the high-strain area with respect to the horizontal axis is larger in simulations 1 and 3 (figure 2.4b,f) when compared to simulations 2 and 4 (figure 2.4d,h).
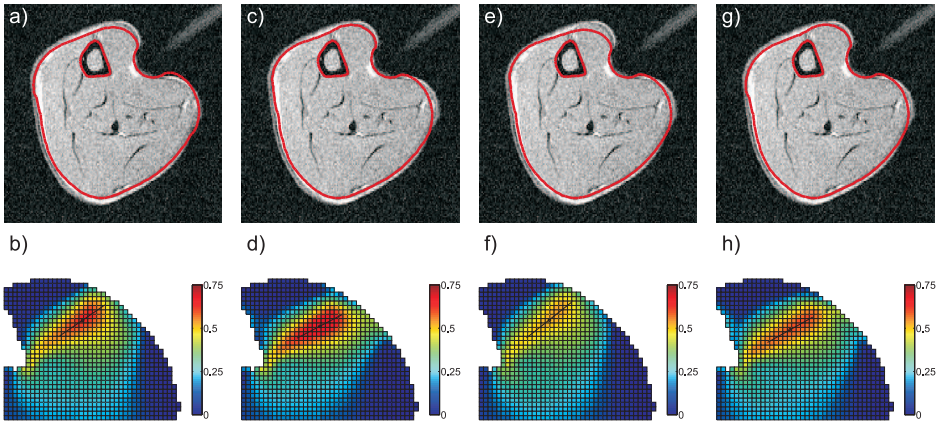
Figure 2.4: *Top:* MR images of the deformed leg with the mesh contours during indentation (red) for one FE model in which model features were varied according to table 2.2. *Bottom:* corresponding maximum shear strain distribution in the TA muscle region for each of the simulations. The centre (o) and the direction (black line) of the largest principal moment of inertia of the high-strain area ($\gamma \geq 0.9\gamma_{max}$) are indicated. a-b) Results for simulation 1; c-d) results for simulation 2; e-f) results for simulation 3; g-h) results for simulation 4.

Table 2.3 shows the sum of squares of d, γ_{max}, and θ due to each of the model features. The material law, friction between the leg and indenter, and the boundary conditions to simulate the plaster cast, have similar effects on the value of d. Parameter γ_{max} is mostly affected by the material law, and friction has the largest influence on θ.

Table 2.3: Sum of squares S of d, γ_{max}, and θ due to each model feature p.

p	S_d	$S_{\gamma_{max}}$ $\times 10^{-2}$	S_θ
Material law	1.16	7.95	11.76
Friction	1.20	1.21	156.06
Plaster cast	1.23	0.01	17.31

In figure 2.5, the mean d values of the two simulations with setting 1 are compared with the corresponding values for the two simulations with setting 2 for all three model features. The relative change of d in simulations with setting 2 compared to setting 1 is also shown in table 2.4. For most FE models a decrease in d is present, although the magnitude of this decrease, which depends on the specific geometry and boundary conditions, is not similar for every model. Nevertheless, in every model at least one of the adapted features causes a considerable decrease in d (table 2.4).
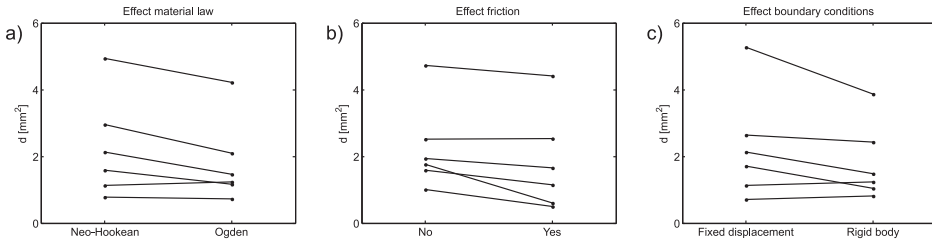
Figure 2.5: Effect of the material law (a), friction between the leg and indenter (b), and the boundary conditions simulating the plaster cast (c) on parameter d (measure for the agreement between model and experiment). The lines indicate how the mean value of d changes for each FE model from setting 1 to 2.

The mean values of γ_{max} and θ for simulations with setting 1 and 2 were compared to determine the influence of the model features on the internal strain distribution (figure 2.6, table 2.4). For each model, γ_{max} is lower in simulations with the Ogden model than in simulations in which Neo-Hookean behaviour was assumed (figure 2.6a, table 2.4). By

Table 2.4: Percentage change of d, γ_{max}, and θ in each FE model if model features are changed from setting 1 to 2 (see table 2.1).

	Feature	Model 1	Model 2	Model 3	Model 4	Model 5	Model 6
	Material law	+9	-31	-29	-15	-27	-8
d	Friction	-66	-15	+1	-7	-27	-50
	Plaster cast	+8	-30	-8	-27	-39	+15
	Material law	-14	-15	-18	-19	-17	-12
γ_{max}	Friction	+11	+2	+1	+1	+7	+28
	Plaster cast	0	-1	0	+1	0	+3
	Material law	+9	+9	-5	-4	+6	+13
θ	Friction	-22	-4	+7	+7	-23	-39
	Plaster cast	+4	+3	+6	+7	+8	+2

contrast, the presence of friction results in a larger γ_{max} when compared to the situation without friction (figure 2.6b, table 2.4). The boundary conditions simulating the plaster cast hardly affect the magnitude of γ_{max} (figure 2.6c, table 2.4). The angle θ is mainly influenced by the incorporation of friction in the FE models, where θ can either increase or decrease due to friction (figure 2.6e, table 2.4). By contrast, both the material law and boundary conditions have considerably less influence on θ (figure 2.6d,f, table 2.4).
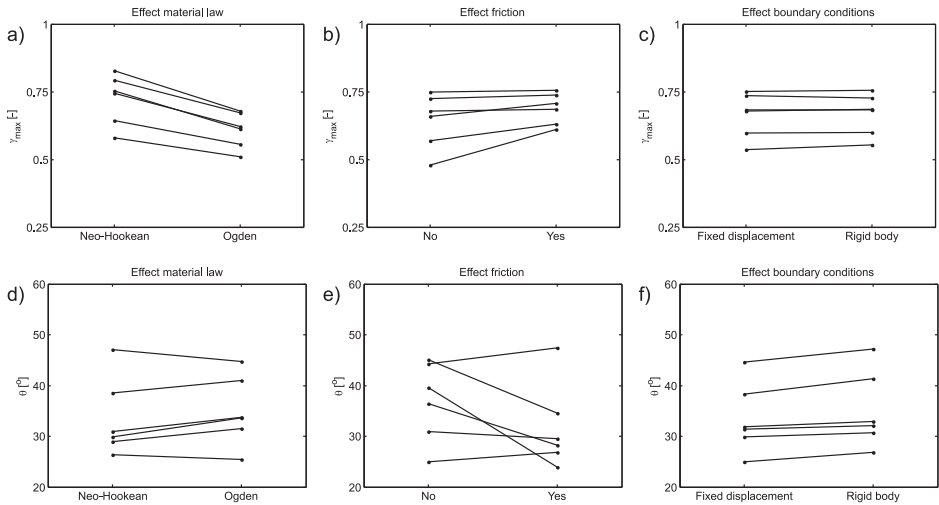
Figure 2.6: Effect of the material law, friction between the leg and indenter, and the boundary conditions simulating the plaster cast on the internal strain distribution represented by γ_{max} (a-c) and θ (d-f). The lines indicate how the mean values of γ_{max} or θ change for each FE model from setting 1 to 2.

2.4   Discussion

In the present study, an FE model that was previously developed by Ceelen et al. (2008a,b) to simulate the compression of skeletal muscle tissue in the rat hindlimb, was adapted to investigate the influence of a number of model features on the agreement with experimental observations and the predictions of the internal strain distributions. The adaptations concerned the material behaviour, and the contact of the muscle tissue with its surroundings and the indenter. In general, all three adaptations had a positive effect on the overlap between the mesh and experimental contours. Furthermore, a change in nonlinearity of the material law mainly affected the magnitude of the largest internal strains. In addition, the inclusion of friction between the indenter and the tissue had a large influence on the direction of the high-strain area in the muscle. By contrast, modelling the surrounding plaster cast as a rigid body only had a small effect on the internal strain distribution.

To assess the agreement of the FE models with the experimental observations, the contours of the leg as determined from the MR images during deformation were compared with the outer boundary of the FE mesh. The difference between both contours was quantified by calculating the total squared distance d between the contours over a number of directions from the centre of the mesh. The values of d were used to determine whether model adaptations improved the quality of the FE model.

Subsequently, the effects of the model adaptations on the estimated strain distribution were investigated by comparing the largest maximum shear strain γ_{max} in the tissue, and the angle θ of the high-strain area ($\gamma \geq 0.9\gamma_{max}$) with respect to the horizontal axis. The values of γ_{max} were used as a measure for the level of total deformation, which is of importance if loading conditions in different animals are to be compared. The angle θ was used to describe the location of the high-strain area in the TA muscle region, which has a large influence on the local comparison of deformation with muscle damage. Since internal deformations were not measured in the experiments, it was not possible to directly determine whether changes in γ_{max} and θ were improvements in the quality of the FE model. It was, however, assumed that the reliability of the calculated deformations improved if d decreased.

The adapted boundary conditions to simulate the plaster cast improved the agreement between model and experiment in four FE models, and only caused a small increase in d in the other two models (figure 2.5c, table 2.4). Due to the larger size of the plaster cast in simulations where the cast was modelled as a rigid body, the motion of the moving part of the muscle was partly restricted during indentation. Although the adapted boundary conditions decreased the difference between the boundary of the mesh and the exper-

imentally observed contour of the muscle tissue, it hardly affected the internal strain distribution in the TA muscle region. Therefore, for the comparison of muscle damage with internal deformations, the approach that was used by Ceelen et al. (2008a,b) is satisfactory. One disadvantage of the original approach, however, is that the sudden transition between completely restricted movement at the part of the boundary where zero-displacements conditions are applied and the relatively large displacements at the free boundary may lead to convergence problems in simulations with large deformations. This problem does not occur if the adapted boundary conditions are applied.

The effect of the material law was investigated by comparing the Neo-Hookean material law with a single-mode Ogden model with a higher nonlinearity in constitutive behaviour (α=5). Changes in material stiffness were not investigated since only one tissue was modelled and the compression of the tissue was displacement-driven in both model and experiment. Since the local deformations of the tissue are mainly determined by the geometry of the leg and the prescribed displacement of the indenter, viscoelasticity was not incorporated into the material law because it only leads to minimal differences in the strain distribution in the tissue (data not shown).

The largest strains in the tissue were lower in simulations with the Ogden model when compared with the Neo-Hookean model (figure 2.6a, table 2.4). This effect was comparable for each experiment and, therefore, the relative comparison of internal strains between experiments will probably not be influenced by a difference in nonlinearity of the constitutive law. Still, the Ogden model may be preferred over the Neo-Hookean model because it improved the capability of the FE model to simulate the experimentally observed results (figure 2.5a, table 2.4), and its behaviour is more similar to the highly nonlinear characteristics of skeletal muscle tissue (Bosboom et al., 2003). Due to convergence problems, however, the parameter α was limited to a value of 5, which necessarily underestimates the nonlinearity of muscle behaviour.

The inclusion of friction caused a reduction in d for almost all FE models (figure 2.5b, table 2.4). Friction considerably influenced the direction and thereby the location of the high-strain area in the TA muscle region (figure 2.6e, table 2.4). Therefore, for a local comparison of muscle damage with deformation, it is important to include friction in the model. The degree and the direction of change was not similar for each experiment, because it primarily depended on the angle of indentation with respect to the outer boundary of the mesh.

In summary, FE models can be used to estimate local tissue deformations due to an external mechanical load, and can thereby contribute to studying the role of deformation in skeletal muscle damage development. By using a dedicated approach, Ceelen et al. (2008a,b) previously reported a clear correlation between deformation and damage in

muscle tissue by compensating for differences in geometry and loading conditions between animals. In the present study, a number of features were adapted in this FE model, all of which had a beneficial effect on the agreement with experimental results. Of these, friction was considered the most important improvement, because its effect was not similar in each model. In this way, variations between animals due to model errors can be further reduced, which adds credence to the capability of the combined experimental-numerical approach to distinguish between the effects of different loading protocols.

Chapter 3

Temporal effects of mechanical loading on deformation-induced damage in skeletal muscle tissue

3.1   Introduction

Prolonged mechanical loading of soft tissues covering bony prominences, as present when individuals are bedridden or wheelchair-bound, may lead to degeneration of skeletal muscle tissue. This can result in a condition termed pressure-related deep tissue injury (DTI), a severe form of pressure ulcer that initiates in deep tissue layers under an intact skin (Black et al., 2007). Subsequently, this tissue damage can progress toward the skin and develop into an extensive wound, with a variable prognosis due to complications, such as osteomyelitis, sepsis, and an increased mortality rate (Thomas, 2001).

The aetiology of different forms of pressure ulcers is not fully understood. Traditionally, compression-induced ischaemia is considered to represent the primary aetiological factor. However, also other damage pathways are involved, such as impaired lymphatic drainage (Miller and Seale, 1981), ischaemia-reperfusion injury (Peirce et al., 2000; Ünal et al., 2001; Tsuji et al., 2005), and sustained tissue deformation (Bouten et al., 2001; Breuls et al., 2003; Stekelenburg et al., 2006b; Gawlitta et al., 2007a). Recently, animal experiments of Stekelenburg et al. (2007) showed that 2 h of continuous muscle compression caused damage in specific regions of the muscle while the complete tissue was ischaemic during loading. Finite element simulations of these experiments by Ceelen et al. (2008b) demonstrated that these regions of damage coincided with the regions subjected to the largest deformations. In addition, muscle damage was only observed in experiments for which a distinct strain threshold was exceeded. This indicates that when local tissue deformations exceed a critical strain threshold, deformation can play an important role in the aetiology of DTI and for a continuous loading period of 2 h, it is more harmful to the tissue than ischaemia.

In clinical practice, however, individuals are subjected to a range of loading regimes, associated with repositioning and pressure relief strategies for wheelchair-bound subjects. It is therefore important to investigate how the relationship between deformation and damage depends on the applied loading regime. In the present study, two questions were addressed: (1) Do the strain-damage relationship and the critical strain threshold for skeletal muscle tissue depend on the load exposure time? (2) Does intermittent load relief as present during repositioning schemes affect the damage evolution?

3.2   Materials & Methods

A combined experimental-numerical approach was adopted to investigate the relationship between muscle deformation and damage, as illustrated in figure 3.1. Animal exper-

iments were performed to monitor the damage evolution in mechanically loaded muscle tissue by means of magnetic resonance imaging (MRI). By simulating these experiments with dedicated finite element (FE) models, the local deformations in the muscle tissue during indentation could be estimated.
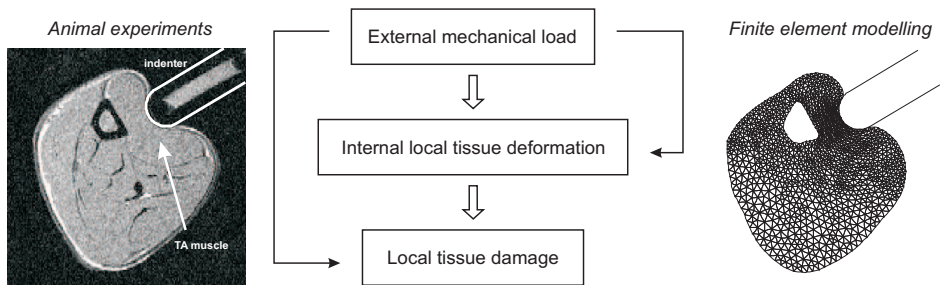
Figure 3.1: Schematic overview of the experimental-numerical approach. Animal experiments were performed in which the damage evolution due to compressive loading was studied with MRI. Dedicated FE models were developed to estimate local tissue deformations during loading. *Left:* MR image of a cross-section of the lower leg of a rat with an indenter compressing the tibialis anterior (TA) muscle. MRI was also used to detect locations of muscle damage after release of the indenter. *Right:* Dedicated FE model of the corresponding cross-section of the leg.

3.2.1   Animal experiments

A previously developed animal model was used to study the damage evolution in skeletal muscle tissue (Stekelenburg et al., 2006a,b; Ceelen et al., 2008b). In this model, 3- to 4-month-old female Brown-Norway rats were used for which the tibialis anterior (TA) muscle in the left hindlimb was mechanically loaded with an indenter. Animals were housed under well-controlled laboratory conditions (12 h light, 12 h dark cycles) and maintained on standard chow and water ad libitum. Rats were anaesthetised with 0.6 L/min medical air with 3 % isoflurane for induction and 1-2 % for maintenance. Respiratory rate was monitored and maintained within the physiological range. The animal experiments were approved and supervised by the Animal Care Committee of Maastricht University.

Experimental protocol

The experimental setup and protocol have been described in detail elsewhere (Stekelenburg et al., 2006a,b; Ceelen et al., 2008b). To summarise briefly, hairs on the left hindlimb of the rat were removed by shaving, after which the left limb was placed in a

specially designed mold and fixated with plaster cast. The anaesthetised animal was positioned supine in the loading device, consisting of two concentric tubes, as illustrated in figure 3.2. The inner one housed the animal, while the outer tube was used to position the rat in a 6.3 T MR scanner (Bruker system, horizontal bore, inner diameter 120 mm) with a 400 mT/m gradient coil. The rat was placed on a heating pad to maintain body temperature within physiological values. The left foot was fixed with a special holder, and a birdcage radio-frequency coil was placed around the limb in a fixed position. A hole in the plaster cast enabled the application of a plastic cylindrical indenter (diameter 3 mm, length 6 mm, attached to a rod) to the TA muscle. The cylinder compressed the tissue with its long axis aligned with the longitudinal axis of the limb, such that a distance of 6 mm underneath the indenter was subjected to approximately uniform indentation in the transverse plane.
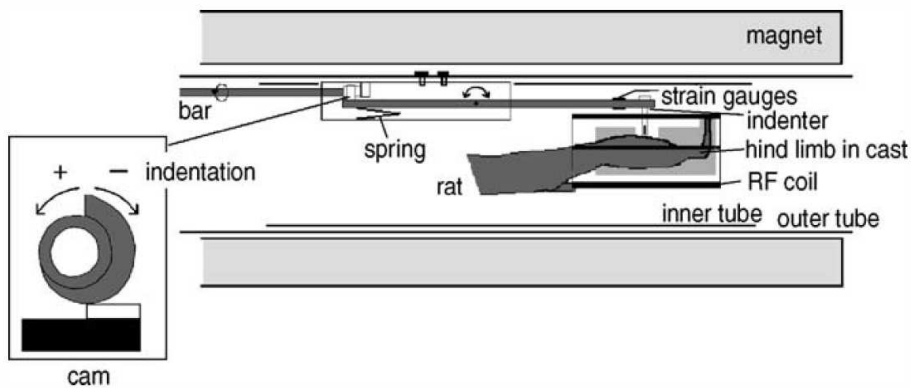
Figure 3.2: Schematic representation of the experimental setup (from Stekelenburg et al. (2006a), with permission.)

The damage evolution in the TA muscle was investigated for three distinct loading regimes, as indicated in figure 3.3. The effect of load exposure time was studied by comparing 2 h loading (figure 3.3a) with 10 min loading (figure 3.3b). The 2 h continuous loading regime was also compared with 2 h of intermittent loading (12 × 10 min loading with 2 min recovery in between, figure 3.3c), to investigate the influence of periodic off-loading on the damage evolution. For the 2 h continuous loading regime, experimental data (n = 11) from Ceelen et al. (2008b) were used. For the 10 min loading and 2 h intermittent loading regimes, 8 and 6 animals were used, respectively.
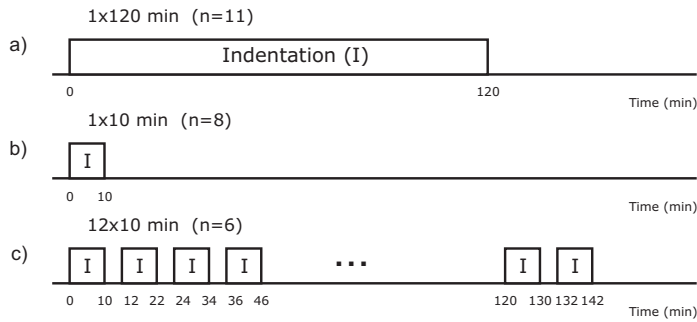
Figure 3.3: Overview of three loading regimes. a) 2 h continuous loading of the tibialis anterior (TA) muscle by indentation (Ceelen et al., 2008b). This loading regime was compared with a shorter (b) loading period (10 min), and with 2 h intermittent (c) loading (12 × 10 min loading with 2 min recovery in between). n denotes the number of animals that were subjected to the different loading regimes.

MR measurements

Transversal scout images were obtained to assess the geometry of the rat leg and the angle and initial position of the indenter. Damage in the TA muscle as a result of indentation was assessed 90 min after the completion of each loading regime with T_2-weighted MRI (multi-echo spin echo sequence with slice thickness = 1 mm, FOV = 25×25 mm^2, matrix size = 128×128 pixels, number of signal averages = 2, echo time TE = 10-320 ms, number of echoes = 32, repetition time TR = 4 s, fat suppression). To obtain a quantitative T_2 map, signal intensities (S) of successive echoes with time (TE) were fitted, on a pixel-to-pixel basis, to the equation

$$S = A + Be^{-TE/T_2} \tag{3.1}$$

In the T_2 map before loading, a region of interest in the TA muscle was selected to determine the mean basal T_2 value and its standard deviation. In the T_2 map after loading, regions covering at least three adjacent pixels with elevated T_2 compared with the mean basal value plus three times the standard deviation were selected as areas with significantly increased T_2 values. Elevated T_2 values have been previously associated with histologically observed muscle damage (Stekelenburg et al., 2006b).

3.2.2 Finite element model

For each animal, dedicated plane stress FE models were developed for 3-4 MR slices underneath the indenter in each experiment, partly based on a previously validated dedi-

cated FE model by Ceelen et al. (2008a,b). In this way, the observed geometric differences between rats were accommodated. To create the mesh, transversal scout images of the rat leg before loading were used to detect the outer contours of the leg and the tibia in Matlab (The Mathworks, Inc.), as illustrated in figure 3.4a. The tibia was assumed to be rigid. The muscle tissue was considered incompressible and was modelled as a single-mode hyperelastic Ogden material with strain energy density W:

$$W = \frac{\mu}{\alpha}(\lambda_1^\alpha + \lambda_2^\alpha + \lambda_3^\alpha - 3) \tag{3.2}$$

In experiments of Bosboom et al. (2001), the parameters of the Ogden model for transverse skeletal muscle tissue were estimated at $\mu = 15.6$ kPa and $\alpha = 21.4$. However, since such a large value for α causes convergence problems in the simulations, $\alpha = 5$ was chosen for the present model, and μ was scaled accordingly ($\mu = 3.6$ kPa) to keep the ratio of μ and α, representing the initial stiffness of the material, equivalent to the one determined by Bosboom et al. (2001). λ_i ($i = 1, 2, 3$) are the principal stretch ratios.

From scout images of the deformed leg, the movement of the tibia during indentation, and the angle and depth of indentation were derived (figure 3.4b). In the FE model, the displacements of the tibia and the indenter were prescribed as essential boundary conditions. In the present study, Coulomb friction was assumed between the leg and the indenter, where the friction coefficient was adapted (between 0 and 1) for each FE model to optimise the correspondence of the outer contour of the leg during indentation between experiment and simulation, as determined by visual inspection. The plaster cast surrounding the leg was modelled as a rigid body in free-slip contact with the leg (figure 3.4c). The FE model was implemented in MSC.Marc (MARC Analysis Research Corporation, 2005).
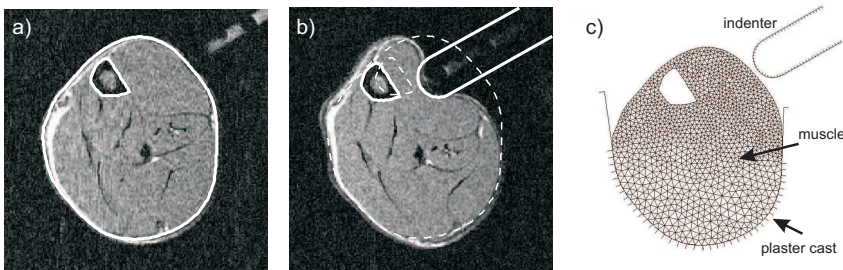
Figure 3.4: a) Transversal scout image of a cross-section of a rat leg before loading. Contours of leg and tibia were determined (white lines) and used for mesh generation. b) Scout image of the same rat leg during loading. Position of the tibia during loading and angle and depth of indentation were determined (solid lines) and used for the essential boundary conditions (contours of leg before loading are shown by dashed lines). c) Resulting FE mesh of the rat leg with indenter and plaster cast modelled as rigid bodies.

3.2.3   Data analysis

To compare local tissue deformations during indentation with damage, the original un-deformed FE mesh was mapped to the situation in the T_2 map 90 min after unloading (figure 3.5a) (Ceelen et al., 2008b). In this quantitative T_2 image, a grid (points located at pixel centres with a spacing of $\sim$0.2 mm) was superimposed on the TA muscle region, and the grid points at which T_2 was significantly increased were identified (figure 3.5b). Subsequently, the grid was mapped to the original undeformed FE mesh to obtain a reference configuration in the situation before loading, as shown in figure 3.5c. From this, the nodal displacements of the mesh during indentation, as determined by the FE analysis, were interpolated onto the grid points, to deform the grid to the situation during loading (figure 3.5d). With the configuration of the grid before and during loading, the 2D deformation gradient tensor $\boldsymbol{F}$ during indentation was determined in each grid point, using a second-order method to compute strains from a discrete set of displacements (Geers et al., 1996). This approach enabled the information on T_2 increase in the grid points to be compared with the tissue deformations at the same locations. From $\boldsymbol{F}$, the principal stretch ratios λ_i ($i = 1, 2, 3$) were determined for each grid point and the strain energy density W was calculated. Thus, in each grid point both the value of W and the presence or absence of a significant increase in T_2 were determined.
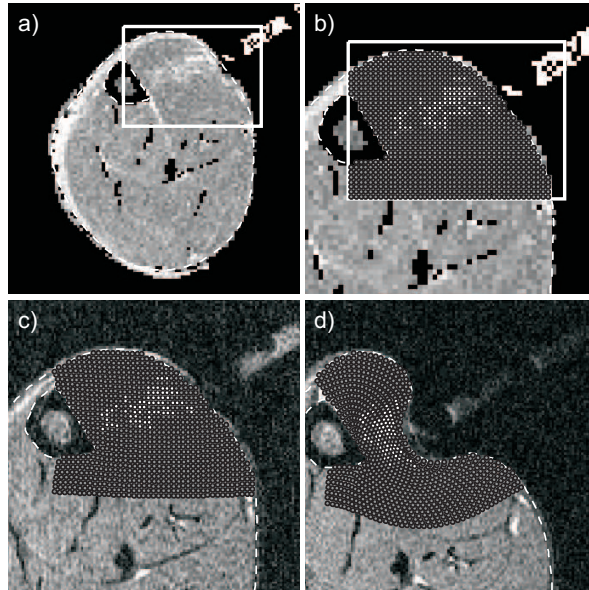
Figure 3.5: a) T_2 map of a rat leg 90 min after unloading. A region of interest around the TA muscle was selected (white box). b) A grid was positioned at the pixel centres within this region. Grid points where T_2 was significantly increased are shown in white. c) The grid was mapped to the original undeformed FE mesh to obtain a reference configuration. d) Grid deformed to the situation during loading.

Two analyses were performed to investigate the relationship between deformation and damage (figure 3.6). In the first analysis, global measures of deformation and damage were used to compare the different loading regimes. In the second analysis, deformation and damage were compared at a local level to establish a material property for muscle tissue independent of the specific geometry and deformation pattern of the experiments.
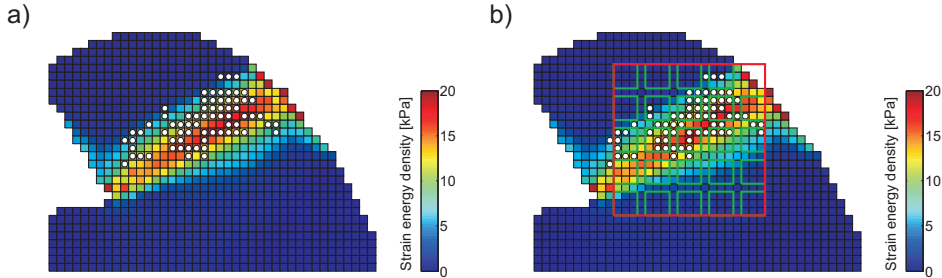
Figure 3.6: Strain energy density in the grid (color) where locations with a significant increase in T_2 are indicated by white circles. a) Global analysis: the strain energy density was integrated over the grid to obtain the 2D strain energy, and the area of elevated T_2 values in the grid was used as a measure of damage. b) Local analysis: $\sim$25 regions (green) of 3x3 grid points were positioned in a smaller area (red box). For each region, the mean strain energy density and the fraction of grid points with elevated T_2 were determined.

Global analysis

As a measure of deformation, the 2D strain energy E needed to deform the TA muscle was calculated for each cross-section by integrating W over the grid (figure 3.6a):

$$E = \int_A W dA = \left(\sum_{i=1}^{N_{gp}} W_i \right) A_{pix} \tag{3.3}$$

where N_{gp} is the number of grid points, W_i is the value of W in grid point i, and A_{pix} is the pixel area. The total area A_d of significantly increased T_2 values was determined for each cross-section as a global measure of damage:

$$A_d = N_d A_{pix} \tag{3.4}$$

where N_d is the number of grid points with an elevated T_2. One value of E and A_d per experiment was obtained by averaging the values of E and A_d over the cross-sections.

Local analysis

It was assumed that the local presence of damage in the tissue follows a binomial distribution with a probability p that depends on the local value of W. To determine p, a smaller area was selected in each grid (red box in figure 3.6b). In this area, approximately 25 regions of 3×3 grid points ($0.6 \times 0.6 \, \text{mm}^2$) were defined. The distance between these regions was one pixel to minimise the spatial dependency of the results in neighbouring regions. For each region, the mean value of W was obtained as a local measure of deformation:

$$\overline{W} = \frac{1}{9} \sum_{i=1}^{9} W_i \tag{3.5}$$

The number of grid points (n_d) with elevated T_2 in the area was used to estimate the local probability on damage:

$$p = \frac{1}{9} n_d \tag{3.6}$$

The relationship between $\overline{W}$ and p was determined by fitting the results of each loading regime to the following logistic regression model (Hosmer and Lemeshow, 2000):

$$\ln \left(\frac{p}{1-p} \right) = b_1 + b_2 \overline{W} \tag{3.7}$$

where b_1 and b_2 are the regression coefficients. To estimate a local deformation threshold for damage, a receiver operating characteristic (ROC) curve was determined for each loading regime to determine an optimal cutoff value for $\overline{W}$ to discriminate between deformations with a high or low risk of causing damage (Akobeng, 2007; Rosner, 2006). The ROC curves were constructed by plotting the sensitivity, which is the probability of correctly predicting damage in case of damage, versus (1 - specificity), where specificity equals the probability of correctly predicting that there is no damage in case of no damage, for a range of cutoff values for $\overline{W}$. Then, the point on the ROC curve closest to the upper left corner (0,1) of the graph was determined as the optimal cutoff value for balancing the sensitivity and specificity (Akobeng, 2007).

3.3   Results

Figure 3.7 shows the MR images and contours of the accompanying FE models (yellow lines) for a typical experiment for each loading regime. Large differences were evident between the shapes of the legs of the different animals (figures 3.7a,e,i), indicating the necessity of developing separate dedicated FE models for each animal. The contours of the FE models of the rat legs during indentation showed a good correspondence with the actual contours of the deformed legs in the MR images (figures 3.7b,f,j). The T_2 maps show that elevated T_2 values in the TA muscle were concentrated in a narrow region extending from the skin underneath the indenter to the tibia for all three loading regimes (figures 3.7c,g,k).
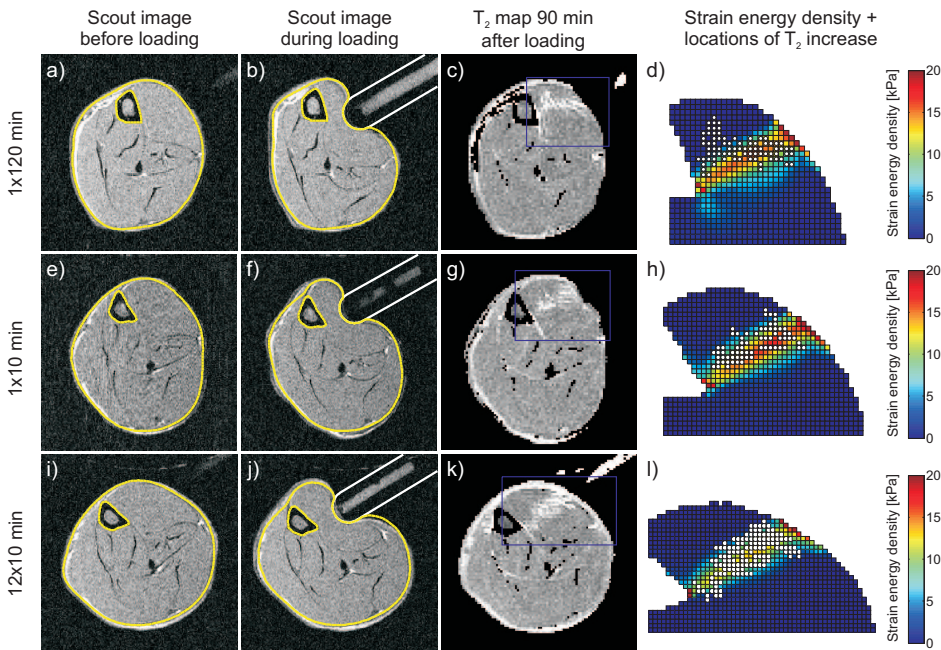
Figure 3.7: Scout images with corresponding FE model contours (yellow), T_2 maps with ROI (purple) including the TA muscle, and distributions of W (colour) together with locations of T_2 increase (white circles) in the ROI for a typical experiment with 2 h continuous loading (a-d), 10 min loading (e-h), and 2 h intermittent (12×10 min) loading (i-l).

The distributions of W in the grids, derived from the FE analyses, are shown in figures 3.7d,h,l, where the locations with significantly increased T_2 are indicated by white circles. For all three loading regimes, elevated T_2 values were mainly present in highly deformed areas. For the 2 h continuous loading regime, the region of T_2 increase clearly corresponded to the region of high values of W (figure 3.7d). However, the spatial T_2 pattern was slightly different from that of the deformation profile. For the other two loading regimes, there was very close correspondence between the regions of T_2 increase and high deformations (figure 3.7h and l).

3.3.1   Global analysis

The results of the global comparison of deformation and damage are depicted in figure 3.8. For each experiment, the mean area A_d with elevated T_2 in the TA muscle is plotted against the mean 2D strain energy E in the muscle during indentation. Figure 3.8 shows that no T_2 increase occurred for all three loading regimes when E was less than a threshold zone ranging from $0.8 \cdot 10^{-4}$ to $1.0 \cdot 10^{-4}$ J/mm. When this threshold was exceeded, A_d increased monotonically with E. When the two continuous loading regimes are compared, this increase of the affected area with E was larger for 2 h loading than for 10 min. By contrast, there were little differences in size of the affected region at corresponding E values, when the results of 2 h continuous loading are compared with 2 h intermittent loading.
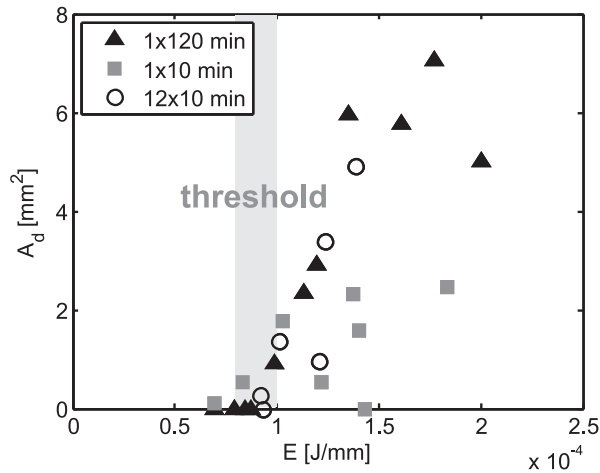
Figure 3.8: Mean area A_d with significantly increased T_2 values in the TA muscle versus the mean 2D strain energy E in the muscle during indentation.

3.3.2   Local analysis

Figure 3.9a shows the probability p on a significant increase in T_2 value as a function of $\overline{W}$ for each loading regime. For both 10 min continuous and 2 h intermittent loading, the probability was approximately zero for $\overline{W} = 0$ and increased with $\overline{W}$. However, beyond $\overline{W} \approx 5$ kPa, the curves of these two loading regimes started to diverge, with p values for 2 h intermittent loading being consistently higher than those for 10 min loading. For 2 h continuous loading, p was slightly larger than zero when $\overline{W} = 0$, and increased further with $\overline{W}$. Differences were also evident between the derived probability curves of the 2 h loading regimes, with a steeper increase of p with $\overline{W}$ for intermittent loading when compared to continuous loading (figure 3.9a).
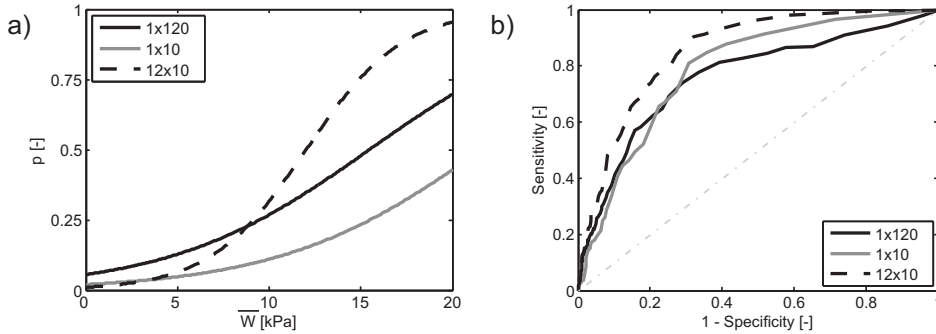
Figure 3.9: a) Probability p on a significant increase in T_2 as a function of the mean strain energy density $\overline{W}$. b) Receiver operating characteristic (ROC) curves for the three loading regimes.

From the ROC curves, depicted in figure 3.9b, the optimal cutoff values for $\overline{W}$ can be determined to discriminate between high- and low-risk deformations. These values, as indicated in table 3.1, reveal a local threshold value of approximately 6-7 kPa for each of the three loading regimes.

Table 3.1: Parameters of the logistic regression models (b_1 and b_2) and optimal cutoff values (p_c and $\overline{W}_c$) to discriminate between high- and low-risk deformations, as derived from the ROC curves. p_c is the optimal cutoff probability, $\overline{W}_c$ is the optimal cutoff value for $\overline{W}$.

Loading regime	b_1 [-]	b_2 [kPa^{-1}]	p_c [-]	$\overline{W}_c$ [kPa]
1x120 min	-2.8	0.18	0.15	6.0
1x10 min	-3.9	0.18	0.07	7.2
12x10 min	-4.6	0.38	0.09	5.9

3.4 Discussion

In the present study, the effects of load exposure time and intermittent load relief on the development of deformation-induced skeletal muscle damage were investigated in a rat model, using a combination of MRI techniques and dedicated FE models. The effect of exposure time was investigated by comparing 2 h and 10 min continuous loading periods. The 2 h continuous loading period was also compared with a 2 h intermittent loading protocol to assess the effect of periodic relief of loading. It was found that muscle damage only occurred beyond a deformation threshold, which was similar for each of the three loading regimes. When the threshold was exceeded, the amount of muscle damage was larger after a 2 h loading period than after 10 min of loading. Brief periods of load relief during a 2 h loading period did not have any significant effect on the damage evolution.

A well-established animal model was used to study the development of deformation-induced muscle damage by means of T_2-weighted MRI (Stekelenburg et al., 2006a,b). An increase in the transverse relaxation time T_2 is generally accepted as an indication of tissue damage (Fleckenstein, 1996). Moreover, in previous studies a good correlation was reported between T_2-weighted MRI and skeletal muscle damage assessed histologically (Bosboom et al., 2003; Stekelenburg et al., 2006b). Therefore, locations in the tissue exhibiting a significant increase in T_2 value after loading were considered to represent areas of tissue damage. However, several pathological mechanisms, e.g. oedema, necrosis, and inflammation, may contribute to the T_2 elevation and can therefore not be distinguished. Additionally, the T_2 increase observed in this study reflects early cellular damage and swelling, and not an advanced state of damage as present during DTI (Stekelenburg et al., 2006b).

The internal tissue deformations during loading were simulated by means of dedicated FE models, based on a previously validated FE model of Ceelen et al. (2008a,b). The use

of dedicated FE models to estimate the internal deformations during loading enabled the comparison of deformation and damage within the same experiment. In addition, this approach could account for the variability in the observed amounts of damage between experiments due to different tissue geometries and deformations. The FE models reported from our previous study showed good agreement with internal muscle deformations as determined from MR-tagging data (Ceelen et al., 2008a). The high level of agreement of the deformed FE model contours with the MR images in that study supported the assumption of a plane stress situation. Furthermore, since displacements were prescribed, the geometry and boundary conditions had a larger influence on the resulting strains than the material properties of the muscle tissue. In the present study, a number of adaptations were implemented in the model to further improve the correspondence between FE model and experiment. A hyperelastic Ogden model was used with a higher order of nonlinearity than the Neo-Hookean material law that was used in the original FE model of Ceelen et al. (2008a). The model parameters were partly based on experiments of Bosboom et al. (2001), but the high order of nonlinearity that was estimated in that study could not be imposed due to convergence problems. Therefore, the results of the present study should not be considered as absolute values, but rather as relative values to distinguish between the effects of different loading regimes. Using a more sophisticated constitutive model for skeletal muscle tissue (e.g. see Van Loocke et al. (2008)) would improve the FE model in the sense that a more accurate estimation of threshold values could be obtained. Including friction between the indenter and rat leg strongly influenced and improved the overlap between the outer contours of the leg in FE model and experiment, and also influenced the locations in the FE model where the largest deformations were present. Including friction was therefore considered to represent a major improvement to the model.

However, even with the improved FE model, the comparison of deformation and damage in the 2 h continuous loading regime showed a consistent spatial mismatch between the deformation and damage profiles. This mismatch might be caused by the relative sliding of different muscle groups during loading, which was not incorporated in the FE model. Apparently, this effect did not occur within a 10 min loading period, since almost complete overlap of damage and high deformations was observed for the 10 min loading period and the 2 h intermittent loading protocol consisting of 12 periods of 10 min loading. This spatial mismatch could not affect the global analysis. However, it clearly influenced the results of the local analysis in which a probability function for damage was estimated. Since part of the damage as assessed from the MR images was located in low-strain areas in the FE model instead of the high-strain region, the mismatch probably caused an overestimation of the probability on damage for low strain energy densities, and an underestimation of this probability for high strain energy densities. The results of the local analysis for the 2 h continuous loading regime should therefore be treated with caution, and should not be interpreted as absolute values.

Damage in the tissue was only present if a distinct deformation threshold, of similar magnitude for each of the three loading regimes, was exceeded. This result was obtained from both a global analysis of the results in which the strain energy in the tissue was compared with the total area exhibiting a T_2 increase, and a local analysis in which the local T_2 increase was compared with the local strain energy density. The global analysis showed that no damage occurred for experiments with 2D strain energies below a threshold range of $0.8 \cdot 10^{-4}$ to $1.0 \cdot 10^{-4}$ J/mm. The advantage of this analysis is that the deformation and damage in each experiment could be classified with a single value, facilitating the comparison of the different experiments and loading regimes. However, since the derived threshold value is only applicable to the specific deformation pattern applied in this study, it should not be interpreted as an absolute value. ROC curves were used to estimate a local deformation threshold that is effectively independent of the applied deformation profile. Due to the spatial mismatch between deformation and damage for the 2 h continuous loading regime, the derived cutoff probability for this loading regime was considerably larger than for the other two protocols, which is considered an artifact. The local deformation threshold itself appeared to be similar for each loading regime, corresponding to a strain energy density of approximately 6-7 kPa. It should, however, be noted that the absolute value of this threshold depends on the constitutive model and the values of the material parameters in the FE model. The fact that the deformation threshold for damage within a 2 h loading period was independent of the load exposure time, supports the idea of an inverse sigmoid relation between deformation and time that will lead to tissue damage (Linder-Ganz et al., 2006; Gefen et al., 2008; Gefen, 2009). For short loading periods, the deformation effectively determines the threshold for damage, which corresponds to the initial upper plateau phase of the sigmoid curve. It appears that for the present animal model this initial plateau phase exists for at least 2 h. However, it should be noted that the threshold value and the duration of this initial plateau phase can be different for other animals and in particular for humans, depending on their susceptibility to tissue damage induced by mechanical loading. Thus, an extrapolation of the present threshold to the human situation, particularly with the inherent variability associated with confounding factors, must be taken with caution.

When the deformation threshold for damage was exceeded, the global analysis showed a monotonic increase of the amount of muscle damage with the internal strain energy. This increase of damage with strain energy was larger after a 2 h loading period than after 10 min. From the local analysis, the probability of damage as a function of the local strain energy density also appeared to be higher for the 2 h than the 10 min loading period. Thus, the load exposure time influences the amount of damage that develops due to deformation. This increase in affected area in the tissue might be caused by a physiological effect. For example, the release of cellular constituents from dead cells may trigger cell death in the surrounding tissue. Another possible explanation could be the local change of mechanical properties associated with dead tissue. For example, Gefen

et al. (2005) found a significant increase in muscle stiffness after cell death, which can subsequently increase the deformations of the surrounding tissue and thereby the total amount of damage.

When the 2 h continuous and intermittent loading regimes are compared in the global analysis, the increase of damage with strain energy appeared to be similar for both loading regimes. On the other hand, the local analysis suggested distinct differences in the local probability of damage. The continuous loading protocol caused more damage than the intermittent load for small strain energy density values, while the reverse was the case for high strain energy densities. However, it is postulated that these differences in the local analysis were caused by the mismatch between the damage and deformation profiles in the 2 h continuous loading regime. This mismatch is considered a shortcoming of the FE model, and therefore a comparison of these two loading regimes based on the results of the local analysis would lead to erroneous conclusions. For the present study, it is therefore concluded that intermittent load relief did not affect the damage evolution within a 2 h loading period. This may be a result of the fact that a 2 h loading period is unlikely to cause any ischaemic damage in our animal model. Indeed, it has been shown by Stekelenburg et al. (2007) that 2 h of complete ischaemia as induced by a tourniquet induced no significant damage in the tissue. Therefore, reperfusion during load relief would neither reduce any ischaemic damage, nor cause additional damage due to ischaemia-reperfusion injury. During longer periods of mechanical loading, intermittent load reliefs may show a larger influence on the damage evolution, since then ischaemia is expected to play a larger role in the damage process in skeletal muscle tissue. In addition, the off-loading period could also have been too short to affect the evolution of muscle damage. Makhsous et al. (2007) measured the perfusion in the buttocks of human volunteers during a sitting protocol including wheelchair pushups, and found that these pushup periods of approximately 30 s were insufficient to provide complete recovery of tissue perfusion. Coggrave and Rose (2003) also reported that almost 2 min of pressure relief were needed to restore tissue oxygen to basal unloaded levels in spinal cord injury individuals.

In summary, the present study showed that the tissue deformations during mechanical loading determine whether or not skeletal muscle damage develops within a short (2 h in our animal model) loading period. The deformations that were applied in this study are clinically relevant when compared to internal soft tissue strains in paraplegic individuals sitting on a hard surface (Linder-Ganz et al., 2008). Therefore, to prevent muscle damage that already develops during short periods of mechanical loading, it is important to minimise tissue deformations by means of cushions and mattresses with appropriate stiffness, such that the deformation threshold for damage is not exceeded. If the deformations do exceed the threshold, then the exposure time determines how much damage develops in the tissue. Limiting the exposure time may therefore also help to minimise

the amount of muscle damage due to mechanical loading. In the present study, intermittent load relief appeared to have minimal effect on the damage evolution. In clinical practice, relief of continuously applied pressure is often accompanied by a change in posture. It is expected that the resulting redistribution of the mechanical load would inevitably influence the damage evolution, and may therefore be more important than temporarily restoring tissue perfusion.

Acknowledgements

Chapter 4

Ischaemia-reperfusion injury in rat skeletal muscle assessed with T_2-weighted and dynamic contrast-enhanced MRI

4.1   Introduction

Pressure ulcers are localised areas of soft tissue breakdown that develop usually over bony prominences as a result of prolonged mechanical loading. For this reason, they are particularly common in bedridden or wheelchair-bound individuals, and represent one of the most common secondary complications in spinal cord injured subjects (McKinley et al., 1999). One specific form of pressure ulcer is termed deep tissue injury (DTI), which is defined as pressure-related injury to subcutaneous tissues, such as skeletal muscle, initially under intact skin (Ankrom et al., 2005; Black et al., 2007). Evolution of such a wound may be rapid, thereby exposing additional layers of tissue even with treatment strategies (Black et al., 2007), and is associated with a variable prognosis due to a range of complications (Thomas, 2001).

The aetiology of pressure ulcers is not completely understood (Bouten et al., 2003). Compression-induced ischaemia is traditionally considered to represent the most important aetiological factor (Kosiak, 1959; Daniel et al., 1981). Other theories involve ischaemia-reperfusion (I-R) injury (Peirce et al., 2000; Tsuji et al., 2005), impaired lymphatic drainage (Miller and Seale, 1981), and sustained tissue deformation (Stekelenburg et al., 2007; Ceelen et al., 2008b). Recently, deformation was reported to be the primary determinant for skeletal muscle damage in a rat model for loading periods up to 2 h (Stekelenburg et al., 2007; Ceelen et al., 2008b; Loerakker et al., 2010). However, in clinical situations, where individuals are often exposed to prolonged periods of mechanical loading, it might be predicted that ischaemia plays an increasingly important role in the damage process. To address these loading conditions, repositioning schemes and alternating pressure mattresses are used, both of which involve reperfusion. Accordingly, it is important to investigate the relative contributions of both ischaemia and reperfusion in the aetiology of DTI.

Ischaemia may lead to disturbed intracellular ion concentrations, accumulation of metabolic waste products, and cell swelling. It is generally accepted that reperfusion after an ischaemic period can reverse these effects by restoring tissue oxygen levels and removing waste products from the previously ischaemic tissue. However, reperfusion after prolonged ischaemia may also aggravate tissue damage due to the activation of reactive oxygen species, inflammation, and oedema, a process that is known as I-R injury (McCord, 1985; Rubin et al., 1996; Blaisdell, 2002). Indeed, it was shown in a rat model that when the total duration of ischaemia was constant, a larger number of I-R cycles caused more damage to the skin of rats than continuous ischaemia alone (Peirce et al., 2000). In addition, Tsuji et al. (2005) reported that microcirculatory flow in the skin of mice was more reduced after repeated I-R cycles than after a single ischaemic insult of equivalent duration. Previous studies, however, were limited as perfusion was measured

with limited spatial or temporal resolution. Moreover, since tissue damage was often assessed with histology, by definition a destructive technique, temporal changes in tissue properties could not be investigated within a single experiment.

In the present study, the effects of ischaemia and reperfusion were investigated in a previously developed rat model to study the aetiology of DTI (Stekelenburg et al., 2006a,b). In particular, the local relationship between post-ischaemic perfusion and changes in skeletal muscle integrity was investigated using a combination of two magnetic resonance imaging (MRI) techniques. Tissue perfusion was examined with dynamic contrast-enhanced MRI (DCE-MRI) using a paramagnetic contrast agent, which is an established method to investigate local differences in perfusion (Sotgia et al., 2008; Thompson et al., 2005). Changes in muscle structural integrity were monitored with T_2-weighted MRI, where an increase in the transverse relaxation time T_2 was used as a measure of muscle pathology related to oedema, necrosis, and inflammation (Fleckenstein, 1996). Since MRI is nondestructive, DCE-MRI and T_2 data were collected at several occasions during each experiment to monitor changes with time.

4.2   Materials & Methods

4.2.1   Animal model

A previously developed animal model was used to study the perfusion and damage process in skeletal muscle tissue (Stekelenburg et al., 2006a,b). In the present study, four 4-5-month old female Brown-Norway rats, weighing between 178 and 183 g, were used. The animals were housed under well-controlled laboratory conditions (12 h light, 12 h dark cycles), and maintained on standard chow and water ad libitum. At the start of the experiment, the animals were anaesthetised with 0.6 L/min medical air with 3 % isoflurane for induction and 1-2 % for maintenance. Respiratory rate and rectal temperature were monitored and maintained within the physiological range during the experiment. A heating pad was used to keep the body temperature between 36 and 37 °C.

Hairs of the left hindlimb of each anaesthetised animal were removed by shaving, after which the lower leg was placed in a specially designed mold and fixated with plaster cast. A water-filled capillary was embedded in the plaster cast as a reference point for comparison between MR measurements. A catheter was implanted in the jugular vein to enable the administration of contrast agent during the perfusion measurements. Each rat was placed supine in the experimental setup, which consists of two concentric tubes, as detailed in Stekelenburg et al. (2006a,b). The inner one housed the animal, and the outer

tube was used to position the animal in a 6.3 T MR scanner (Bruker system, horizontal bore, inner diameter 120 mm) with a 400 mT/m gradient coil. The left foot was positioned within a special holder, and a birdcage radio-frequency coil was placed around the lower leg in a fixed position.

Ischaemia was applied with a silicone vessel loop (Identi Loops supermaxi blue, Dispo Medical), which was applied around the thigh to restrict blood flow in the complete lower leg. The ischaemic condition was maintained for 4 h, after which the vessel loop was removed. Post-ischaemic DCE-MRI and T_2 data were collected during the subsequent 2 h period. The experimental protocol was approved and supervised by the Animal Care Committee of Maastricht University.

4.2.2   MR measurements

High-resolution transversal scout images (FOV = 25×25 mm^2, matrix size = 256×256) were obtained during the experiment to assess the geometry of the rat leg. DCE-MRI was used to calculate local contrast enhancement parameters, and changes in the muscle tissue were assessed with T_2-weighted MRI several times during the 6 h investigation period. A time schedule of the MR measurements is illustrated in figure 4.1.
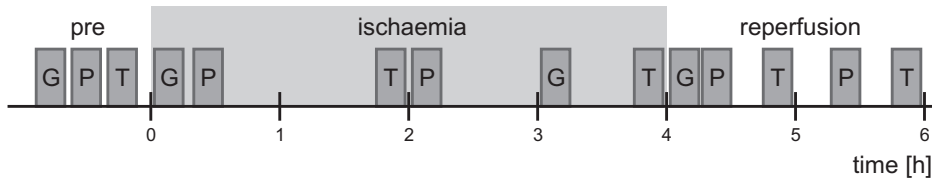
Figure 4.1: Time schedule of the experiments including the different MR measurements: G = transversal scout images to assess the geometry of the leg; P = DCE-MRI to investigate the perfusion; T = T_2-weighted MRI to monitor changes in muscle tissue. Ischaemia was applied at 0 h by means of a vessel loop. After 4 h, the vessel loop was removed, and MR measurements were continued for another 2 h.

DCE-MRI

Local contrast enhancement in the leg was investigated using an intravenous injection of paramagnetic contrast agent ProHance (Gd-HP-DO3A, Bracco Diagnostics Inc.). To estimate T_1 in the leg before contrast agent administration ($T_{1,pre}$), a 3D T_1-weighted FLASH (RF- and gradient-spoiled) sequence was applied with the following imaging parameters:

FOV $= 25 \times 25 \times 17.6$ mm^3, matrix size $= 128 \times 96 \times 16$, TR $=$ 10 ms, TE $= 2.8$ ms, and multiple flip angles α equal to 2°, 5°, 7°, 10°, 15°, and 20°. The resulting signal S is given by:

$$S = S_0 \sin(\alpha) \frac{1 - e^{-TR/T_1}}{1 - \cos(\alpha) e^{-TR/T_1}} \tag{4.1}$$

with two unknowns: S_0, which includes proton density, T_2^* decay, and scanner scaling, and T_1. For each voxel, the signal that was collected at the six flip angles was nonlinearly fitted to equation 4.1 to obtain an estimate for $T_{1,\text{pre}}$ (Yankeelov and Gore, 2009). Subsequently, a dynamic series of 3D FLASH acquisitions (with $\alpha = 15°$) was applied to investigate the perfusion in the leg. After four baseline image acquisitions, a 100 μL bolus of ProHance (0.2 mmol/kg) was administered via the catheter in the jugular vein, while image acquisition was continued for a further 45 scans. To calculate $T_1(t)$ in each voxel, S_0 was first eliminated from equation 4.1 by dividing $S(t)$ by the baseline signal S_{pre}:

$$\frac{S(t)}{S_{\text{pre}}} = \frac{1 - e^{-TR/T_1(t)}}{1 - \cos(\alpha) e^{-TR/T_1(t)}} \cdot \frac{1 - \cos(\alpha) e^{-TR/T_{1,\text{pre}}}}{1 - e^{-TR/T_{1,\text{pre}}}} \tag{4.2}$$

where S_{pre} was obtained by averaging $S(t)$ from the first four scans. By substituting:

$$X = \frac{1 - \cos(\alpha) e^{-TR/T_{1,\text{pre}}}}{1 - e^{-TR/T_{1,\text{pre}}}} \quad \text{and} \quad Y = S(t)/S_{\text{pre}} \tag{4.3}$$

$T_1(t)$ was calculated (Haacke et al., 2007):

$$T_1(t) = \frac{-TR}{\ln\left(\frac{X - Y}{X - Y\cos(\alpha)}\right)} \tag{4.4}$$

The concentration of contrast agent $C(t)$ in each voxel was calculated from the change in T_1 according to:

$$C(t) = \frac{1}{r_1} \left(\frac{1}{T_1(t)} - \frac{1}{T_{1,\text{pre}}} \right) \tag{4.5}$$

where r_1 represents the T_1 relaxivity of the contrast agent, equal to $\sim$3 mM^{-1} s^{-1} at 6.3 T (Laurent et al., 2006; Blockley et al., 2008).

To characterise the time course of contrast enhancement, a piecewise linear fit was applied to $C(t)$ in each voxel (Singh et al., 2009). A quantitative tracer kinetic model, such as the two-compartment Tofts model (Tofts et al., 1999), was not used, because this requires the knowledge of an arterial input function, which could not be determined in the present study because damage to the blood vessels is likely to occur. As illustrated in figure 4.2, each curve was divided into three linear phases: a constant baseline phase, a rapid initial rise in $C(t)$, and a third phase in which $C(t)$ can be either increasing or decreasing:

$$C_{\text{fit}}(t) = \begin{cases} c & \text{for } t \leq \alpha \\ c + b_1(t - \alpha) & \text{for } \alpha \leq t \leq \beta \\ c + b_1(\beta - \alpha) + b_2(t - \beta) & \text{for } t \geq \beta \end{cases} \tag{4.6}$$

where α and β are the intersection time points between the line segments, c is the baseline concentration before contrast agent administration, and b_1 and b_2 are the slopes of the second and third line segment, respectively. Constants c, b_1, and b_2 were derived by fitting $C_{\text{fit}}(t)$ to $C(t)$ using the least squares method, and α and β were varied until the difference between $C_{\text{fit}}(t)$ and $C(t)$ was minimal.
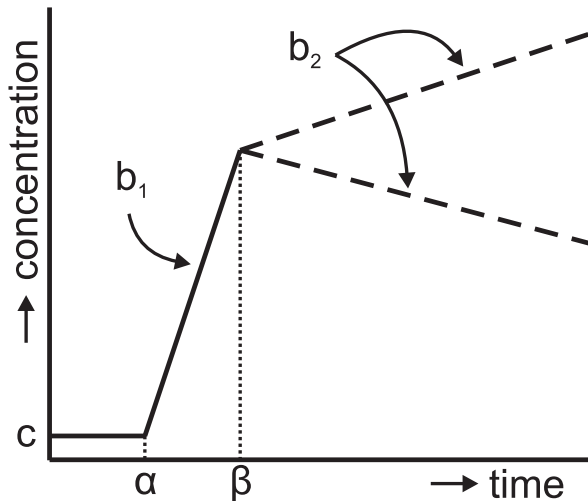
Figure 4.2: The time course of $C(t)$ was characterised by fitting the data of each voxel to a piecewise linear fit model consisting of three line segments with intersection points α and β. The first segment represents the baseline concentration (c), the second segment with slope b_1 describes the rapid initial increase in $C(t)$, and the third phase has slope b_2 which can be either positive or negative. The area A under the curve above the baseline concentration c was also determined.

For each curve, four parameters were used for comparison with T_2 data: slopes b_1 and b_2, the concentration at the first peak $C_p = C_{fit}(t = \beta)$, and the total area A under the curve above the baseline. The area A was calculated from the other parameters and equal to $\frac{1}{2}(\beta - \alpha)(C_p - c) + (t_{end} - \beta)(C_p - c) + \frac{1}{2}(t_{end} - \beta)(C_{end} - C_p)$, with t_{end} and C_{end} the time and concentration at the end of the DCE-MRI scan, respectively. For the concentration data during post-ischaemic perfusion, each parameter was divided into three subgroups (low, normal, and high) to investigate spatial differences in contrast enhancement in the leg. The thresholds to distinguish between low, normal, and high parameter values were derived from the distribution of each parameter in the initial DCE-MRI scan before ischaemia. From this distribution, the 25th (p_{25}) and 75th (p_{75}) percentile and the interquartile range $r_{IQ} = p_{75} - p_{25}$ were determined, and the lower and upper thresholds for the normal subgroup were defined as $t_l = p_{25} - r_{IQ}$ and $t_h = p_{75} + r_{IQ}$, respectively.

T_2-weighted MRI

Changes in the muscle tissue were monitored with T_2-weighted MRI, using a multi-echo spin echo sequence (FOV = 25×25 mm^2, matrix size = 128×128, slice thickness = 1 mm, 11 slices, TR = 4 s, TE = 10-320 ms, 32 echoes, and fat suppression using a spectrally-selective 90 ° pulse followed by a spoiler gradient). A quantitative T_2 map was obtained by fitting the data of the first eight echoes to:

$$S = S_0 e^{-TE/T_2} \tag{4.7}$$

Comparison of contrast enhancement and T_2

DCE-MRI and T_2 data were coregistered in four consecutive MR slices. The high-resolution scout images were used to define the outer boundary of the leg and the tibia in each slice. Between these two boundaries, a grid was defined with the resolution of the DCE-MRI data (distance between grid points 25/128 mm and 25/96 mm in horizontal and vertical direction, respectively). Subsequently, this grid was mapped to the corresponding slices in the DCE-MRI data based on the contours of the leg, and the pixel values of the contrast enhancement parameters were linearly interpolated onto the grid points. The same procedure was applied to the T_2 maps, to enable comparison of the contrast enhancement parameters with T_2 at identical locations.

Influence of ProHance on T_2

Besides decreasing T_1, the contrast agent might also affect the T_2 measurements. Therefore, the effect of ProHance on T_2 was investigated in three rats. For each animal, quantitative T_2 maps of the leg were obtained first. Subsequently, a 100 μL bolus of ProHance (0.2 mmol/kg) was administered and $C(t)$ was determined. A second series of T_2 maps was subsequently acquired to determine the decrease in T_2 caused by the contrast agent. To estimate the T_2 decrease as a function of C, it was assumed that:

$$C_{\text{end}} = \frac{1}{r_2} \left(\frac{1}{T_{2,\text{post}}} - \frac{1}{T_{2,\text{pre}}} \right) \tag{4.8}$$

where C_{end} is the contrast agent concentration at the end of the DCE-MRI scan, r_2 is the T_2 relaxivity of ProHance, and $T_{2,\text{pre}}$ and $T_{2,\text{post}}$ are the T_2 values as measured in the T_2 maps before and after contrast agent administration, respectively. Median values of $T_{2,\text{pre}}$ and $T_{2,\text{post}}$ in the leg were determined for four slices of each animal. For the corresponding slices of the DCE-MRI data, the median C_{end} in the leg was calculated. The transverse relaxivity r_2 was then determined by fitting the results to equation 4.8. For the I-R experiments, the T_2 value in each grid point was corrected for the corresponding C_{end} value of the preceding DCE-MRI scan using r_2.

4.2.3 Statistical analysis

Associations between the different contrast enhancement parameters during the post-ischaemic phase were assessed with the Spearman rank correlation coefficient r_s. Differences in T_2 with time and between contrast enhancement subgroups were examined using the Kruskal-Wallis test. Significant differences between pairs of variables were determined with the Wilcoxon rank sum test, where the p-value was adjusted according to the Bonferroni multi-comparisons procedure. $p < 0.05$ was considered significant.

4.2.4 Histology

At the end of the 6 h investigation period, biopsies of the tibialis anterior muscle were taken from both experimental and control legs. The tissues were snap-frozen in melting isopentane and stored at -80 °C. Frozen samples were cut in transversal direction in 5 μm thick sections and stained with haematoxylin and eosin.

4.3   Results

4.3.1   DCE-MRI

Figure 4.3 shows a representative example of the temporal concentration of the contrast agent in three regions of interest (ROIs) in the leg. In the initial pre-ischaemic DCE-MRI scan (figure 4.3a-b), the concentration showed a similar profile in each area. This was characterised by an initial increase after administration, followed by a second small rise in concentration up to $\sim$0.1 mM. In the post-ischaemic situation (figure 4.3d-e), large spatial differences were evident. In some areas, the peak concentration exceeded pre-ischaemic levels reaching values of $\sim$0.3 mM (ROI 1). However, such a steep increase was often followed by a rapid decrease in concentration. There were also areas for which the influx of contrast agent was almost absent (ROI 3).
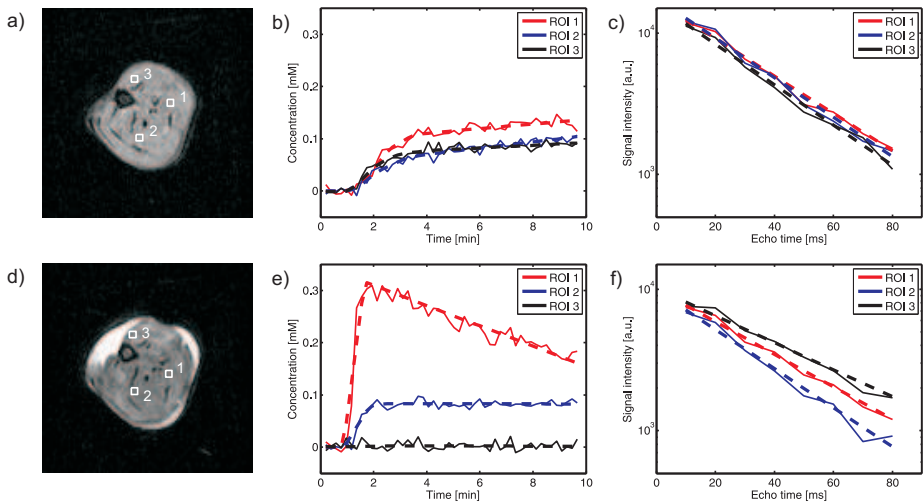
Figure 4.3: a-b) Mean concentration (solid line) and mean piecewise linear fit (dashed line) of the concentration in time in three ROIs in the leg of one animal during the initial pre-ischaemic DCE-MRI scan. c) Mean T_2-weighted signal intensity (solid) and mean fitted curve (dashed) in the three ROIs during the pre-ischaemic T_2 scan (plotted on a logarithmic scale). d-e) Mean concentration (solid line) and mean piecewise linear fit (dashed line) during the second post-ischaemic DCE-MRI scan. f) Mean T_2-weighted signal intensity (solid) and mean fitted curve (dashed) during the second post-ischaemic T_2 scan (plotted on a logarithmic scale).

Figure 4.4 displays a representative example (the same animal as in figure 4.3) of the spatial distribution of the four contrast enhancement parameters, b_1, b_2, C_p, and A, at different time points during the experimental protocol. All parameters showed a homo-

geneous distribution during the pre-ischaemic DCE-MRI scan (figures 4.4a-d). After the initial rise in concentration with slope b_1 (figure 4.4a), a second gradual increase was observed with slope b_2 (figure 4.4b). During ischaemia, all parameter values in the complete leg were essentially reduced to zero, confirming the ischaemic condition (figures 4.4e-l). In the post-ischaemic situation, all parameters showed a heterogeneous distribution (figures 4.4m-t). There were areas in which no-reflow was present (solid arrows in figure 4.4), most clearly characterised by very small values of A. The locations of these distinct areas of no-reflow were similar in all experiments. By contrast, some areas (dashed arrows in figures 4.4) exhibited a very steep initial rise in concentration in the post-ischaemic phase (slope b_1, figures 4.4m,q). In these areas, considerably higher peak concentrations were reached (figures 4.4o,s), followed by a more rapid washout of the contrast agent, as characterised by the negative values for slope b_2 (figures 4.4n,r).
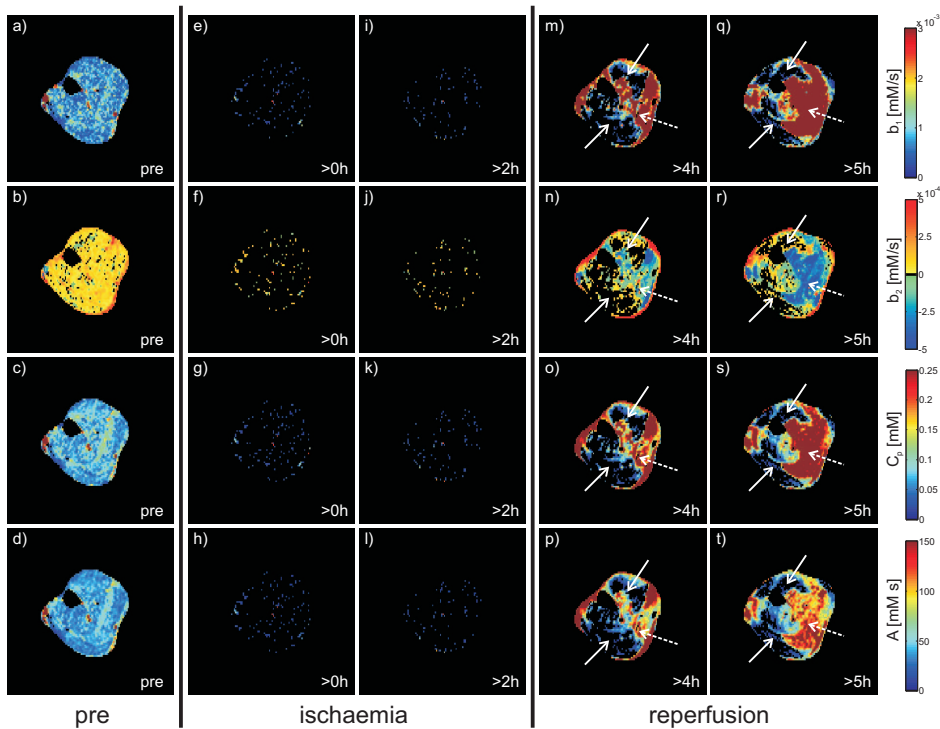
Figure 4.4: Representative example (same animal as in figure 4.3) of the spatial distribution of the four contrast enhancement parameters. a-d) Before ischaemia was applied. e-l) During ischaemia. m-t) During the post-ischaemic phase (solid arrows: areas with absent post-ischaemic contrast enhancement; dashed arrows: areas with increased contrast enhancement).

To quantify these associations between the different contrast enhancement parameters during the post-ischaemic situation, the Spearman rank correlation coefficient r_s was calculated (table 4.1). Very strong positive correlations were found between each combination of b_1, C_p, and A. By contrast, negative correlations of b_2 with the other three parameters were obtained, which were particularly marked during the second post-ischaemic DCE-MRI scan ($t > 5$ h). All correlations were statistically significant with $p \ll 0.001$. Thus, a rapid influx of contrast agent during the post-ischaemic phase resulted in higher peak concentrations, followed by an accelerated washout of the contrast agent.

Table 4.1: Spearman rank correlation coefficient r_s between the contrast enhancement parameters in all experiments during the first ($t > 4$ h) and second ($t > 5$ h) post-ischaemic DCE-MRI scan. Correlations were statistically significant ($p \ll 0.001$) between all parameters.

	b_1-b_2	b_1-C_p	b_1-A	b_2-C_p	b_2-A	C_p-A
$t > 4$ h	-0.41	0.98	0.97	-0.34	-0.26	0.99
$t > 5$ h	-0.62	0.98	0.97	-0.56	-0.47	0.99

Figure 4.5 illustrates the relative proportions of the three subgroups (low, normal, and high) of parameter b_1 with time for the different animals. The choice of the threshold levels for the subgroups was such that approximately 90 % of the leg represented the normal category during the initial DCE-MRI scan. During ischaemia, low values of b_1 were evident almost throughout each of the legs. The two post-ischaemic DCE-MRI scans show that perfusion did not return in the complete leg immediately after release of the vessel loop in all animals, represented by the lack of contrast enhancement in those areas. In rats 1 and 3, a partial shift of b_1 from the low to the high subgroup was present during the post-ischaemic phase (figure 4.5a,c), whereas the opposite was observed for rats 2 and 4 (figure 4.5b,d). The results for the relative subgroup proportions of b_2, C_p, and A demonstrated similar trends to the results for b_1, due to the strong correlations between all contrast enhancement parameters.
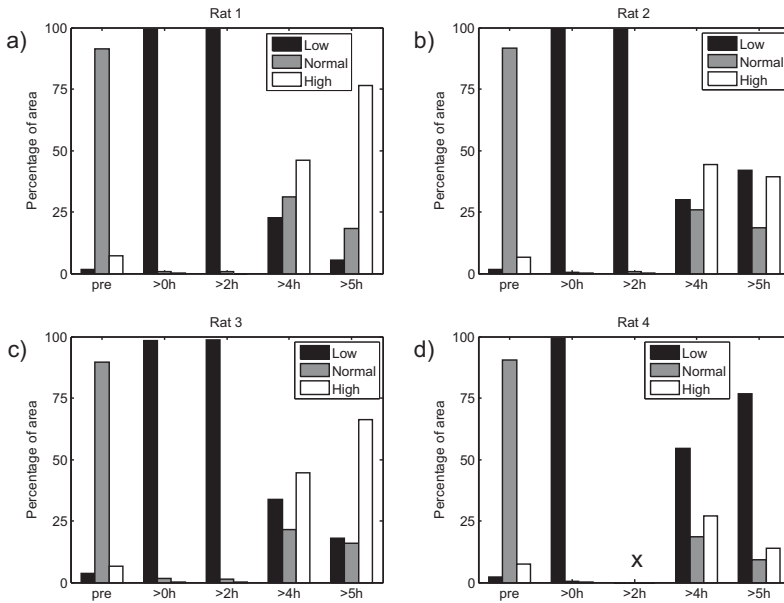
Figure 4.5: Time course of the relative subgroup proportions (low, normal, and high) of b_1 in the leg with time. a) Rat 1 ($t_l = 2.7\cdot10^{-4}$ mM/s, $t_h = 1.6\cdot10^{-3}$ mM/s). b) Rat 2 ($t_l = 2.7\cdot10^{-4}$ mM/s, $t_h = 1.7\cdot10^{-3}$ mM/s). c) Rat 3 ($t_l = 2.1\cdot10^{-4}$ mM/s, $t_h = 1.3\cdot10^{-3}$ mM/s). d) Rat 4 ($t_l = 3.2\cdot10^{-4}$ mM/s, $t_h = 1.6\cdot10^{-3}$ mM/s). The second DCE-MRI scan during ischaemia is missing for rat 4, indicated by the symbol x.

4.3.2 T_2-weighted MRI

The spatial differences in T_2 are illustrated in figure 4.3. The pre-ischaemic T_2 scan shows similar T_2 values in three different ROIs in the leg (figure 4.3c), whereas large spatial differences in T_2 were present during the post-ischaemic phase (figure 4.3f). The time course of T_2 during one of the I-R experiments (the same animal as in figures 4.3 and 4.4) is depicted in figure 4.6. The transverse relaxivity r_2 of ProHance was esti-mated at 12 mM^{-1} s^{-1} and used to correct T_2 for the local concentration of the contrast agent. Both the measured and corrected T_2 showed a homogeneous distribution before ischaemia (figure 4.6a,b), with a gradual increase in T_2 in the complete leg during the is-chaemic period (figure 4.6c-f). During the post-ischaemic phase, T_2 increased in specific areas (solid arrows in figure 4.6), and decreased in other areas (dashed arrows in figure 4.6). The locations of these distinct areas were similar in all experiments.
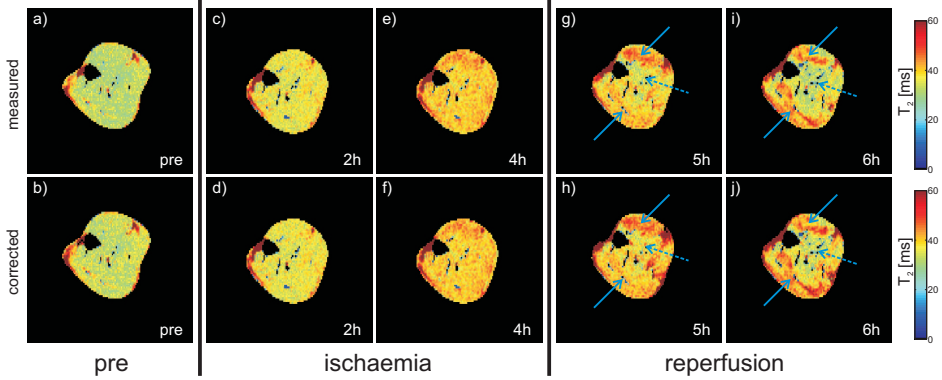
Figure 4.6: Representative example of the time course of the measured T_2 and T_2 corrected for the local concentration of ProHance. a-b) Before ischaemia was applied. c-f) During ischaemia. g-j) During the post-ischaemic phase (solid arrows: areas with a further increase in T_2; dashed arrows: areas with a decrease in T_2).

4.3.3   Comparison of contrast enhancement and T_2

For the post-ischaemic phase, figures 4.4 and 4.6 show that areas exhibiting a decrease in T_2 were associated with high values for contrast enhancement parameters b_1, C_p, and A, whereas regions with an increase in T_2 were associated with regions of no-reflow (represented by the low values of b_1, C_p, and A). As a strong correlation was found between all contrast enhancement parameters, the local quantitative comparison of contrast enhancement with T_2 is only shown for parameter b_1. Parameter b_1 was chosen since the initial rise of the signal intensity or concentration curve is often used in semi-quantitative analyses to estimate perfusion (Kraitchman et al., 1996; Al-Saadi et al., 2000; Jerosch-Herold et al., 2004). Moreover, Luo et al. (2002) have shown that in rat skeletal muscle a perfusion index derived from the initial Gd-DTPA uptake rate is proportional to perfusion measured using radionuclide-labelled microspheres. Figure 4.7 depicts the time course of T_2 in the complete leg before and during ischaemia, and for each of the three b_1 subgroups during the post-ischaemic phase for all experiments. Significant differences of T_2 with time or between subgroups are displayed in table 4.2. During ischaemia, T_2 increased significantly with time. For the post-ischaemic phase, the time course of T_2 was different per subgroup of b_1, where T_2 increased for the low b_1 subgroup and decreased for the high b_1 subgroup. At 6 h, a clear negative association between T_2 and b_2 was present.
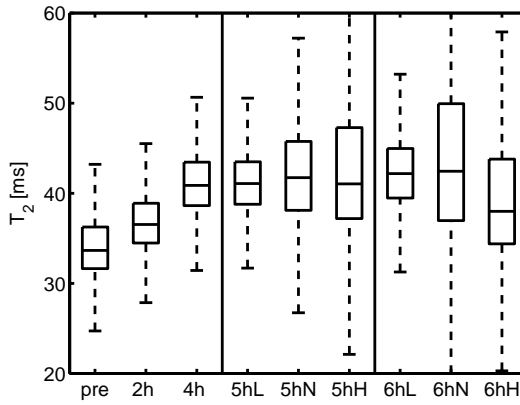
Figure 4.7: Boxplot of T_2 in the complete leg in all experiments before and during ischaemia, and for each of the three b_1 subgroups during the post-ischaemic phase. T_2 was corrected for the local concentration of ProHance. Symbols L, N, and H denote the low, normal and high b_1 subgroup, respectively.

Table 4.2: Significant differences of T_2 in time and between b_1 subgroups. T_2 was corrected for the local concentration of ProHance. Symbols L, N, and H denote the low, normal and high b_1 subgroup, respectively.

Comparison	Significant differences
With time during ischaemia	$T_{2,\mathrm{pre}} < T_{2,\mathrm{2h}} < T_{2,\mathrm{4h}}$
With time for low b_1	$T_{2,\mathrm{4h}} < T_{2,\mathrm{6hL}}$; $T_{2,\mathrm{5hL}} < T_{2,\mathrm{6hL}}$
With time for normal b_1	$T_{2,\mathrm{4h}} < T_{2,\mathrm{5hN}}$; $T_{2,\mathrm{4h}} < T_{2,\mathrm{6hN}}$
With time for high b_1	$T_{2,\mathrm{4h}} > T_{2,\mathrm{6hH}}$; $T_{2,\mathrm{5hH}} > T_{2,\mathrm{6hH}}$
At 5h	$T_{2,\mathrm{5hN}} > T_{2,\mathrm{5hH}}$
At 6h	$T_{2,\mathrm{6hL}} > T_{2,\mathrm{6hN}} > T_{2,\mathrm{6hH}}$

4.3.4   Histology

Haematoxylin and eosin stainings of the tibialis anterior muscles of both control and experimental legs are shown in figure 4.8. The tibialis anterior muscle in the control leg displayed a normal polygonal appearance of muscle fibres with few interstitial spaces (figure 4.8a). At the end of the I-R experiments, morphological changes were evident throughout the muscle, although there were clear regional differences in the severity of these changes (figure 4.8b). In some regions, only small alterations were observed (figure 4.8c), whereas in other areas rounded hypertrophic fibres and increased interstitial spaces were evident (figure 4.8d).
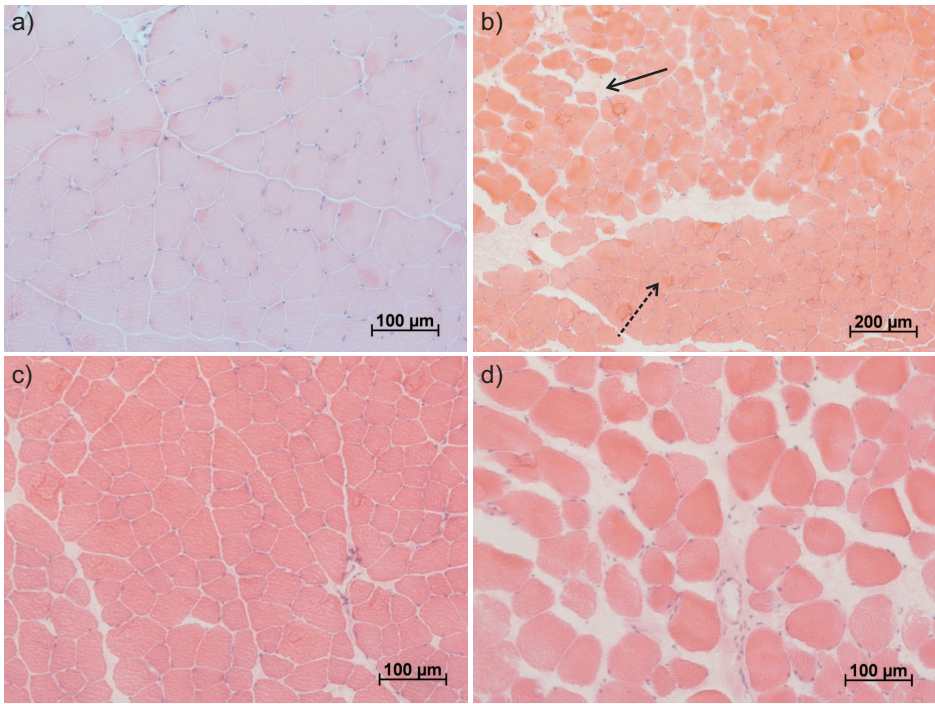
Figure 4.8: Haematoxylin and eosin stainings of cross-sections of the tibialis anterior muscle. a) Healthy tissue from the control leg, showing a normal polygonal appearance of muscle fibres and few interstitial spaces. b) After 4 h ischaemia and 2 h reperfusion. In some areas (solid arrow), changes in tissue structure were more severe than in other areas (dashed arrow). c) Example of minor alterations after 4 h ischaemia and 2 h reperfusion. d) Example of more severe morphological changes after 4 h ischaemia and 2 h reperfusion (rounded hypertrophic cells, increased interstitial spaces).

4.4   Discussion

In the present study, the local interrelation between post-ischaemic contrast enhancement and changes in T_2 in skeletal muscle was investigated. Animal experiments with Brown-Norway rats were performed in which 4 h ischaemia was applied to the left hindlimb of each animal, followed by 2 h reperfusion. During ischaemia, T_2 increased gradually with time in the complete leg (figure 4.6). The post-ischaemic DCE-MRI scans showed a highly heterogeneous pattern, consisting of areas with a considerable increase in contrast enhancement when compared to the initial DCE-MRI scan before ischaemia, and also areas with no-reflow (figure 4.4). The locations of these regions were similar across the experiments and also showed a clear correlation with T_2. A decrease in T_2 toward control values was observed in areas with high post-ischaemic contrast enhancement, whereas areas with no-reflow exhibited a further increase in T_2 during the reperfusion phase (figure 4.6).

Contrast enhancement in the hindlimb was investigated with DCE-MRI using an intra-venous bolus injection of ProHance. The resulting local time profile of the concentration of contrast agent in the leg was determined, and a semi-quantitative analysis was applied to characterise each time profile with four parameters. The present data analysis is quantitative in nature involving an analysis of the temporal profile of the contrast agent concentration, as opposed to signal intensity curves. In addition, the initial upslope is often used as a measure for perfusion, and is suitable to detect spatial differences in perfusion (Jerosch-Herold et al., 2004). However, parameters that were derived from the piecewise linear fit can not be directly related to physiological mechanisms. The use of a quantitative tracer kinetic model, such as the two-compartment Tofts model (Tofts et al., 1999), would produce parameters that reflect the (patho)physiology more accurately. This, however, requires the knowledge of an arterial input function, which was not possible in the present study as damage to blood vessels was most likely in the post-ischaemic phase.

Changes in skeletal muscle properties were monitored with T_2-weighted MRI, where an increase in T_2 was considered a measure of tissue damage (Fleckenstein, 1996). However, several pathological mechanisms, which can not be distinguished, can all contribute to the increase in T_2. Therefore, histological analyses were performed that revealed a different tissue structure after 4 h ischaemia and 2 h reperfusion when compared to healthy tissue of the control leg (figure 4.8). At the end of the I-R experiments, rounded hypertrophic muscle fibres and increased interstitial spaces were present, that probably caused the increase in T_2. These histological changes may be the result of osmotic water shifts due to disturbed intracellular ion concentrations and the accumulation of waste products of anaerobic metabolism during ischaemia (Stekelenburg et al., 2007). During the reperfusion phase, tissue swelling and thereby T_2 may have decreased in particular areas due to restoration of ion homeostasis and removal of waste products. On the other hand, damage to blood vessels and cell membranes could have caused an increase in swelling and T_2 in other areas. In previous studies, similar alterations in tissue structure after ischaemia and reperfusion were reported (Carmo-Araújo et al., 2007; Hashimoto et al., 2008). Spatial differences in the severity of these changes in the muscle were also observed. In the present study, however, it proved not possible to exactly coregister MRI and histological slices for a local comparison of T_2 and DCE-MRI with histology, because of the lack of geometrical information on the histological slices and deformation of the ex vivo tissues.

T_2 was determined frequently during each experiment in combination with DCE-MRI. As the contrast agent that was required for the DCE-MRI scans decreases both T_1 and T_2, the influence of ProHance on T_2 was investigated in three experiments. Subsequently, the T_2 maps of the I-R experiments were corrected for this effect based on the concentration of contrast agent at the end of the preceding DCE-MRI scan (figure 4.6). The influence of ProHance on T_2 appeared to be small, due to relatively low concentrations

in the leg during the pre-ischaemic DCE-MRI scan, and a rapid washout of contrast agent during the post-ischaemic phase. Furthermore, the real concentration is probably much lower during the T_2 scan than at the end of the preceding DCE-MRI scan. Therefore, the correction of T_2 that was applied in the present study represents an overestimation of the influence of ProHance. Moreover, in I-R experiments of Morikawa et al. (1991), where no contrast agent injections were used, a similar heterogeneous T_2 profile in skeletal muscle of the rat hindlimb was also reported. Therefore, although the contrast agent had a small influence on T_2, this effect was not large enough to significantly influence the results, and measuring perfusion and T_2 in the same experiment also enabled the local comparison of the heterogeneous spatial distributions of contrast enhancement and T_2.

The areas of high post-ischaemic contrast enhancement were characterised by a rapid initial upslope of the concentration curve, possibly reflecting hyperaemia (figure 4.4). This initial fast uptake of contrast agent was strongly correlated with a rapid washout, which may be a result of increased vascular permeability (Tofts et al., 1995; Lavini et al., 2007). The response in this region was associated with a decrease in T_2 (figure 4.6), which corresponds with the results of the I-R experiments of Morikawa et al. (1991) that also showed a decrease in signal intensity in T_2-weighted images in this region. It is probable that the muscle changes after 4 h ischaemia were still reversible, so that T_2 could decrease toward pre-ischaemic values during reperfusion. Thus, no signs of I-R injury, e.g. by reactive oxygen species, were observed in this region.

Regions with no-reflow demonstrated an increase in T_2 during the post-ischaemic phase (figure 4.6). No-reflow is a feature of I-R injury and can be caused by microvascular thrombosis, vasospasm, or oedema (Urbaniak et al., 1997; Blaisdell, 2002). The two major regions of no-reflow were located in the anterior tibial and superficial posterior compartments of the leg, also corresponding with the results of Morikawa et al. (1991). Therefore, oedema may have caused an elevated compartmental pressure that was sufficient to close the blood vessels. This acute compartment syndrome is known to occur in the anterior tibial compartment, which is rigidly bound by the tibia, fibula, interosseus septum, and deep fascia, but it is less common for the superficial posterior compartment (Beraldo and Dodds, 2006). On the other hand, Urbaniak et al. (1997) found that a regional no-reflow phenomenon in muscle tissue was often restricted to localised areas of the vascular network. Therefore, the specific architecture of the blood vessels in the leg may also play a role in the local pattern of no-reflow that was observed in the present study. As muscles predominating in fast-twitch fibres are more susceptible to I-R injury, the distribution of the different muscle fibre types in the hindlimb might also contribute to the heterogeneous pattern (Chan et al., 2004). However, the influence of this effect on the results of the present study may be negligible, since the vast majority of muscle groups in the rat hindlimb is mainly composed of fast-twitch fibres (Armstrong and Phelps, 1984). The no-reflow regions were associated with a further increase in T_2

after the ischaemic period (figure 4.6). If no-reflow was caused by the compartment syndrome, this increase in T_2 may be a result of extensive swelling in the tissue during reperfusion before the vessels collapsed. On the other hand, the rise in T_2 could also be explained by the additional 2 h of local ischaemia.

In summary, the roles of ischaemia and reperfusion in the aetiology of DTI were investigated in the present study. For this, T_2-weighted and DCE-MRI were applied to study changes in skeletal muscle integrity and perfusion. The combination of both techniques within the same experiment enabled the local comparison of the heterogeneous T_2 and contrast enhancement profiles, although T_2 values had to be corrected for the presence of contrast agent. The DCE-MRI data revealed the presence of no-reflow areas in the hindlimb, that were associated with a further post-ischaemic increase in T_2. For skeletal muscle tissue that is subjected to prolonged periods of mechanical loading associated with ischaemia, these results show that reperfusion after prolonged ischaemia may not be complete, thereby continuing the ischaemic condition and aggravating tissue damage. Clearly, the influence of reperfusion on ultimate pressure ulcer development is complex and requires further investigation, particularly when considering changes associated with spinal cord injury. Additionally, its effects must be considered when designing appropriate repositioning strategies for at-risk individuals.

Acknowledgements

Chapter 5

The effects of deformation, ischaemia, and reperfusion on the development of muscle damage during prolonged loading

5.1   Introduction

Pressure ulcers are localised areas of tissue degeneration that occur in bedridden or wheelchair-bound individuals as a result of sustained mechanical loading. For example, their occurrence is a major secondary complication for spinal cord injured individuals (McKinley et al., 1999; Garber and Rintala, 2003), which can seriously affect their quality of life. In addition, the treatment of pressure ulcers and related complications represents a financial and human burden in terms of extended hospitalisation and possible surgical interventions (Bennett et al., 2004; Brem et al., 2010).

Deep tissue injury (DTI) is a severe form of pressure ulcer where tissue damage starts in subcutaneous tissue layers, such as skeletal muscle, underneath intact skin (Ankrom et al., 2005; Black et al., 2007). DTI represents a serious problem, because tissue damage only becomes apparent at the skin surface at an advanced stage, at which time treatment becomes problematic and several complications can occur (Thomas, 2001; Brem et al., 2010). Therefore, early identification of DTI and subsequent treatment are critical to reduce comorbidities and costs (Brem et al., 2010). This requires a better understanding of the aetiology of DTI, in order to develop appropriate risk assessment tools and early detection methods.

Compression-induced ischaemia is traditionally considered to represent the most important factor in the aetiology of DTI (Kosiak, 1959; Daniel et al., 1981). More recently, other theories have been proposed, including ischaemia-reperfusion (I-R) injury (Peirce et al., 2000; Tsuji et al., 2005), impaired lymphatic drainage (Miller and Seale, 1981), and sustained tissue deformation (Bouten et al., 2001; Gawlitta et al., 2007a; Linder-Ganz et al., 2007; Stekelenburg et al., 2007; Ceelen et al., 2008b). For example, in a rat model, deformation was reported to be the primary determinant for skeletal muscle damage for loading periods up to 2 h (figure 5.1). This damage, however, was confined to specific regions of the muscle, despite the fact that the complete muscle was ischaemic during loading (Stekelenburg et al., 2007). In addition, dedicated finite element (FE) models of Ceelen et al. (2008b) demonstrated that these regions of damage coincided with those regions subjected to the largest deformations, and that damage only occurred if a specific deformation threshold was exceeded. Moreover, a correlation between the amount of damage and deformation was found, and recent observations have suggested that the deformation threshold for muscle damage appears to be similar for a range of loading conditions (Loerakker et al., 2010).
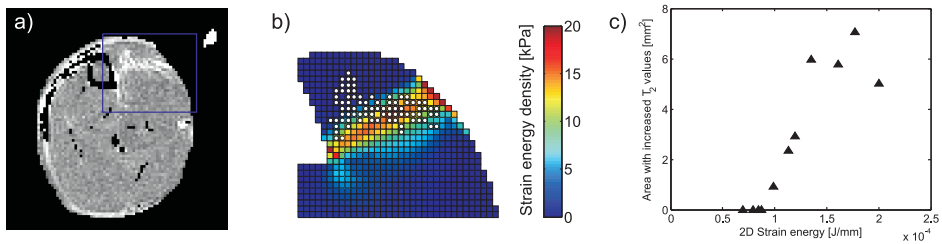
Figure 5.1: a) T_2 map obtained from T_2-weighted magnetic resonance (MR) images of a cross-section of a rat leg, indicating that muscle damage (area with increased T_2, high-intensity (white) pixels) due to 2 h compression only occurred in a small region of the muscle. b) The internal strain energy density distribution estimated with FE models showed an overlap with the damaged region in the tissue. c) The total strain energy in the muscle clearly correlated with the amount of tissue damage once a specific threshold value was exceeded. (Adapted from Loerakker et al. (2010).)

In clinical practice, however, where individuals are often exposed to prolonged loading, it might be predicted that ischaemia plays an increasingly important role in the damage process. In addition, repositioning strategies and pressure-relieving mattresses are employed to periodically unload and thereby stimulate reperfusion of tissue areas at risk of developing ischaemic injury. It is generally accepted that reperfusion after an ischaemic period is beneficial for the tissue to reverse the changes that occur during ischaemia. However, reperfusion can also aggravate tissue damage due to the combined activation of reactive oxygen species, inflammation, and oedema. Indeed, it was shown in a rat model that an increasing number of I-R cycles was more damaging to the skin of rats than continuous ischaemia alone (Peirce et al., 2000). Moreover, a separate study reported that muscle damage was less extensive after 2.5 h ischaemia if gradual reperfusion was used as compared to instantaneous reperfusion (Ünal et al., 2001). Therefore, it may be hypothesised that the contributions of ischaemia and reperfusion to the damage process increase with prolonged loading. To test this hypothesis, the effects of deformation, ischaemia, and reperfusion on muscle damage development were investigated in a rat model for DTI during a 6 h period using magnetic resonance imaging (MRI).

5.2   Materials & Methods

5.2.1   Animal model

A previously developed animal model was used to study the effects of both deformation and ischaemia (Stekelenburg et al., 2006a,b). Sixteen 4-5-month old female Brown-Norway rats, weighing between 157 and 190 g, were used. The animals were housed under well-controlled laboratory conditions (12 h light, 12 h dark cycles), and maintained

on standard chow and water ad libitum. At the start of the experiment, the animals were anaesthetised with 0.6 L/min medical air with 3 % isoflurane for induction and 1-2 % for maintenance. Respiratory rate and rectal temperature were monitored and maintained within the physiological range. A heating pad was used to maintain body temperature between 36 and 37 °C.

Hairs of the left hindlimb were removed by shaving, after which the lower leg was placed in a specially designed mold and fixated with plaster cast. A water-filled capillary was embedded in the plaster cast as a reference point for comparison between MRI acquisitions. A hole in the cast was created to enable compression of the tibialis anterior (TA) muscle with an MR-compatible cylindrical indenter (diameter 3 mm, length 6 mm, attached to a rod), as described previously (Ceelen et al., 2008b; Loerakker et al., 2010). A catheter was implanted in the jugular vein to enable the administration of contrast agent in order to investigate perfusion. Each rat was placed supine in the experimental setup, which consists of two concentric tubes, as detailed in Stekelenburg et al. (2006a,b). The inner tube housed the animal, and the outer tube was used to position the animal in a 6.3 T MR scanner (Bruker BioSpin, horizontal bore, inner diameter 120 mm) with a 400 mT/m gradient coil. The left foot was positioned within a special holder, and a birdcage radio-frequency coil was placed around the lower leg in a fixed position.

Four different loading protocols were applied, as illustrated in figure 5.2a. In group I (n = 4), 6 h ischaemia was applied with a silicone vessel loop (Identi Loops supermaxi blue, Dispo Medical), which was applied around the thigh to restrict blood flow in the complete lower leg. In group II (n = 4), the vessel loop was removed after 4 h to enable reperfusion. Experimental data for this group have recently been reported separately as well (Loerakker et al., 2011). In group III (n = 4), the TA muscle was compressed with the indenter. After 4 h compression, a vessel loop was applied to cause complete ischaemia for another 2 h and the indenter was removed. In group IV (n = 4), the TA muscle was compressed with the indenter for 4 h, after which the indenter was removed to enable reperfusion. The effect of reperfusion was examined by comparing the results of group I and II. The relative effects of deformation and ischaemia were investigated by comparing the results of group I with group III and group II with group IV.

At the end of the 6 h investigation period in each loading protocol, the TA muscles were taken from both experimental and control legs, and the animals were sacrificed. The tissues were snap-frozen in melting isopentane and stored at -80 °C. Frozen samples were cut in transversal direction in 5 μm thick sections and stained with haematoxylin and eosin. The experimental protocol was approved and supervised by the Animal Care Committee of Maastricht University.
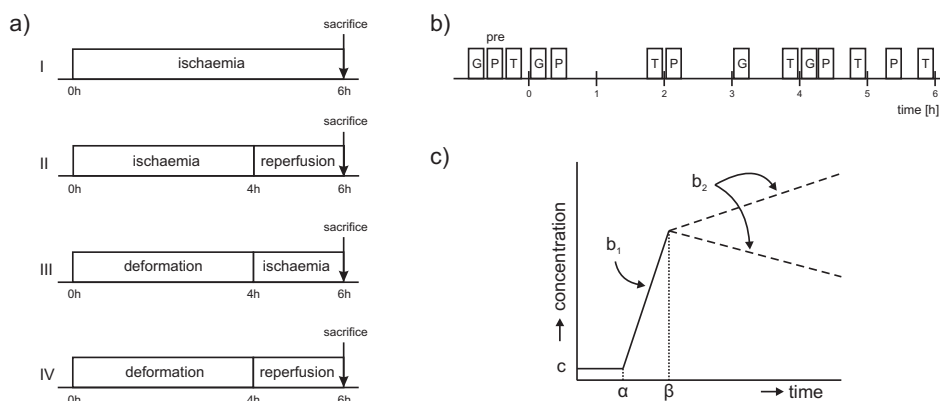
Figure 5.2: a) Overview of the combinations of deformation, ischaemia, and reperfusion in the four experimental groups. Group I: 6 h ischaemia; group II: 4 h ischaemia followed by 2 h reperfusion; group III: 4 h deformation followed by 2 h ischaemia; group IV: 4 h deformation followed by 2 h reperfusion. b) Time schedule of the different MRI acquisitions: G = transversal scout images to assess the geometry of the leg, P = DCE-MRI to investigate the perfusion, T = T_2-weighted MRI to monitor changes in tissue integrity. c) The time course of $C(t)$ was characterised by fitting the data of each voxel to a piecewise linear fit model consisting of three line segments with intersection points α and β. The first segment represents the baseline concentration (c), the second segment with slope b_1 describes the rapid increase in $C(t)$, and the third phase has slope b_2, which can be either positive or negative. (Adapted from Loerakker et al. (2011), with permission.)

5.2.2   MR measurements

High-resolution transversal scout images (FOV = 25×25 mm^2, matrix size = 256×256) were obtained during the experiment to assess the geometry of the rat leg. Dynamic contrast-enhanced MRI (DCE-MRI) was used to calculate local contrast enhancement parameters, and changes in muscle integrity were assessed with T_2-weighted MRI several times during the 6 h investigation period of each experiment. The time schedule of the MR measurements is illustrated in figure 5.2b.

Dynamic contrast-enhanced MRI

Local contrast enhancement in the leg following an intravenous injection of paramagnetic contrast agent ProHance (Gd-HP-DO3A, Bracco Diagnostics Inc.) was measured using a 3D dynamic series of T_1-weighted FLASH (RF- and gradient-spoiled) sequences with the following imaging parameters: FOV = $25 \times 25 \times 17.6$ mm^3, matrix size = $128 \times 96 \times 16$, TR = 10 ms, TE = 2.8 ms, and flip angle $\alpha = 15°$. After four baseline image acquisitions, a 100 μL bolus of ProHance (0.2 mmol/kg) was administered via the catheter in the jugular vein, while image acquisition was continued for a further 45 scans. The local time profile of T_1 was determined as described in Loerakker et al.

(2011), and the concentration of contrast agent $C(t)$ in each voxel was calculated from the change in T_1 according to:

$$C(t) = \frac{1}{r_1} \left(\frac{1}{T_1(t)} - \frac{1}{T_{1,\text{pre}}} \right)$$

(5.1)

where r_1 represents the T_1 relaxivity of the contrast agent, equal to approximately 3 mM^{-1} s^{-1} at 6.3 T (Laurent et al., 2006; Blockley et al., 2008).

To characterise the time course of contrast enhancement, a piecewise linear fit was applied to $C(t)$ in each voxel (Singh et al., 2009). As illustrated in figure 5.2c, each curve was divided into three linear phases (Singh et al., 2009; Loerakker et al., 2011): a constant baseline phase, a rapid initial rise in $C(t)$, and a subsequent phase in which $C(t)$ can be either increasing or decreasing:

$$C_{\text{fit}}(t) = \begin{cases} c & \text{for } t \leq \alpha \\ c + b_1(t - \alpha) & \text{for } \alpha \leq t \leq \beta \\ c + b_1(\beta - \alpha) + b_2(t - \beta) & \text{for } t \geq \beta \end{cases}$$

(5.2)

where α and β are the intersection time points between the line segments, c is the baseline concentration before contrast agent administration, and b_1 and b_2 are the slopes of the second and third line segment, respectively. Constants c, b_1, and b_2 were derived by fitting $C_{\text{fit}}(t)$ to $C(t)$ using the least squares method, and α and β were varied until the difference between $C_{\text{fit}}(t)$ and $C(t)$ was minimal. Parameter b_1 was chosen as perfusion index, since the initial rise in the signal intensity or concentration curve is often used to estimate perfusion (Al-Saadi et al., 2000; Luo et al., 2002; Jerosch-Herold et al., 2004). From the b_1 distribution in the initial DCE-MRI scan, the 25th (p_{25}) and 75th (p_{75}) percentile and the interquartile range $r_{\text{IQ}} = p_{75} - p_{25}$ were calculated. For each experiment, a threshold equal to $p_{25} - r_{\text{IQ}}$ was set to distinguish between ischaemic (b_1 lower than threshold) and perfused areas in subsequent DCE-MRI acquisitions.

T_2-weighted MRI

Changes in muscle integrity were monitored with T_2-weighted MRI, using a multi-echo spin echo sequence (FOV = 25×25 mm^2, matrix size = 128×128, slice thickness = 1 mm, 11 slices, TR = 4 s, TE = 10-320 ms, 32 echoes, and fat suppression using a spectrally-selective 90 ° pulse followed by a spoiler gradient). A quantitative T_2 map was obtained

by fitting the signal intensity S of the first eight echoes to:

$$S = S_0 e^{-TE/T_2} \tag{5.3}$$

T_2 was corrected for the influence of ProHance, as recently detailed in Loerakker et al. (2011).

Comparison of contrast enhancement and T_2

The b_1 and T_2 data were coregistered in four consecutive MR slices. The high-resolution scout images (figure 5.2b) were used to define the outer boundary of the leg and the tibia in each slice. Between these two boundaries, a grid was defined with the resolution of the DCE-MRI data (distance between grid points 25/128 mm and 25/96 mm in horizontal and vertical directions, respectively). Subsequently, this grid was mapped to the corresponding slices in the DCE-MRI data based on the contours of the leg, and the pixel values of b_1 were linearly interpolated onto the grid points. The same procedure was applied to the T_2 maps, to enable comparison of b_1 with T_2 at identical locations.

5.2.3   Finite element model

To estimate the deformation of the muscle tissue during indentation in groups III and IV, dedicated plane stress FE models were developed for four MR slices underneath the indenter for each animal, as described in Loerakker et al. (2010). The outer boundaries of the leg and tibia, as determined from the initial scout images, were used to create the mesh (figure 5.3a). The tibia was considered rigid, and the muscle tissue was modelled as an incompressible single-mode hyperelastic Ogden material with strain energy density W:

$$W = \frac{\mu}{\alpha}(\lambda_1^\alpha + \lambda_2^\alpha + \lambda_3^\alpha - 3) \tag{5.4}$$

where λ_i ($i = 1, 2, 3$) are the principal stretch ratios, $\mu = 3.6$ kPa, and $\alpha = 5$ (Loerakker et al., 2010).

From scout images of the deformed leg, the movement of the tibia during indentation, and the angle and depth of indentation were derived (figure 5.3b). The displacements of the tibia and the indenter were prescribed as essential boundary conditions. Coulomb

friction was assumed between the leg and the indenter, where the friction coefficient was adjusted between 0 and 1 for each FE model to optimise the correspondence of the outer contour of the leg during indentation between experiment and simulation, as determined by visual inspection. The plaster cast surrounding the leg was modelled as a rigid body in free-slip contact with the leg (figure 5.3c). The FE model was implemented in MSC.Marc (MARC Analysis Research Corporation, 2005). A region of interest, covering the TA muscle, was selected for each model (Loerakker et al., 2010). To obtain a global measure of deformation, the 2D strain energy was calculated by integrating W over this area.
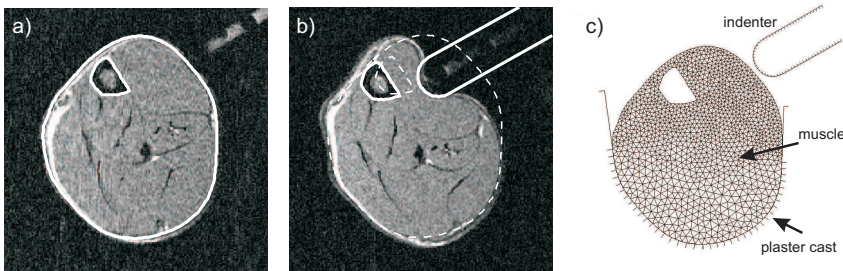
Figure 5.3: a) Transversal scout image of the rat leg before compression. The outer contours (white lines) of the leg and tibia were used for mesh generation. b) The displacement of the tibia and the angle and depth of indentation were derived from the scout image during loading (original mesh contours shown by dashed lines). c) Resulting FE mesh with indenter and plaster cast modelled as rigid bodies. (From Loerakker et al. (2010).)

5.2.4   Comparison of experimental groups

For group I, the median T_2 in the leg (in all four MR slices) was determined for each animal at each time point. For group II, this was done similarly for the T_2 maps during the ischaemic phase. Since reperfusion in this group was not homogeneous throughout the leg, the median T_2 was determined separately for areas with and without reperfusion, which were distinguished using a threshold for b_1. For group III, only the T_2 values in the TA muscle region were considered because this area was subjected to deformation. During deformation, only the ischaemic area of the TA muscle was selected. For group IV, the same approach was used during deformation. During the reperfusion phase, the median T_2 in the TA muscle was determined separately for the areas with and without reperfusion, similar to the approach adopted for group II. For experiments in group III and IV, the strain energy as determined from the FE model was averaged over the four slices and compared with T_2 at the end of the experiment and the level of ischaemia in the leg during deformation. A one-way ANOVA was used to examine differences in

T_2 between experimental groups and time points. Significant differences between pairs were determined using a Bonferroni post-hoc test with $p < 0.05$ considered significant.

5.3   Results

The main results of the four experimental groups are summarised in table 5.1.

Table 5.1: Overview of the main findings from the four experimental groups.

Group	Main findings
I	Perfusion was absent during application of the vessel loop. T_2 increased gradually in the complete leg.
II	Heterogeneous b_1 pattern after removal of the vessel loop. T_2 was larger in no-reflow areas when compared to reperfused areas.
III	Partial ischaemia of the leg during compression followed by complete ischaemia. T_2 increased mainly in large parts of the compressed TA muscle. Levels of ischaemia, deformation, and T_2 varied considerably between experiments.
IV	Partial ischaemia of the leg during compression. After compression, reperfusion of the TA muscle was present in three of the four animals. T_2 increased in large parts of the compressed TA muscle. Levels of ischaemia, deformation, and T_2 varied considerably between experiments.
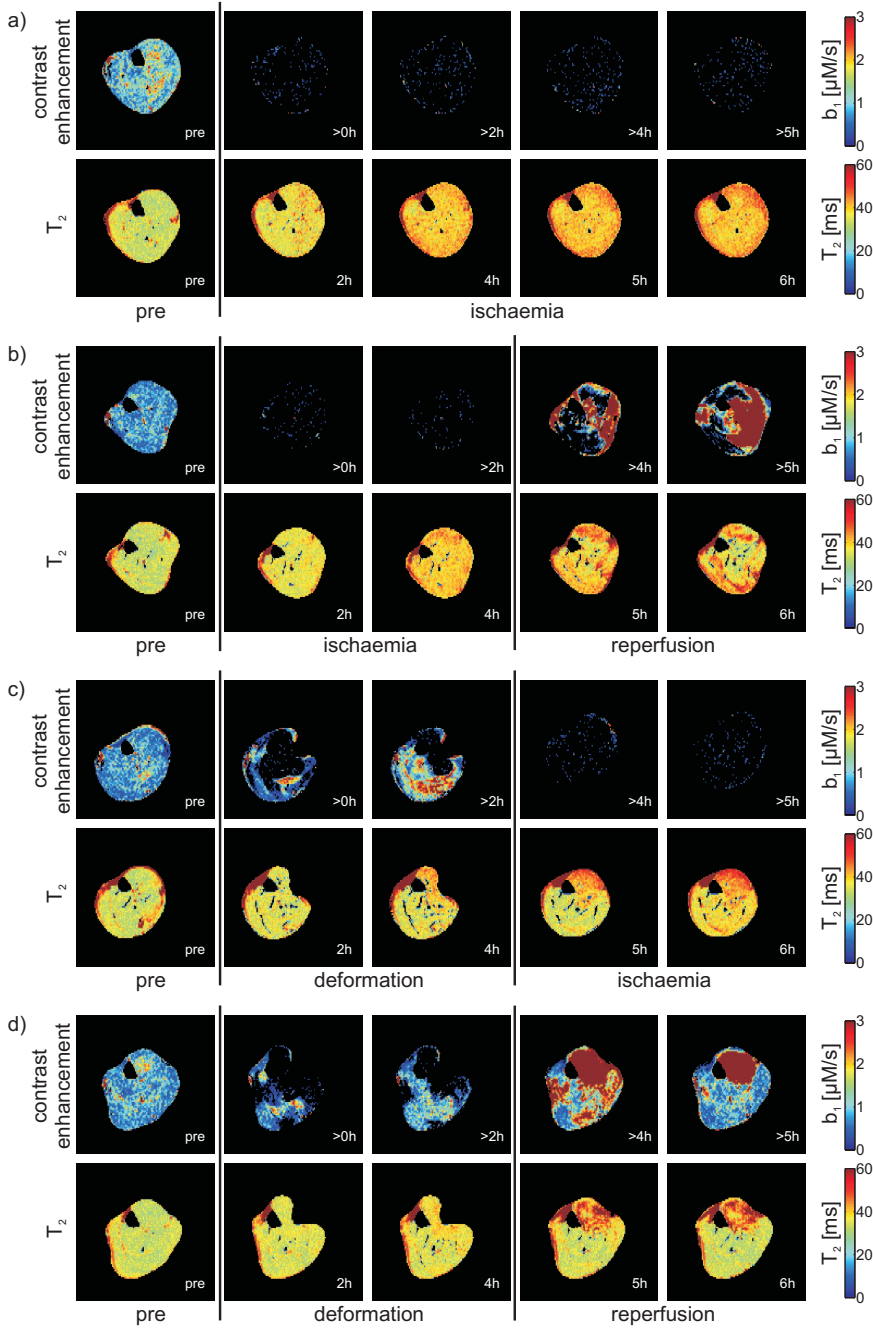
Figure 5.4: Spatial distributions of b_1 and T_2 in the rat leg in time for one experiment per experimental group: a) group I (6 h ischaemia); b) group II (4 h ischaemia followed by 2 h reperfusion); c) group III (4 h deformation followed by 2 h ischaemia); d) group IV (4 h deformation followed by 2 h reperfusion).

In figure 5.4, the b_1 and T_2 maps with time are shown for one animal of each experimental group. For all experiments, a homogeneous initial distribution of b_1 and T_2 was observed. For group I (figure 5.4a), the low values in the b_1 maps confirm the ischaemic condition during application of the vessel loop. The T_2 maps show a homogeneous increase in T_2 with time throughout the leg. For group II, similar results were observed during ischaemia (figure 5.4b). After removal of the vessel loop, heterogeneous b_1 and T_2 profiles were evident. There were areas in which contrast enhancement was absent, indicating no-reflow, which were associated with an increase in T_2. The locations of these distinct areas of no-reflow were similar across the experiments in group II. By contrast, a decrease in T_2 was observed in areas with reperfusion. The b_1 maps of group III indicate that part of the leg was ischaemic during deformation, and completely ischaemic when the vessel loop was subsequently applied (figure 5.4c). T_2 increased in the TA muscle region during deformation, and increased further in the complete leg during ischaemia. For group IV (figure 5.4d), similar results were observed during the deformation period as for group III. After deformation, however, the b_1 maps indicate that reperfusion occurred in the complete leg of this animal. Reperfusion also occurred for two other animals in this group, while for one animal no-reflow was observed in the complete TA muscle region. For two of these three animals with reperfusion, T_2 increased further in parts of the TA muscle region during the reperfusion phase.

The time course of T_2 for all individual experiments is shown in figure 5.5. In group I, the increase in T_2 in the leg was relatively similar for each animal (figure 5.5a). For group II, larger differences between animals were present after removal of the vessel loop (figure 5.5b). T_2 remained elevated or even increased in areas with no-reflow, whereas a decreasing trend in T_2 was observed for areas with reperfusion. Considerably more variation was observed between animals in groups III and IV (figure 5.5c-d). In group III, the overall increase in T_2 differed between animals, although the time profile was comparable. For animals in group IV, major differences were present after removal of the indenter. Reperfusion occurred in three of the four cases, accompanied by a variable increase in T_2. No-reflow in the complete TA muscle occurred in one animal (rat 4), associated with an elevated T_2 when compared to the situation during loading.

For each of the experiments involving deformation (groups III and IV), the mean 2D strain energy, percentage of ischaemia in the leg, and median T_2 in the TA muscle are presented in table 5.2. In addition to the variation in T_2 that was observed from figure 5.5d, also the levels of deformation and ischaemia appeared to vary across the experiments.
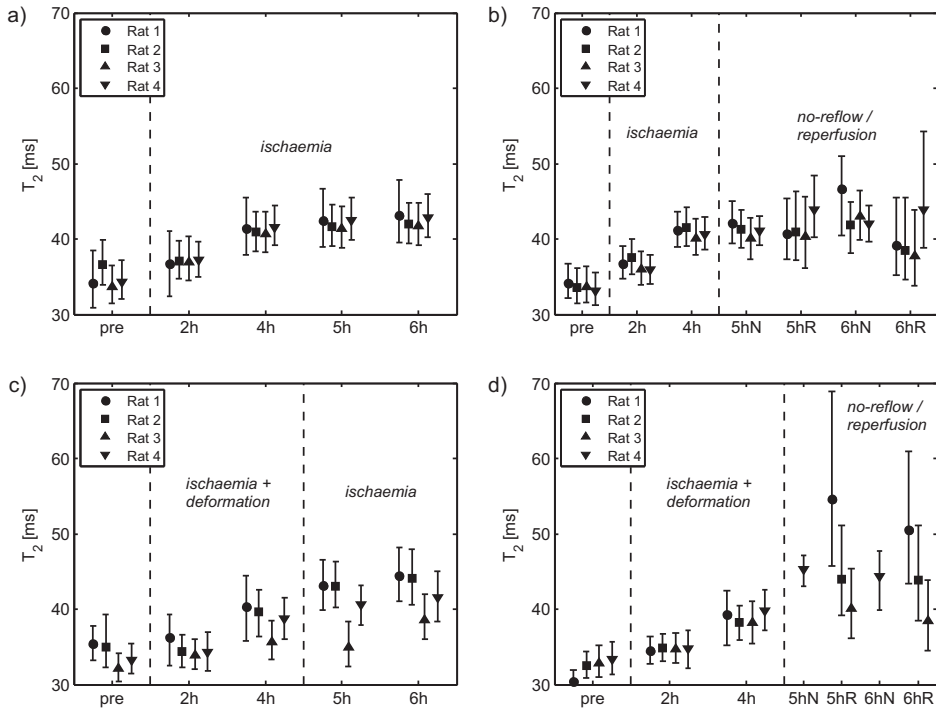
Figure 5.5: Median T_2 in time for the individual animals in each group. Error bars indicate the interquartile range of each T_2 distribution. a) Time course of T_2 in the leg in group I (6 h ischaemia). b) Time course of T_2 in the leg in group II. After removal of the vessel loop after 4 h ischaemia, the median T_2 was determined separately for areas with no-reflow (N) and with reperfusion (R). c) Time course of T_2 in the TA muscle in group III. During 4 h deformation, only the ischaemic region of the TA muscle was considered. d) Time course of T_2 in the TA muscle in group IV. During 4 h deformation, only the ischaemic region of the TA muscle was considered. After removal of the indenter, no-reflow (N) in the complete TA muscle region was observed for one animal (rat 4), while complete reperfusion (R) of the TA muscle was observed for the other three animals.

Table 5.2: Mean 2D strain energy, percentage of ischaemia in the leg, and median T_2 in the TA muscle in the experiments involving deformation (groups III and IV).

Animal	Mean 2D strain energy [$\times 10^{-4}$ J/mm]	Percentage ischaemia [%]	Median T_2 [ms]
Group III rat 1	1.29	50.8	44.5
Group III rat 2	1.23	66.7	44.0
Group III rat 3	0.78	32.7	38.6
Group III rat 4	1.47	80.4	41.5
Group IV rat 1	1.51	99.8	50.5
Group IV rat 2	1.39	55.5	43.9
Group IV rat 3	0.60	55.2	38.4
Group IV rat 4	1.29	91.6	44.0

For groups I and II, the mean group results were compared, where the significant differences in T_2 within and between these groups are presented in table 5.3. For both groups, no significant difference in T_2 was found between the initial distribution and after 2 h ischaemia. After 4 h ischaemia, T_2 was significantly increased in both groups when compared to the situation after 2 h ischaemia. In group I, T_2 did not significantly increase further after 4 h ischaemia. In the reperfused areas in group II, T_2 at the end of the 6 h investigation period was not significantly larger than after 2 h ischaemia, whereas T_2 in the no-reflow areas was still significantly elevated. Moreover, a significant difference in T_2 was found between the no-reflow and reperfused areas. No significant differences were found between groups I and II. Although there was a significant difference between T_2 in the no-reflow and reperfused areas at 6 h in group II, both distributions were not significantly different from T_2 after 6 h ischaemia in group I.

Table 5.3: Significant differences in T_2 in time within groups I and II and between both groups. Symbols N and R denote the areas with no-reflow (N) and reperfusion (R).

Comparison	Significant differences
Within group I	$T_{2,\mathrm{pre}} < T_{2,4\mathrm{h}}, T_{2,5\mathrm{h}}, T_{2,6\mathrm{h}}$
	$T_{2,2\mathrm{h}} < T_{2,4\mathrm{h}}, T_{2,5\mathrm{h}}, T_{2,6\mathrm{h}}$
Within group II	$T_{2,\mathrm{pre}} < T_{2,4\mathrm{h}}, T_{2,5\mathrm{hN}}, T_{2,5\mathrm{hR}}, T_{2,6\mathrm{hN}}, T_{2,6\mathrm{hR}}$
	$T_{2,2\mathrm{h}} < T_{2,4\mathrm{h}}, T_{2,5\mathrm{hN}}, T_{2,5\mathrm{hR}}, T_{2,6\mathrm{hN}}$
	$T_{2,6\mathrm{hN}} > T_{2,6\mathrm{hR}}$
Between groups I and II	-

In figure 5.6, comparisons between the appropriate experimental groups are shown. Due to the considerable variation between experiments in groups III and IV, the mean data of these groups were not used for comparison with other groups. In figure 5.6a, the individual results of group III are compared with the mean data of group I to investigate the relative effects of deformation and ischaemia. When compared to the effect of complete ischaemia (group I), it can be observed that deformation combined with partial ischaemia of the leg (group III) resulted in a slightly larger increase in T_2 in two animals (rats 1 and 2) and to a smaller increase in T_2 in the other two animals. The comparison of group II with the individual experiments of group IV shows that T_2 in the group IV experiments with reperfusion increased considerably in rats 1 and 2, whereas a decrease in T_2 was observed for the reperfused areas in group II (figure 5.6b). In the animal with no-reflow in the complete TA muscle region (rat 4), a considerable increase in T_2 was present after removal of the indenter.
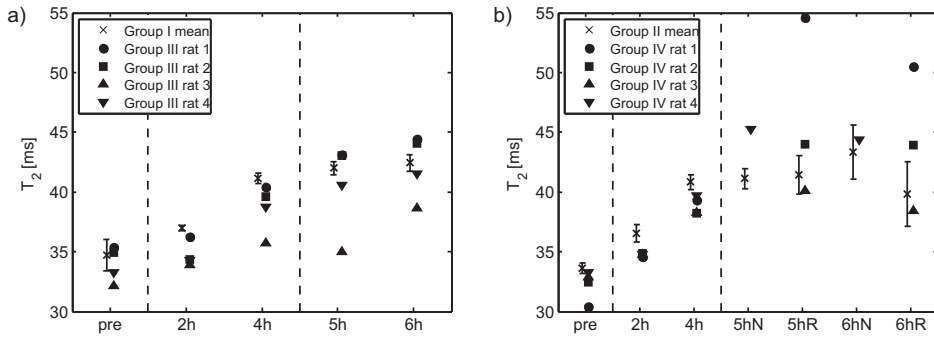
Figure 5.6: Comparison of T_2 profiles between the different experimental groups. a) Comparison of group I (mean $\pm$ standard deviation) with the individual experiments of group III (median T_2 in TA muscle). b) Comparison of group II (mean $\pm$ standard deviation) with the individual experiments of group IV (median T_2 in TA muscle). After removal of the vessel loop in group II, T_2 was determined separately for the no-reflow (N) and reperfused (R) areas. After removal of the indenter in group IV, complete no-reflow of the TA muscle was observed for one animal (rat 4), and complete reperfusion occurred in the other three animals.

Haematoxylin and eosin stainings of the TA muscles of both control and experimental legs are presented in figure 5.7. Cross-sections of the control leg showed a normal polygonal appearance of muscle fibres with few interstitial spaces (figure 5.7a). After 6 h ischaemia (group I), only minor alterations were observed, consisting of areas with somewhat larger cells and a little increase in interstitial spaces (figure 5.7b). In group II, more severe histological changes were observed after 4 h ischaemia and 2 h reperfusion, although there were regional differences in the severity of these changes (figure 5.7c-d). In some regions, only minor alterations were present, whereas in other areas rounded hypertrophic fibres and considerably increased interstitial spaces were evident. In the deformation experiments (groups III and IV), also regions with enlarged fibres and severely increased interstitial spaces were observed adjacent to areas with minor changes in the tissue (figure 5.7e-h).
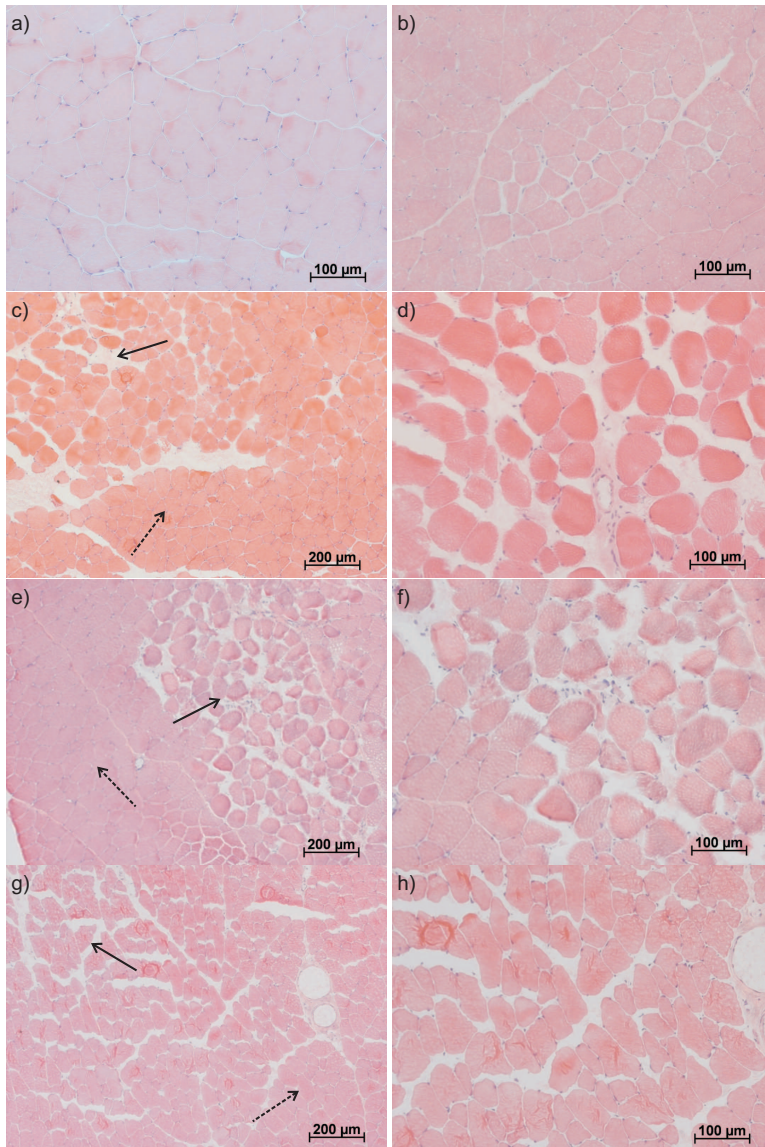
Figure 5.7: Haematoxylin and eosin stainings of cross-sections of the TA muscle. a) Tissue from the control leg, showing a normal polygonal appearance of muscle fibres and small interstitial spaces. b) In group I, only minor alterations in the tissue were present. c) In group II, remarkable regional differences were observed, where tissue changes were only minor in some areas (dashed arrow), and more severe in others (solid arrow). d) Close-up of a region with severe swelling in group II (same magnification as control leg). e) In group III, severe swelling was observed in some areas (solid arrows), whereas only minor alterations were present in others (dashed arrows). f) Close-up of a region with considerable swelling in group III (same magnification as control leg). g) In group IV, also areas with enlarged fibres and increased interstitial spaces were present (solid arrow) adjacent to areas with minor alterations (dashed arrow). h) Close-up of a a region with swelling in group IV (same magnification as control leg).

5.4   Discussion

In the present study, the effects of deformation, ischaemia, and reperfusion on muscle damage development were investigated. This involved the use of a previously developed rat model for DTI, with the animals subjected to different combinations of deformation, ischaemia, and reperfusion during a 6 h period (figure 5.2a). Perfusion was examined using DCE-MRI, and tissue integrity was monitored with T_2-weighted MRI. Local tissue deformations were estimated using animal-specific FE models. Complete ischaemia of the leg caused a homogeneous increase in T_2 in the leg (group I). Reperfusion after 4 h ischaemia was absent in distinct areas, associated with larger T_2 values when compared to T_2 in reperfused areas (group II). T_2 increased in large parts of the TA muscle in all experiments involving deformation (groups III and IV), although large variations were observed between the individual experiments.

Local perfusion in the rat leg was examined using an intravenous bolus injection of contrast agent. A local perfusion index was derived from the initial slope of the local time profile of the contrast agent concentration. Although the initial slope of the signal intensity or concentration curve is often used to study changes in local perfusion (Al-Saadi et al., 2000; Luo et al., 2002; Jerosch-Herold et al., 2004), this parameter also reflects the permeability of the blood vessels, and is consequently not a direct measure of perfusion alone. In the present study, however, it was still considered a suitable measure to distinguish between regions with and without perfusion, since complete absence of contrast enhancement can only be caused by a lack of perfusion. Changes in tissue integrity were monitored with T_2-weighted MRI, where an increase in T_2 was considered a measure of tissue damage involving oedema, necrosis, or inflammation (Fleckenstein, 1996). Biopsies of the TA muscle were taken at the end of the 6 h investigation period to distinguish between the different pathological processes.

Local deformations in the TA muscle during indentation were estimated using FE models in which the geometry and boundary conditions were adapted for each experiment. The original FE model was developed by Ceelen et al. (2008a) and validated with MR-tagging experiments. The applied strains in this animal model have previously been reported by Ceelen et al. (2008b), revealing compressive strains up to ∼50 % and maximum shear strains up to ∼100 %. These strains are similar to those in the buttocks of seated individuals. Indeed, an estimation of the internal strains during sitting by Linder-Ganz et al. (2008) revealed compressive strains up to ∼80 % and maximum shear strains up to ∼100 %, particularly in spinal cord injured subjects. The model was further improved by Loerakker et al. (2010), and showed good correspondence with the contours of the deformed leg in the MR images. The muscle tissue in the leg was modelled with a hyperelastic Ogden law using material properties partly based on experiments by Bosboom et al. (2001). Consequently, the strain energy values calculated from the simulations

should not be interpreted as absolute values, but rather as a relative measure of the level of deformation to compare experiments.

In group II, reperfusion was noticeably absent in specific regions of the leg, where T_2 remained elevated or even increased further after removal of the vessel loop (figure 5.5b). No-reflow is a feature of I-R injury that can be caused by microvascular thrombosis, vasospasm, or oedema (Urbaniak et al., 1997; Blaisdell, 2002). The two major regions of no-reflow were located in the anterior tibial and superficial posterior compartments of the leg, corresponding with the results of Morikawa et al. (1991), who performed similar experiments with ischaemia and reperfusion in the rat hindlimb. The locations of no-reflow in the present study may be due to either the occurrence of acute compartment syndrome or by the specific architecture of blood vessels in the rat hindlimb (Loerakker et al., 2011).

Only minor histological alterations were evident in group I animals after 6 h ischaemia. Therefore, the T_2 increase in this group may not be indicative of sustained structural damage, but was more likely related to the intracellular metabolic changes and cell swelling that are both associated with ischaemia. There were discrete regions of more severe swelling in parts of the TA muscle in group II, presumably coincident with the no-reflow areas that exhibited a further increase in T_2. Similar morphological features involving oedema were observed after ischaemia and reperfusion in previous studies (Carmo-Araújo et al., 2007; Hashimoto et al., 2008). Hatoko et al. (2002) also reported that interstitial oedema after 6 h ischaemia occurred gradually with reperfusion, which might explain the minor alterations in group I observed in the present study. Thus, ischaemia alone caused only minor changes in the muscle tissue in group I that could probably be reversed by reperfusion after 4 h of ischaemia in group II. However, tissue swelling could also be aggravated in group II in areas with no-reflow, indicating the complex effect of reperfusion on damage development in skeletal muscle. In addition, this swelling of the tissue may lead to a substantial increase in muscle stiffness, which will increase the load on the adjacent healthy tissue and can thereby contribute to the progression of tissue damage (Gefen et al., 2005). Whether the effect of reperfusion is beneficial or not depends not only on the duration of ischaemia, but also on the anatomical location of the insult, and the rate of the load removal (Ünal et al., 2001).

The overall increase in T_2 with time varied between the animals in group III. For example, when compared to the results after 6 h ischaemia in group I, the total T_2 increase in group III was slightly larger in two animals and smaller in two other animals (figure 5.6a). These results indicate that deformation in combination with partial ischaemia of the leg can lead to a smaller T_2 increase in the TA muscle as a whole than complete ischaemia of the leg. Locally, however, deformation in combination with partial ischaemia can still be more damaging than complete ischaemia (figure 5.7e-f). In group IV, com-

plete reperfusion of the TA muscle was observed for three of the four animals. During the reperfusion phase, T_2 remained comparable to the situation after 4 h deformation in one animal, and increased considerably further in large parts of the TA muscle in the other two animals (figure 5.6b), this latter increase being considerably larger than in the group II experiments. A possible explanation for these results is that the deformation in these two experiments may have caused substantial structural damage in the muscle, which is manifested in the reperfusion phase by increased swelling in the tissue, or even aggravation of tissue damage.

Stekelenburg et al. (2007) showed that 2 h deformation, inevitably combined with partial ischaemia, caused highly localised regions of irreversible muscle damage, whereas 2 h of complete ischaemia only caused reversible changes in the tissue. The locations of tissue damage clearly coincided with the areas subjected to the highest deformations (Ceelen et al., 2008b; Loerakker et al., 2010). For loading periods up to 2 h, these results imply that ischaemia has a negligible effect on muscle damage development and deformation is the primary trigger for muscle damage. In the extended experiments of the present study involving deformation, T_2 increased in a large part of the TA muscle, and not only in a narrow region as observed after 2 h deformation. Therefore, ischaemia is probably responsible for part of the T_2 increase, indicating that deformation and ischaemia are both involved in the damage process. In addition, a larger variation was observed between the experiments in which deformation was applied and those not involving deformation. This could be attributed to the significant variation in deformation between experiments as reflected in the broad range of values for the mean 2D strain energies (table 5.2) in both groups III and IV. This can be expected to cause a variation in size of the area with T_2 increase caused by deformation (figure 5.1) (Loerakker et al., 2010). On the other hand, the percentage of ischaemia in the leg also varied between experiments (table 5.2), implying that ischaemia could have had a variable influence on the increase in T_2 in the different experiments as well. Therefore, deformation may have both a direct and an indirect effect on the damage process. The consequence of the former is that a larger overall deformation causes a larger area of T_2 increase (Loerakker et al., 2010). The indirect effect arises from the fact that deformation partly determines the level of ischaemia in the leg, and thereby would subsequently influence the increase in T_2.

Due to the large variation between the experiments involving deformation and partial ischaemia, it is difficult to definitively prove this hypothesis. However, since the applied levels of deformation and ischaemia will always be different in every experiment due to differences in leg geometry and load application, increasing the number of experiments would not reduce this variation in the deformation groups. To obtain more insight into the quantitative contributions of deformation and ischaemia, the experiments could be classified into specific subgroups of deformation, ischaemia, and reperfusion. However, due to the large variation between experiments, the complex effect of reperfusion, and

the fact that there are probably interactions between the effects of deformation and ischaemia, this approach will require a very large number of animals before significant differences between subgroups can be found. Furthermore, the large variation in T_2 increase due to differences in load application and geometry between animals is also an important observation, as it may explain in part the differences in susceptibility to DTI development between different tissue sites on the same individual.
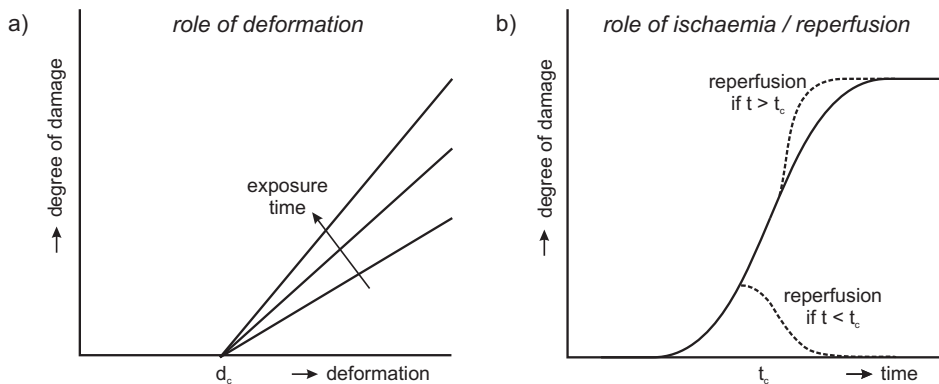
Figure 5.8: Hypothesis for the development of DTI. a) Deformation directly causes muscle damage if a critical deformation threshold (d_c) is exceeded. The amount of damage is determined by the exposure time. b) For long periods, ischaemia and reperfusion become involved in the damage process. Reperfusion can reverse the damage process after a short ischaemic period. However, if a critical time point t_c is exceeded, reperfusion will aggravate tissue damage. When the loading period increases, it is expected that ischaemia will ultimately play a more important role in the damage process than deformation.

Based on the results of the present paper and previous studies, an hypothesis for the development of DTI can be proposed (figure 5.8). Deformations exceeding a specific threshold will directly cause muscle damage, where the degree of damage will be determined by the level of deformation and its exposure time (figure 5.8a). As the loading period increases, ischaemia and reperfusion will also contribute to the damage process. Reperfusion will be beneficial for the tissue only for a limited period of ischaemia. When this period is exceeded, reperfusion will aggravate existing tissue damage (figure 5.8b). The time point after which reperfusion causes additional damage depends on several factors, including the anatomical location and temperature of the involved tissue. Thus, for prolonged loading, deformations exceeding a threshold directly cause muscle damage that is subsequently aggravated by ischaemia and reperfusion with increasing exposure time. The level of ischaemia and thereby its damaging effect, is partly influenced by the level of deformation. Ischaemia and subsequent reperfusion may ultimately contribute more to muscle damage development than deformation, as their damaging effects significantly increase with the exposure time. In summary, the damage process in skeletal

muscle tissue is dominated by the level of deformation during short loading periods, corresponding to the initial plateau phase in the sigmoid pressure-time threshold for muscle damage as proposed recently (Linder-Ganz et al., 2006; Gefen et al., 2008; Stekelenburg et al., 2008; Gefen, 2009). However, during prolonged loading, ischaemia and reperfusion will gradually take over, and ultimately play a more important role than deformation.

For clinical practice, this hypothesis would imply that the rapid initiation and subsequent progression of DTI can be prevented by using appropriate cushioning in order to keep internal tissue deformations below the deformation threshold for damage. For prolonged loading, it is indeed important to limit the period of ischaemia by means of repositioning strategies and pressure-relieving mattresses, to prevent tissue damage related to ischaemia or I-R injury. The deformation threshold for damage as well as the time point after which ischaemia starts to cause tissue damage will inevitably vary between individuals and also for a specific individual in time. These variations are probably related to pathologies, especially those related to spinal cord injury, that influence tissue properties (Elsner and Gefen, 2008; Linder-Ganz et al., 2008), the circulation, and the immune system. These factors will partly explain the individual susceptibility to the development of DTI and highlight the need for regular assessments of individual subjects.

Acknowledgements

Chapter 6

How does muscle stiffness affect the internal deformations within the soft tissue layers of the buttocks under constant loading?

6.1   Introduction

A pressure ulcer is a localised injury to the skin and/or underlying tissue, usually over a bony prominence, as a result of pressure, or pressure in combination with shear (NPUAP and EPUAP, 2009). Pressure ulcers can occur in situations where people are subjected to sustained mechanical loads, and are particularly common in subjects who are bedridden or wheelchair-bound. The occurrence of pressure ulcers is a major secondary complication for spinal cord injured (SCI) individuals (McKinley et al., 1999; Garber and Rintala, 2003). In addition, a large proportion of ulcers in this population are severe involving deep tissues (Garber and Rintala, 2003), and are associated with poor healing and a high recurrence rate (Rintala et al., 2008; Bates-Jensen et al., 2009).

Pressure ulcers can originate at the skin surface and progress toward deeper tissues, but they can also start in deep tissues underneath an intact skin and progress outward. In several studies, tissue damage due to compression was observed initially in the muscle tissue as opposed to skin (Nola and Vistnes, 1980; Daniel et al., 1981; Salcido et al., 1994). This type of injury has recently been defined as pressure-related deep tissue injury (DTI) (Ankrom et al., 2005; Black et al., 2007). The reported prevalence of DTI is relatively low when compared to other pressure ulcer categories, although its value may be underestimated due to difficulties in identifying DTI (Kottner et al., 2010; VanGilder et al., 2010). Nevertheless, it represents a severe problem, because tissue damage observed at the skin surface only becomes apparent at an advanced stage, at which time treatment becomes problematic with a variable prognosis (Thomas, 2001; Brem et al., 2010). Therefore, early identification and subsequent treatment of DTI are critical to reduce comorbidities and costs. This requires an improved understanding of its underlying aetiology, if appropriate risk assessment tools and early detection methods are to be developed.

The aetiology of DTI is multifactorial in nature, involving compression-induced ischaemia (Kosiak, 1959; Daniel et al., 1981), ischaemia-reperfusion injury (Peirce et al., 2000; Tsuji et al., 2005), impaired lymphatic drainage (Miller and Seale, 1981), and tissue deformation (Bouten et al., 2003; Breuls et al., 2003; Linder-Ganz et al., 2007; Gefen et al., 2008). For short loading periods, tissue deformation was reported to be the most important factor in skeletal muscle damage development (Gawlitta et al., 2007a; Stekelenburg et al., 2007). Moreover, in a rat model for DTI, muscle damage only occurred if a specific deformation threshold was exceeded (Ceelen et al., 2008b; Loerakker et al., 2010). It is likely that this deformation threshold is within the physiological range of deformations that occur in the buttocks of seated individuals, particularly in the SCI population (Linder-Ganz et al., 2007, 2008). Therefore, it is essential to minimise internal tissue deformations during sitting to prevent the short-term development of muscle damage that may eventually lead to ulcer formation.

Developed models have predicted that the internal strain distribution in soft tissues in the buttocks during sitting is highly heterogeneous, with larger strains evident underneath bony prominences compared to locations adjacent to the body-support interface (Chow and Odell, 1978; Dabnichki et al., 1994; Oomens et al., 2003). The magnitude and distribution of internal strains are determined by the body weight, the support surface, and the thickness and mechanical properties of the tissues. SCI is associated with a range of events that alter the distribution of internal strains. One of these features is muscle atrophy as a result of disuse (Scelsi, 2001; Liu et al., 2008). Additionally, the properties of the muscle tissue change, leading to an increase in lipid content and a decrease in muscle tone (Scelsi, 2001), which can lead to a decrease in muscle stiffness. Accordingly, a decrease in both thickness and stiffness of muscles resulting from SCI will be associated with increased deformations during loading and hence an increased risk of DTI. Indeed, a recent study reported that a decrease in muscle thickness caused an increase in strains in the muscle tissue (Elsner and Gefen, 2008). In a separate study, the presence of intramuscular fat infiltration was reported to increase internal deformations in the muscle as well (Sopher et al., 2011).

Electrical stimulation of muscles has long been proposed as a strategy to prevent these structural alterations following SCI. The modality is designed to preserve or increase muscle thickness, and enhance oxygenation of muscle tissues. If applied during loading, stimulation-induced muscle contractions were reported to increase muscle stiffness and reconfigure the shape of the muscle (Levine et al., 1990a). In several studies, reduced interface pressures under the ischial tuberosities and increased tissue oxygenation levels due to stimulation were reported for able-bodied and SCI subjects (Levine et al., 1990b; Bogie et al., 2006; Van Londen et al., 2008; Gyawali et al., 2011; Solis et al., 2011a). In addition, intermittent electrical stimulation has been used to prevent or reduce the development of muscle damage during 2 h loading in animal models of DTI (Solis et al., 2007; Curtis et al., 2011). In this way, electrical stimulation can have a long-term effect by improving tissue properties, and also a short-term effect by preventing the development of muscle damage.

Recently, an animal model was developed to investigate the effect of electrical stimulation on the internal pressures and deformations in the buttocks during loading (Solis et al., 2011b,c). The geometry of the buttocks before and during loading, either with or without stimulation, was assessed using magnetic resonance imaging (MRI). The local deformations in the tissues during loading were assessed with MR tagging. However, this method was limited for a number of reasons. For example, MR tagging could not be applied during stimulation because of the large displacements in the muscle during contraction. Furthermore, MR tagging was unable to distinguish between the internal strains in the different tissue layers due to its limited spatial resolution. In the present study, an animal-specific finite element (FE) model was developed to simulate the inter-

nal tissue deformations during loading in the muscle, fat, and skin layer. The following questions were addressed:

1. How large are the deformations in the three soft tissue layers during loading?

2. How sensitive is the FE model to the relative stiffnesses of the three tissues?

3. What is the effect of a change in muscle stiffness on the internal deformations?

4. What is the contribution of increased muscle stiffness to the changes in deformation during electrical stimulation?

6.2   Materials & Methods

6.2.1   Animal model

The internal loading conditions were investigated in a porcine model for DTI (Solis et al., 2011b,c), as illustrated in figure 6.1. All experimental protocols were approved by the University of Alberta Animal Care and Use Committee. In the present study, the FE model was developed to simulate the experimental conditions in one animal (Yucatan Miniature Swine, 2 years old, 73 kg). Prior to loading, the animal was positioned in prone position inside a 1.5 T MR scanner (Siemens Sonata system) and fixated to the support surface. The initial undeformed geometry of the buttocks was assessed using MRI (TE = 2.33 ms, TR = 4.92 ms, slice thickness = 2.5 mm, FOV = $400 \times 400 \times 260$ mm^3, matrix size = $640 \times 640 \times 104$). Subsequently, the buttocks of the animal were loaded with an MR-compatible indenter on which a force of 25 % of the body weight was imposed. The geometry of the tissues during loading was determined with MRI (TE = 1.09 ms, TR = 2.45 ms, slice thickness = 3.5 mm, FOV = $333 \times 400 \times 154$ mm^3, matrix size = $320 \times 384 \times 44$). Electrical stimulation was then applied for a period of 10 s while the constant load was maintained. This involved the placement of MR-compatible skin electrodes over the motor points of the gluteal muscles of the left hindlimb to generate maximal contractions. One second after the start of stimulation, MRI (same parameters as during loading without stimulation) was used to investigate the change in geometry due to stimulation.
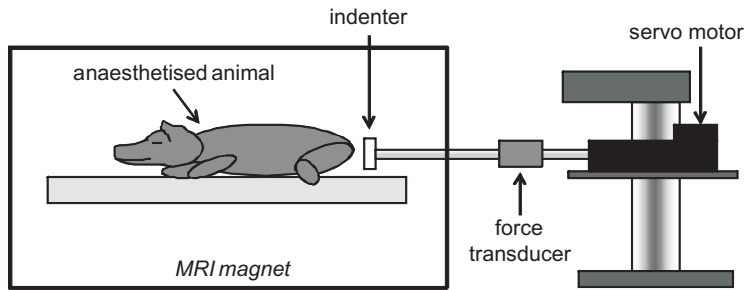
Figure 6.1: Schematic overview of the experimental setup. The animal was positioned in prone position within the MRI system. A force of 25 % of the body weight of the animal was imposed on an MR-compatible indenter to compress the buttocks. The geometry of the buttocks before and during loading was monitored with MRI. (Adapted from Solis et al. (2011b,c).)

6.2.2   FE model

The high-resolution MR images of the buttocks before loading were imported into the software package Mimics (Materialise NV, Leuven, Belgium) for segmentation of the different tissues and to create a 2D mesh of ∼8000 quadratic triangular elements (figure 6.2).
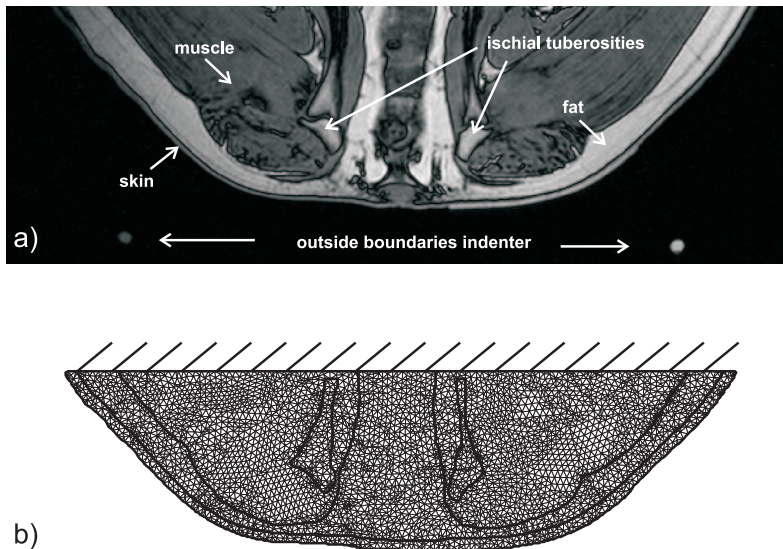
Figure 6.2: a) High-resolution MR image of the buttocks before loading that was used for segmentation of the different tissues. b) Resulting mesh of the FE model. Zero-displacement boundary conditions were imposed on the bones and the top of the mesh.

The bones were considered rigid, and muscle, fat, and skin were modelled as incompressible single-mode Ogden materials with strain energy density W:

$$W = \frac{\mu}{\alpha}(\lambda_1^\alpha + \lambda_2^\alpha + \lambda_3^\alpha - 3) \tag{6.1}$$

where $\lambda_i (i = 1, 2, 3)$ are the principal stretch ratios, and μ and α are material parameters. In the present study, $\alpha = 5$ was assumed for all soft tissues. Parameter μ for each tissue was derived from the corresponding shear modulus G according to (Ogden, 1972; Ogden et al., 2004):

$$\mu = \frac{2G}{\alpha} \tag{6.2}$$

The shear modulus of muscle was derived from MR elastography data of human subjects (Kruse et al., 2000; Basford et al., 2002). For fat, the shear modulus of porcine tissue was used (Geerligs et al., 2008). Data of human skin that were fitted to a computational model were used to determine the Young's modulus and subsequently, by assuming incompressibility, the shear modulus of skin (Hendriks et al., 2003). The shear moduli and the parameters of the Ogden model for each tissue are shown in table 6.1.

Table 6.1: Shear modulus G of muscle (Kruse et al., 2000; Basford et al., 2002), fat (Geerligs et al., 2008), and skin (Hendriks et al., 2003), and the parameters α and μ of the Ogden model for each of the tissues included in the FE model.

Tissue	G [kPa]	α [-]	μ [kPa]
Muscle	15	5	6
Fat	7.5	5	3
Skin	20	5	8

In all simulations, zero-displacement boundary conditions were applied to the bones and the top of the mesh (figure 6.2b). Furthermore, a plane stress situation was assumed. The indenter in the FE model was modelled as a rigid body with a prescribed displacement. This displacement was derived from the final position of the indenter in the MR image of the buttocks during loading without stimulation.

The deformation gradient tensor $\boldsymbol{F}$ was calculated from the nodal displacements and used to calculate the Green-Lagrange strain tensor $\boldsymbol{E}$. From this, the in-plane principal strains E_1 and E_2 (with $E_1 > E_2$) and maximum shear strain $\gamma_{max} = \frac{1}{2}(E_1 - E_2)$ were

determined. The maximum shear strain was calculated since a correlation between this strain parameter and the presence of muscle damage has recently been reported (Ceelen et al., 2008b). The principal stresses σ_i ($i = 1, 2, 3$) were calculated using the following relation(Ogden et al., 2004):

$$\sigma_i = \lambda_i \frac{\partial W}{\partial \lambda_i} - p = \mu \lambda_i^\alpha - p \tag{6.3}$$

Since the out-of-plane principal stress σ_3 is equal to zero in the plane stress simulations, the hydrostatic pressure p is equal to $\mu \lambda_3^\alpha$. The principal stretch ratios were derived from the principal Green-Lagrange strains and the incompressibility assumption:

$$\lambda_{1,2} = \sqrt{2E_{1,2} + 1} \qquad \text{and} \qquad \lambda_3 = \frac{1}{\lambda_1 \lambda_2} \tag{6.4}$$

Subsequently, the in-plane maximum shear stress $\tau_{max} = \frac{1}{2}(\sigma_1 - \sigma_2)$ was calculated from the in-plane principal stresses (with $\sigma_1 > \sigma_2$).

6.2.3 Sensitivity analysis

To investigate the influence of the stiffness of the three tissues in the model on the calculated deformations, parameter μ in each tissue was varied by 50 % from the prescribed values (table 6.1), according to a Taguchi orthogonal array (table 6.2, (Logothetis and Wynn, 1989)). For each simulation, the largest values of γ_{max} and τ_{max} in each tissue were calculated to assess the influence of the relative stiffnesses on the deformations in each tissue.

Table 6.2: Taguchi orthogonal array consisting of nine simulations to assess the influence of the relative stiffnesses of muscle (μ_m), fat (μ_f), and skin (μ_s) on the strain distribution in the FE model. The value of μ was varied by 50 % from the reference value (table 6.1) for each tissue.

Simulation	μ_m [kPa]	μ_f [kPa]	μ_s [kPa]
1	3	1.5	4
2	3	3	8
3	3	4.5	12
4	6	1.5	8
5	6	3	12
6	6	4.5	4
7	9	1.5	12
8	9	3	4
9	9	4.5	8

6.2.4   Effects of a change in muscle stiffness

The effects of a change in muscle stiffness, e.g. a decrease after SCI or an increase during electrical stimulation, was investigated by varying the value of μ for the muscle by 25 and 50 %. For these simulations, it was assumed that the body weight of an individual would not change. Therefore, the displacement of the indenter was imposed incrementally until the same force of 25 % body weight was achieved as in the reference simulation. Thus, the displacement of the indenter was not equal in the different simulations. The largest values of γ_{max} and τ_{max} in each tissue were calculated to determine the influence of a change in muscle stiffness on the deformations of the individual tissues.

Since only the left hindlimb of the animal was stimulated in the experiment, additional simulations were performed in which the muscle stiffness in the FE model was increased only on one side of the buttocks. Again, the indenter displacement was imposed incrementally until the same force was achieved as in the reference simulation. These simulations with 25 and 50 % increased muscle stiffness on one side of the buttocks were compared with MR images of the buttocks during loading and stimulation, to investigate the contribution of increased muscle stiffness to the changes in deformation that occur during stimulation.

6.3   Results

6.3.1   Reference model

In figure 6.3, the results of the reference model are shown. The contours of the mesh during loading show a good agreement with the experimental observations (figure 6.3b). High strains are present in both the muscle and the fat layers (figure 6.3c). Indeed, the largest values of γ_{max} are similar (0.65 for muscle and 0.63 for fat), but the high-strain area is considerably larger in the fat tissue. By contrast, figure 6.3d demonstrates that the muscle layer is exposed to the largest shear stresses in the buttocks, with a maximum of 36 kPa. The largest principal strains and stresses in each tissue are shown in table 6.3.
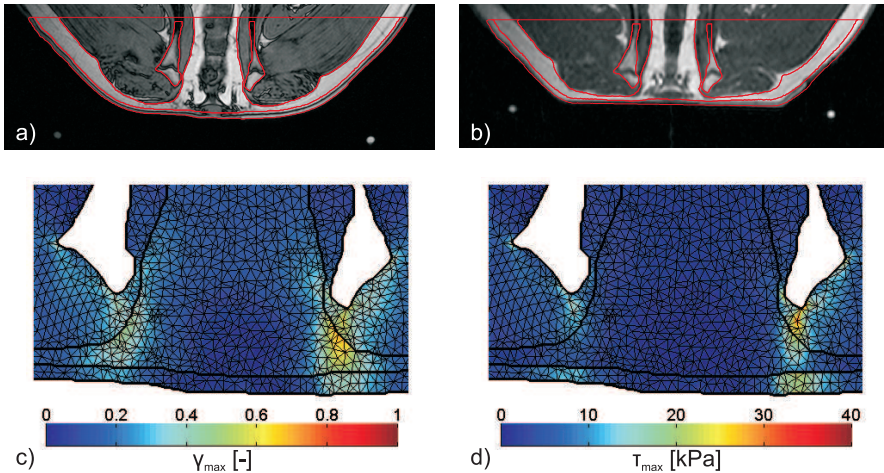
Figure 6.3: a) MR image of the pig buttocks with the mesh contours (red) before loading. b) MR image of the pig buttocks with the mesh contours (red) during loading with 25 % body weight. c) Distribution of γ_{max} in the buttocks during loading. d) Distribution of τ_{max} in the buttocks during loading.

Table 6.3: Largest principal strains (E_1 and E_2 with $E_1 > E_2$) and stresses (σ_1 and σ_2 with $\sigma_1 > \sigma_2$) in each tissue in the reference model.

	E_1 [-]	E_2 [-]	γ_{max} [-]	σ_1 [kPa]	σ_2 [kPa]	τ_{max} [kPa]
Muscle	0.86	-0.43	0.65	24	-79	36
Fat	0.83	-0.43	0.63	3	-32	17
Skin	0.46	-0.35	0.41	7	-34	20

6.3.2   Sensitivity analysis

To assess the effect of each tissue stiffness on the deformed mesh, the contours of the three simulations with the same tissue stiffness were averaged, resulting in three average mesh contours per tissue (figure 6.4). The muscle stiffness had the largest influence on the deformed mesh contours (figure 6.4a). The stiffness of the fat and skin layer only had a minimal effect on the resulting mesh contours (figure 6.4b-c).
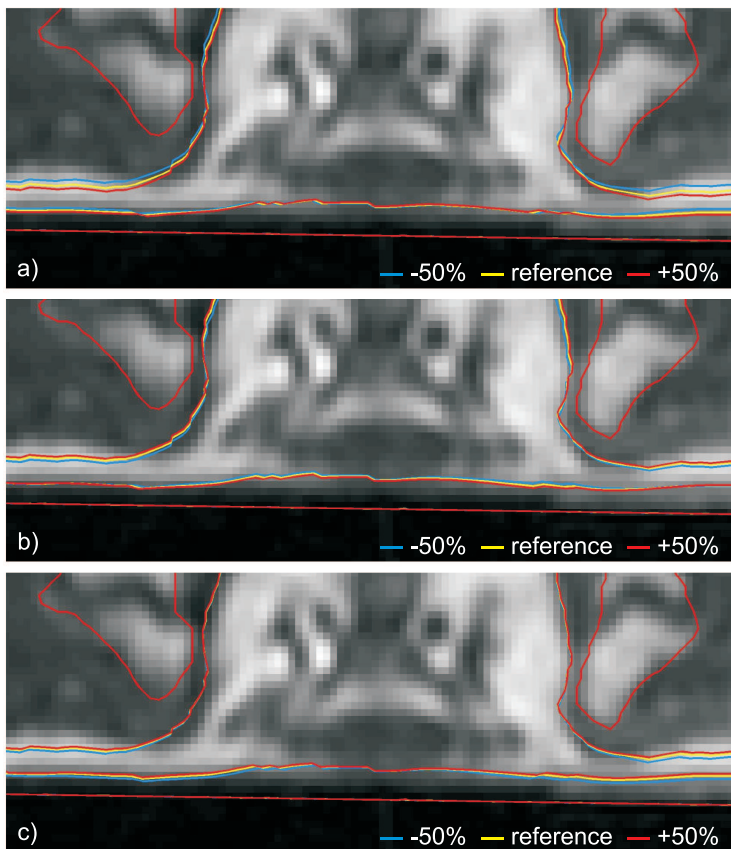
Figure 6.4: Average contours of the simulations of the sensitivity analysis. a) Average contours of the simulations with the reference muscle stiffness (simulations 4-6), and with a 50 % decrease (simulations 1-3) or increase (simulations 7-9). b) Average contours of the simulations with the reference fat stiffness (simulations 2,5,8), and with a 50 % decrease (simulations 1,4,7) or increase (simulations 3,6,9). c) Average contours of the simulations with the reference skin stiffness (simulations 2,4,9), and with a 50 % decrease (simulations 1,6,8) or increase (simulations 3,5,7).

The largest values of γ_{max} and τ_{max} in each tissue for all nine simulations are shown in figure 6.5. The relative stiffness values of the three soft tissues in the buttocks have a large influence on the internal distribution of γ_{max} (figure 6.5a). The largest value of γ_{max} in each tissue is smallest in the skin layer for all simulations. The largest strains in the muscle and fat layer are comparable if μ_m is twice as large as μ_f (simulations 1, 5, and 9, table 6.2). The largest strain is larger in muscle than in fat if $\mu_m < 2\mu_f$ (simulations 2, 3, and 6). On the other hand, the largest strains in the buttocks are present in the fat layer if $\mu_m > 2\mu_f$ (simulations 4, 7, and 8). For the distribution of τ_{max}, the relative stiffness values of the different tissues mainly influence the magnitude of τ_{max} in the tissues, with considerably less influence on the relative stresses in the different tissues. The largest stresses are in the muscle layer, whereas the largest τ_{max} in the skin is slightly larger than the largest τ_{max} in the fat layer in seven out of nine simulations (figure 6.5b).
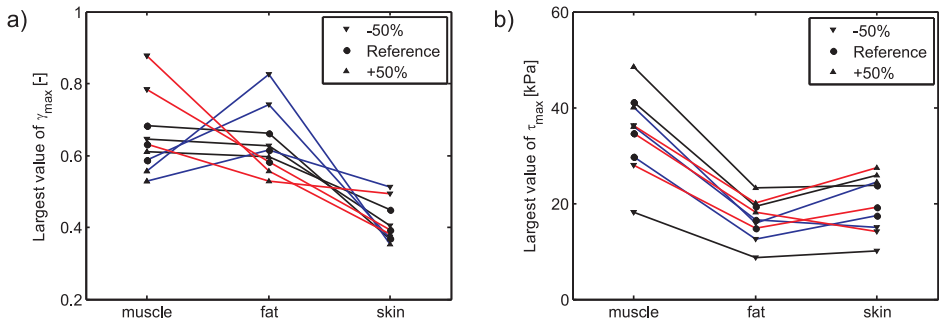
Figure 6.5: Largest maximum shear strain (γ_{max}) (a) and maximum shear stress (τ_{max}) (b) in each tissue for the nine simulations of the sensitivity analysis. Black lines: results of simulations 1, 5, and 9 ($\mu_m = 2\mu_f$); blue lines: results of simulations 4, 7, and 8 ($\mu_m > 2\mu_f$); red lines: results of simulations 2, 3, and 6 ($\mu_m < 2\mu_f$). The symbol ● indicates that the reference value was chosen for the tissue, and the symbols ▼ and ▲ indicate that the reference value decreased or increased by 50 %, respectively.

6.3.3   Effects of a change in muscle stiffness

Figure 6.6 shows the distribution of γ_{max} and τ_{max} in the buttocks in the simulations in which the muscle stiffness was increased and decreased by 50 %. The reaction force on the indenter was equal in these simulations. A 50 % decrease in muscle stiffness caused an increase in strains in the buttocks (figure 6.6a), which was primarily evident in the muscle tissue, accompanied by an increase in stress (figure 6.6b). A 50 % increase in muscle stiffness caused a reduction in both internal shear strains and stresses (figure 6.6c-d), particularly marked in the muscle layer.
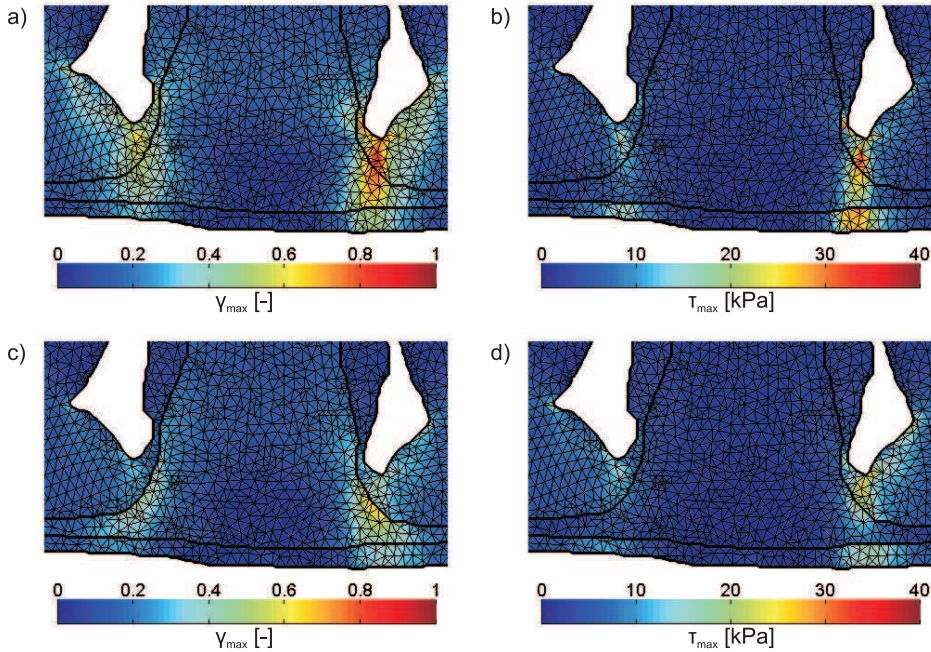
Figure 6.6: Distribution of the maximum shear strain (γ_{max}) (a) and maximum shear stress (τ_{max}) (b) in the simulation in which the muscle stiffness was reduced by 50 %. Distribution of γ_{max} (c) and τ_{max} (d) in the simulation in which the muscle stiffness was increased by 50 %. (For comparison, figures 6.3c and 6.3d show the distribution of γ_{max} and τ_{max} in the reference simulation.)

The largest strain in the muscle changes considerably with variation in muscle stiffness (figure 6.7a). Indeed, a decrease of 50 % in stiffness causes an increase in maximum shear strain from 0.65 to 0.99 in the muscle. The corresponding strains in the fat and skin layer are less affected by the change in muscle stiffness. By contrast, a 50 % increase in muscle stiffness causes a decrease in strain from 0.65 to 0.49. In this way, the largest strain in the muscle tissue decreases to a value below the largest strain in the fat layer. The corresponding trends in internal stress with changes in muscle stiffness are fairly similar for each of the three tissues (figure 6.7b).
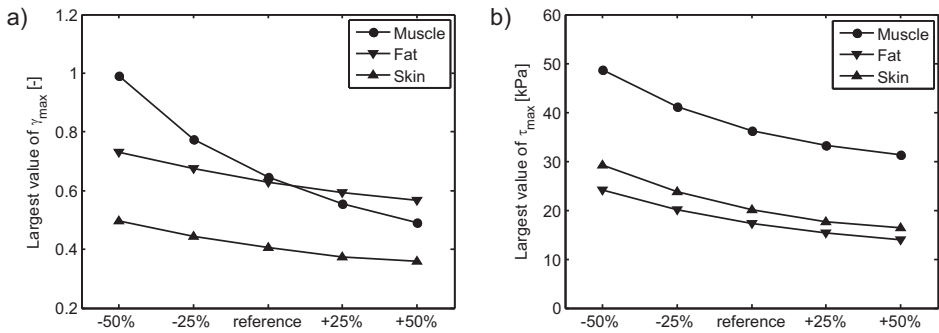
Figure 6.7: Largest maximum shear strain (γ_{max}) (a) and maximum shear stress (τ_{max}) (b) in each tissue in the simulations in which the muscle stiffness was varied while the reaction force on the indenter remained unchanged.

Figure 6.8 shows the mesh contours of the simulations in which the muscle stiffness in the buttocks was increased unilaterally, superimposed on the MR images of the pig buttocks both during loading without stimulation (figure 6.8a) and during loading with stimulation (figure 6.8b). A comparison of these two MR images shows that the shape of the muscles of the left hindlimb (right side on MR image) clearly changed during the stimulation-induced contraction, as indicated by the white circles and arrows superimposed on figure 6.8b. Additionally, the ischial tuberosity slightly moved in an upward direction. Both effects are not present in the simulation.

6.4   Discussion

Recently, an animal model was used to investigate the effect of electrical stimulation of muscle tissue on the internal deformations in the buttocks (Solis et al., 2011b,c). In the present study, an animal-specific FE model was developed to estimate the internal mechanical state of the soft tissues in the buttocks during loading. First, a sensitivity analysis was performed to assess the influence of the material properties on the model results. Secondly, the effect of a change in muscle stiffness on the stress and strain distribution in the FE model was investigated, since muscle stiffness can change with time, either chronically due to SCI or intermittently during electrical stimulation. The stiffness of the muscle was also increased unilaterally to simulate the experiments with stimulation and investigate the contribution of increased muscle stiffness to the changes in deformation that occur during stimulation.
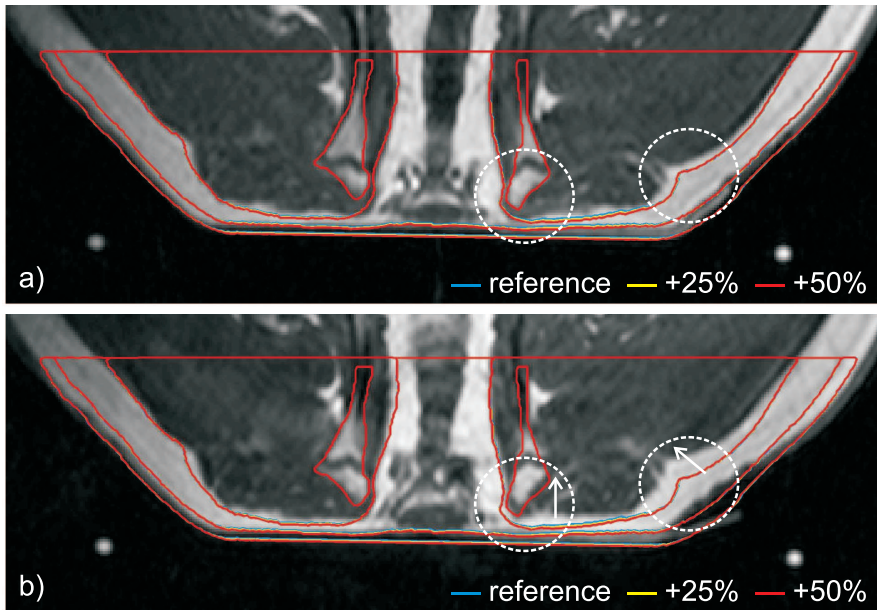
Figure 6.8: Mesh contours of the simulations in which the muscle stiffness was increased unilaterally to simulate the experiment in which electrical stimulation was applied. a) Mesh contours superimposed on the MR image during loading without stimulation. b) Mesh contours superimposed on the MR image during loading with stimulation. The white circles indicate where the FE model deviates most from the real contours of the buttocks during stimulation. The arrows show the direction in which the muscle tissue moved during contraction.

The geometry of the buttocks was derived from high-resolution MR images of the animal before loading, and used to create the FE mesh. Additionally, the displacement of the indenter during loading was derived from images of the buttocks during loading. A plane stress situation was assumed for the model, because this resulted in a better agreement with the MR images than a plane strain assumption (data not shown). Although a 3D approach could give a better estimation of the internal deformations, the model that was developed in the present study corresponded well with the MR images of the deformed buttocks with the current 2D approach. Therefore, it is expected that the in-plane strains and stresses in the model are reasonable estimates of the actual in-plane deformations in the loading experiments.

The calculated deformations of the reference model are similar to those recently reported in patient-specific FE models of the buttocks of healthy volunteers (Linder-Ganz et al., 2007, 2008), and the largest strains in the muscle were close to the recently suggested damage threshold (Ceelen et al., 2008b; Loerakker et al., 2010). High strains were also observed in the fat layer, corresponding to a previous FE model, which reported strains

in fat tissue often exceeding those in the muscle (Oomens et al., 2003). The location where deformation-induced tissue damage starts for DTI is determined by the internal deformations and the susceptibility of each tissue. The results of the present study raise the question whether there is also a deformation threshold for fat, and how this compares to the threshold of skeletal muscle. To study the aetiology of DTI, it is therefore important to investigate the damage process of fat tissue as well.

The sensitivity analysis of the reference model showed that the internal strains in the three tissues depend considerably on the relative stiffnesses of the tissues. The largest strains in muscle and fat were comparable when the muscle tissue was modelled with a stiffness value twofold that of fat (figure 6.5). At lower stiffness ratios, strains were larger in the muscle, whereas the largest strains were evident in the fat when muscle was more than twice as stiff. These results demonstrate the importance of using accurate material properties of the three tissues in the model to obtain reliable estimates of the internal deformations and to avoid underestimation of the deformations in the softer fat tissues. In the present study, the shear moduli of muscle, fat, and skin were derived from different experimental studies using different methods. Ultimately, the relative material properties of the three tissues should be determined in a single study using the same methodology which could, for example, be achieved using MR or ultrasound elastography (Mariappan et al., 2010; Parker et al., 2011). In addition, FE models may also be used in combination with imaging methods to determine material properties (Then et al., 2007, 2009). The sensitivity analysis further revealed that the stress distribution was less affected by the relative stiffnesses of the three tissues. Indeed, a variation of tissue properties mainly caused a change in absolute stress values. The relative proportions of the stress levels in the three tissues were less affected, with the largest stresses always located in the muscle tissue.

In the sensitivity analysis, material properties were varied while the displacement of the indenter was the same in each simulation. To investigate the effect of muscle stiffness on the internal deformations, it was assumed that the body weight would not change. Therefore, additional simulations were performed in which the muscle stiffness was varied and the reaction force was kept constant. As a result, the displacement of the indenter varied with a change in muscle stiffness. In these simulations, a change in muscle stiffness had a large influence on the maximum shear strain distribution in the FE model. This was particularly evident in the muscle layer where a considerable increase in strain was observed when the muscle stiffness was decreased by 50 % (figure 6.7a). An increase in muscle stiffness caused a decrease in muscle strains to a value below the strains in the fat layer, indicating that electrical stimulation during loading may have a large effect on the strains in the muscle. It is worthy of note that there is still a lack of data concerning the change in transverse muscle stiffness due to either SCI or contraction, and thus it is not clear what physiological change can occur in muscle stiffness. Thus the stiffness

changes applied in the present study may not totally represent those occurring in a clinical setting. Nonetheless, the results show that a change in muscle stiffness can have a large influence on the strain distribution in the buttocks.

A comparison of the simulations with increased muscle stiffness on one side of the buttocks with MR images of the experiments with applied stimulation, revealed that increasing the muscle stiffness alone was not sufficient to simulate its effect. Electrical stimulation clearly changed the buttock shape during contraction. Therefore, to investigate the effect of electrical stimulation on the internal tissue deformations during loading, it is necessary to include muscle contraction in the constitutive behaviour of the muscle tissue in the FE model, which will also require an extension of the model to 3D.

In summary, an animal-specific FE model was developed to estimate internal tissue deformations in the buttocks during loading. The model showed the presence of large strains in both the fat and muscle layer, with a load of only 25 % of the body weight on the ischial tuberosities. A change in muscle stiffness had a large effect on the stress and strain distribution in the buttocks. Particularly in the muscle layer, a large change in maximum shear strain was observed, which indicates that electrical stimulation may have a large effect on the strain distribution in the buttocks, either temporarily by changing the shape of the muscles (Levine et al., 1990a) and reducing the internal tissue strains during loading (Solis et al., 2007; Curtis et al., 2011), or by preventing the decrease in muscle stiffness and thickness due to SCI (Bogie et al., 2006). The model of the present study was developed to estimate tissue deformations in one healthy animal. In future studies, the current approach may be used to investigate the effects of changes in the muscle tissue on tissue deformations in other animals or humans, in particular those with SCI. The inclusion of muscle contractile behaviour in the model could give valuable insights into the changes that occur in the mechanical state of the tissues during electrical stimulation.

Acknowledgements

Chapter 7

Plasma variations of biochemical markers for deep pressure ulcers in able-bodied and spinal cord injured subjects

7.1   Introduction

A pressure ulcer is a local lesion to the skin and/or underlying tissues, resulting from prolonged mechanical loading involving pressure alone or in combination with shear and/or friction (NPUAP and EPUAP, 2009). Two types of pressure ulcers can be distinguished. Superficial pressure ulcers involve the skin layer only, while deep pressure ulcers are often initiated in deep muscle tissue adjacent to bony prominences (Bouten et al., 2003). The latter ulcers only become apparent at the skin surface when tissue destruction is extensive having progressed up from the muscle layers. Accordingly, early detection and prevention is problematic and subsequent treatment is prolonged with a variable prognosis.

Subjects with spinal cord injury (SCI) are particularly susceptible to deep pressure ulcers due to their inherent impaired sensitivity, disuse muscle atrophy and impaired vascularity (Scelsi, 2001; Rappl, 2008). Accordingly, the prevalence of pressure ulcers in this population has been studied frequently to identify risk factors and determine the individual susceptibility to pressure ulcer development (Garber et al., 2000; Chen et al., 2005). For example, Rodriguez and Claus-Walker (1988) postulated that the established change in skin resistance to external forces post SCI could be attributed to breakdown of the structural protein collagen. They reported increased levels of collagen degradation products, hydroxylysine and hydroxyproline, in a small group of SCI subjects, suggesting a decreased skin stiffness and strength. Other research for identifying persons at risk of pressure ulcers examined the metabolites of sweat collected at the skin surface. In compressed skin, the impairment of both blood supply and lymphatic drainage could lead to an increased production of urea, lactate and urate (Polliack et al., 1993, 1997). However, the simple method of sweat collection requires a significant sweat volume for analysis and thus may not prove appropriate for SCI subjects with altered or reduced sudomotor function.

In the present study, circulatory levels of biochemical markers for muscle damage were investigated to explore the possibility of using them for detection of deep pressure ulcers. Three markers of muscle damage and one marker of inflammation were chosen for investigation:

- Creatine kinase (CK), an enzyme with a combined molecular mass of 86 kDa involved in cellular energetics and muscle metabolism, which is mostly found in skeletal and cardiac muscle and the brain (Sorichter et al., 1999).

- Myoglobin (Mb), a cytoplasmic haemoprotein of 18 kDa, which is present in skeletal and cardiac muscle (Sorichter et al., 1999).

- Heart-type fatty acid binding protein (H-FABP), a protein of 15 kDa involved in

the cellular uptake, transport, and metabolism of fatty acids in skeletal and cardiac muscle and the kidneys (Sorichter et al., 1999).

- C-reactive protein (CRP), a ubiquitous marker in inflammation, tissue damage and infection (Pepys and Hirschfield, 2003).

The concentrations of these proteins in the circulation are determined by the release from the injured tissue and the clearance by the kidneys (Clarkson and Hubal, 2002). In a study with human volunteers, levels of CK, Mb, and H-FABP all increased after eccentric exercise (Sorichter et al., 1998). The time to reach peak concentration and subsequently return to baseline levels was shorter for Mb and H-FABP when compared to CK, which can be explained by the differences in molecular mass of these proteins. These markers have also been used to detect cardiac muscle damage. Skeletal muscle damage can be distinguished from cardiac muscle damage by calculating the ratio of Mb over H-FABP, which is considerably higher in case of skeletal muscle damage (20-70) when compared to cardiac muscle damage ($\sim$5) (Van Nieuwenhoven et al., 1995). With respect to pressure ulcers, several studies have reported considerable increases in CK levels in serum and wound exudate in animal studies on deep pressure ulcers (Hagisawa et al., 1988; Sari et al., 2008; Minematsu et al., 2010). Furthermore, higher serum levels of CRP were observed in SCI subjects with pressure ulcers than in subjects without ulcers (Scivoletto et al., 2004; Frost et al., 2005; Morse et al., 2008).

This study represents a preliminary investigation of the basal circulatory levels and variations of these four markers in able-bodied subjects and SCI subjects with a low level lesion. To assess whether these markers are appropriate for early detection, the following questions are of importance:

1. What are the baseline circulatory levels of these markers in SCI subjects and is there a difference compared to able-bodied individuals?

2. How large are the variations of the markers within a day and during a week?

3. Are the variations smaller than variations expected when a pressure ulcer develops or exists?

4. Are there any relationships between the circulatory levels of these markers?

7.2   Materials & Methods

7.2.1   Participants

The participants in this study included eight male subjects with traumatic SCI (mean age 56, range 40-68), who were former patients of a rehabilitation centre (Adelante, Hoensbroek, The Netherlands). Of these, one subject, 11 years post injury, presented with a category II pressure ulcer and had American Spinal Injury Association (ASIA) Impairment Scale classification A (Marino et al., 2003), with neurologic level of injury T12 (SCI+PU group, $n = 1$). This subject also suffered from diabetes, hypertension, and high cholesterol, and had a stoma. Of the remainder (SCI group, $n = 7$), who were between one and 44 years post injury, six participants without pressure ulcers had an ASIA-A classification and one had an ASIA-B classification (Marino et al., 2003). The neurological level of injury in these seven subjects was between T11 and L3. One of these subjects suffered from diabetes and high cholesterol and two subjects suffered from hypertension. For comparison, a control group of aged-matched male subjects was recruited from volunteers at the Eindhoven University of Technology, consisting of seven able-bodied participants (control group, $n = 7$). The study was approved by the Medical Ethical Review Committee of the Adelante rehabilitation centre and all participants signed the informed consent form.

7.2.2   Experimental protocol

Blood was withdrawn by a standard venipuncture from all subjects on five consecutive days. One blood sample was taken for four days in the early afternoon. On the fifth day, three samples were taken corresponding to the morning, early and late afternoon. Blood samples were collected in two 5 mL vacutaier collection tubes, which contained Olefin gel, heparin and lithium to prevent coagulation. Blood was centrifuged at 3000 rpm for 10 min. Plasma was transferred into two vials, one of which was analysed for CK, Mb and CRP content using an Analyzer Roche type Modular (Atrium Medical Centre Heerlen, The Netherlands). The vial used for H-FABP analysis was stored at -80 °C, and subsequently tested with an enzyme-linked immunosorbent assay (ELISA). Basic clinical and demographic information was obtained by a questionnaire and a diary was filled in by all participants.

7.2.3   Biochemical analysis

CK catalyses the reaction of phosphocreatine with ADP to creatine and ATP. The NADPH content, which is directly proportional to the CK content, was measured photometrically. The detection range was 3 - 2300 U/L (Roche, Switzerland). The CRP content was also determined by photometry, with a detection range of 1 - 350 mg/L (Roche, Switzerland). Electrochemiluminescence, a sandwich principle based immunoassay, was used for Mb detection in plasma samples, with a detection range of 21 - 3000 ng/mL (Roche, Switzerland). The coefficients of variation for total precision of the CK, CRP and Mb concentrations were < 1.4 %, < 6.2 %, and < 5.2 %, respectively. H-FABP ELISAs (Hycult Biotech, Uden, The Netherlands) were used to detect the concentration of H-FABP in all samples. This assay is a solid-phase ELISA based on the sandwich principle. Samples and standard were tested in duplicate and averaged. The detection range of the ELISA was 0.1 - 25.0 ng/mL.

7.2.4   Statistical analysis

To compare the marker concentrations of the able-bodied and SCI subjects, the median marker concentrations over the five days were calculated for each individual. Subsequently, the presence of significant differences in median marker levels between the groups was determined using the nonparametric Wilcoxon rank sum test. The presence of diurnal variations in marker levels was investigated by applying the nonparametric Friedman test to the marker concentrations that were measured in the morning, and the early and late afternoon of the same day, followed by a Bonferroni post-hoc test. Correlations between the marker levels were assessed using the Spearman rank correlation coefficient. Test results were considered significant if $p < 0.05$.

7.3   Results

7.3.1   Inter-subject variations

The marker concentrations of the four proteins on the five consecutive days are shown in figure 7.1, indicating that the intra-subject variations were small compared to the inter-subject variations in marker levels.

Figure 7.1: Concentrations of CK (a), Mb (b), H-FABP (c), and CRP (d) for all subjects in the samples that were taken on five consecutive days.

For CK in the control group, the largest values for both concentration and variation were observed in subject 3 (185-599 U/L). In the SCI group without pressure ulcers, the greatest concentrations were present in subject 7 (306-467 U/L). The SCI+PU subject showed relatively low CK levels with a small variation (30-70 U/L). For Mb, only minor inter-subject variations were observed for the control group. The greatest Mb concentrations were found in subject 4 (128-171 ng/mL) of the SCI group. The Mb levels of the SCI+PU subject were comparable to both other subject groups. For H-FABP, the inter-subject variations were also greater than the intra-subject variations, although the differences in the former were smaller than for CK. SCI subject 7 (1.6-7.1 ng/mL) showed the largest variation in H-FABP levels, and the highest concentrations were observed for the SCI+PU subject (6.7-9.3 ng/mL). The largest variations in CRP levels were found in control subject 6 (2-7 μg/mL), and SCI subjects 3 (8-14 μg/mL), 4 (12-22 μg/mL), and 5 (4-14 μg/mL). The highest CRP concentrations were present in the SCI+PU subject (24-29 μg/mL).

7.3.2   Diurnal variations

Figure 7.2 shows the marker concentrations of the samples that were taken in the morning, and the early and late afternoon of the same day. Close examination of the diurnal data using the Friedman test indicated some significant differences between time points in the group of SCI subjects. In particular, the concentrations of Mb in the morning were greater than those measured in the late afternoon ($p = 0.03$). For H-FABP, the morning concentrations were greater than those in the early afternoon ($p = 0.02$). For the other markers, no significant differences in concentration were present between the different time points in both the control and SCI groups.

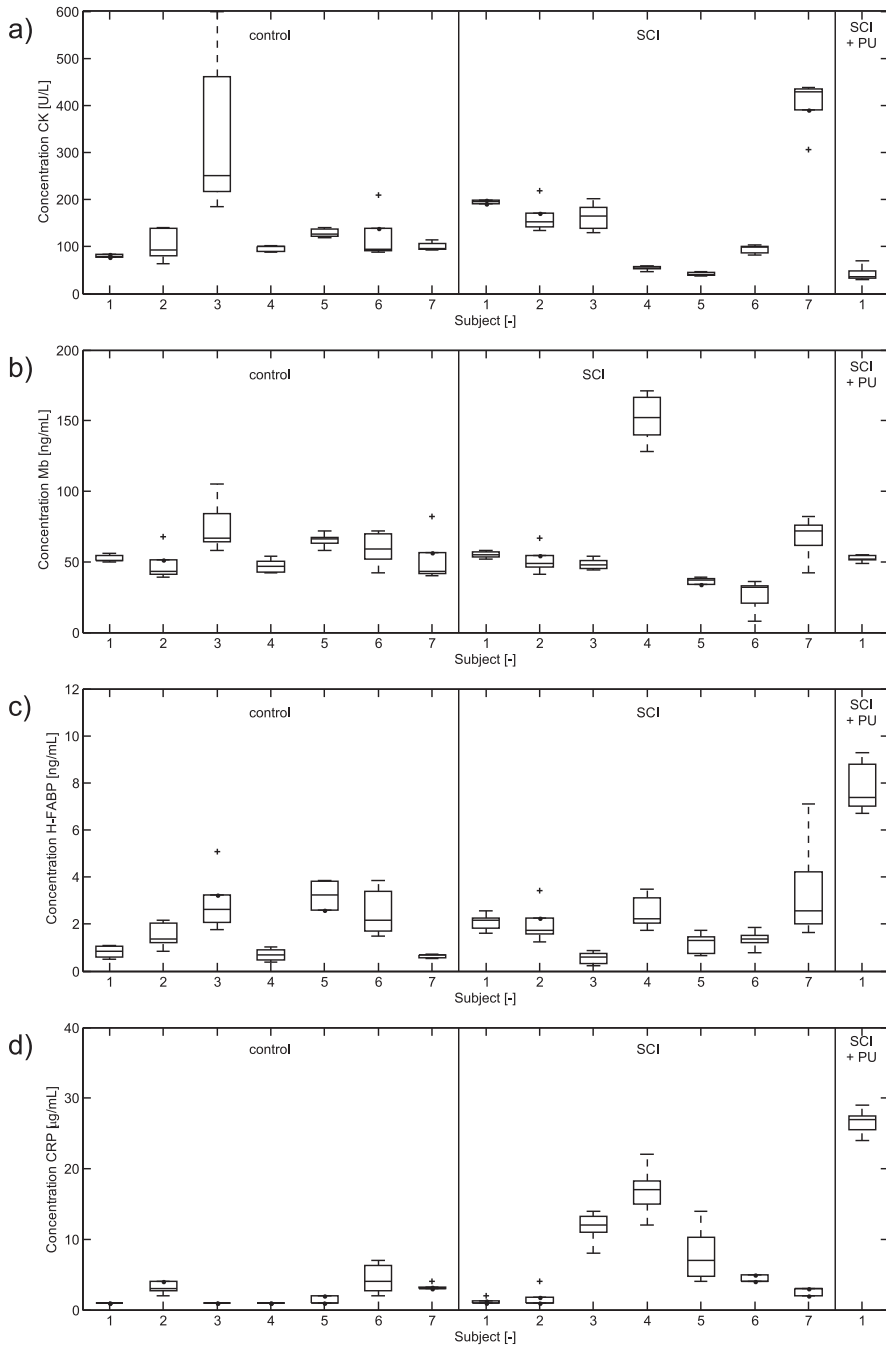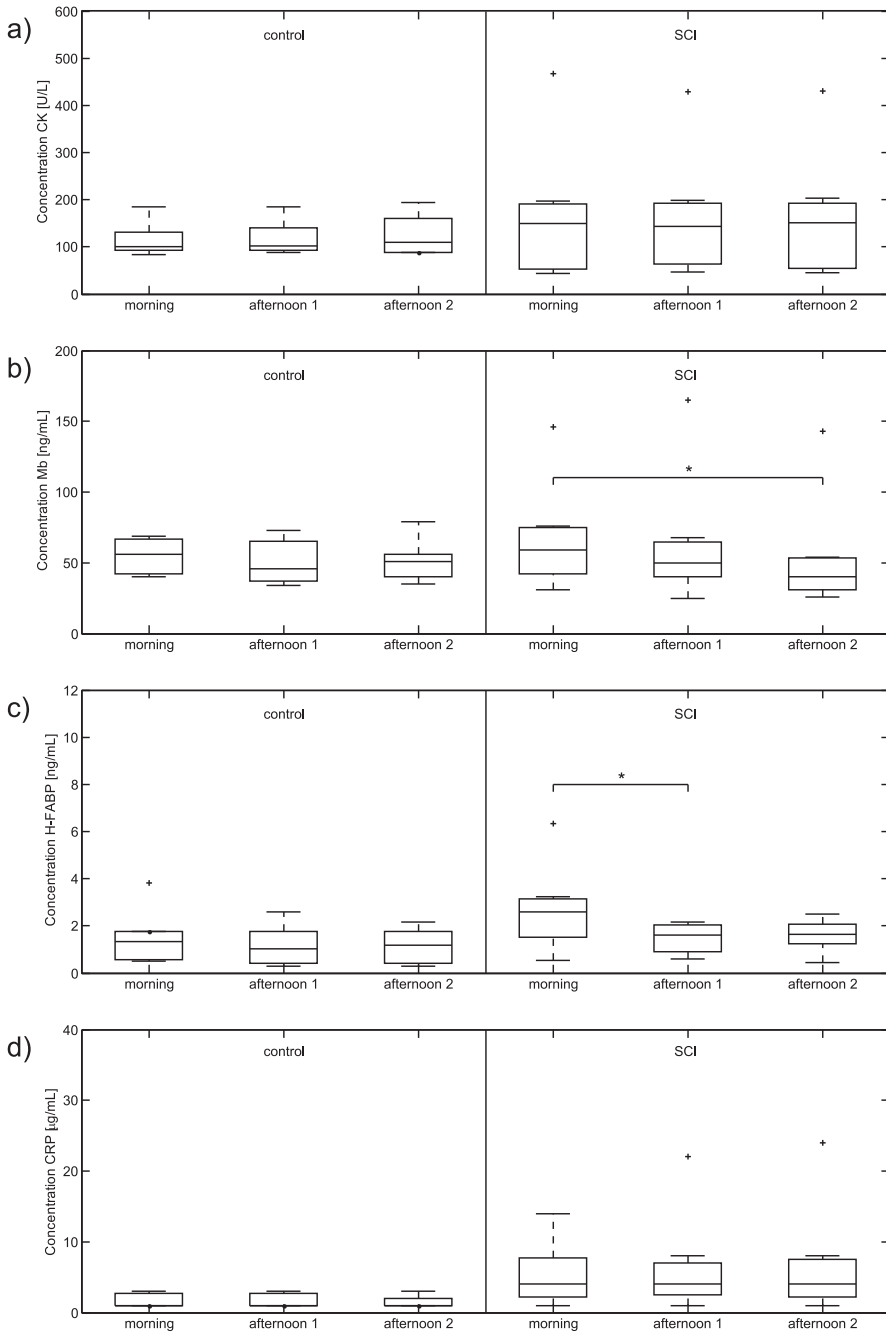**Figure 7.2:** Concentrations of CK (a), Mb (b), H-FABP (c), and CRP (d) for all subjects in the three samples that were taken in the morning, and the early (1) and late (2) afternoon of the same day. * Significant difference between time points.

7.3.3   Comparison of groups

The group data of the marker concentrations on the five consecutive days are summarised in table 7.1. For the group comparisons, the SCI group was presented both as a single group and divided into two groups according to their individual motor function; SCI active (SCI-A, subjects 1-3,7) and SCI non-active (SCI-NA, subjects 4-6). The group data are also displayed in figure 7.3. The Wilcoxon rank sum test revealed no significant differences between the groups of able-bodied and SCI subjects for any of the markers. Also, no significant differences were found between the SCI-A and SCI-NA groups.

Table 7.1: Concentrations of the markers of muscle damage (CK, Mb, and H-FABP), and inflammation (CRP) in the control, SCI, and SCI+PU groups on the five consecutive days. The SCI group was presented both as a single group and divided into two groups according to their individual motor function; SCI active (SCI-A, subjects 1-3,7) and SCI non-active (SCI-NA, subjects 4-6).

Group	CK [U/L]	Mb [ng/mL]	H-FABP [ng/mL]	Ratio Mb/H-FABP	CRP [μg/mL]
Control (n=7)					
Median	102	54	1.3	39	1
Range	64-599	34-105	0.3-5.1	15-126	1-7
SCI (n=7)					
Median	144	50	1.7	29	4
Range	38-467	8-171	0.2-7.1	6-200	1-24
SCI-A (n=4)					
Median	194	53	1.8	29	2
Range	130-467	29-82	0.2-7.1	10-200	1-14
SCI-NA (n=3)					
Median	54	37	1.5	29	5
Range	38-103	8-171	0.7-3.5	6-88	3-24
SCI+PU (n=1)					
Median	33	54	8.6	6	27
Range	27-70	49-55	6.7-9.3	6-8	24-30

Figure 7.3: Group results of the marker concentrations of CK (a), Mb (b), H-FABP (c), and CRP (d) on the five consecutive days. The SCI group was presented both as a single group and divided into two groups according to their individual motor function; SCI active (SCI-A) and SCI non-active (SCI-NA).

The SCI+PU subject showed relatively low CK concentrations compared to the other groups (figure 7.3a). Furthermore, the CK concentrations in the SCI-A subjects were larger than the concentrations in the SCI-NA group, although this result could not be con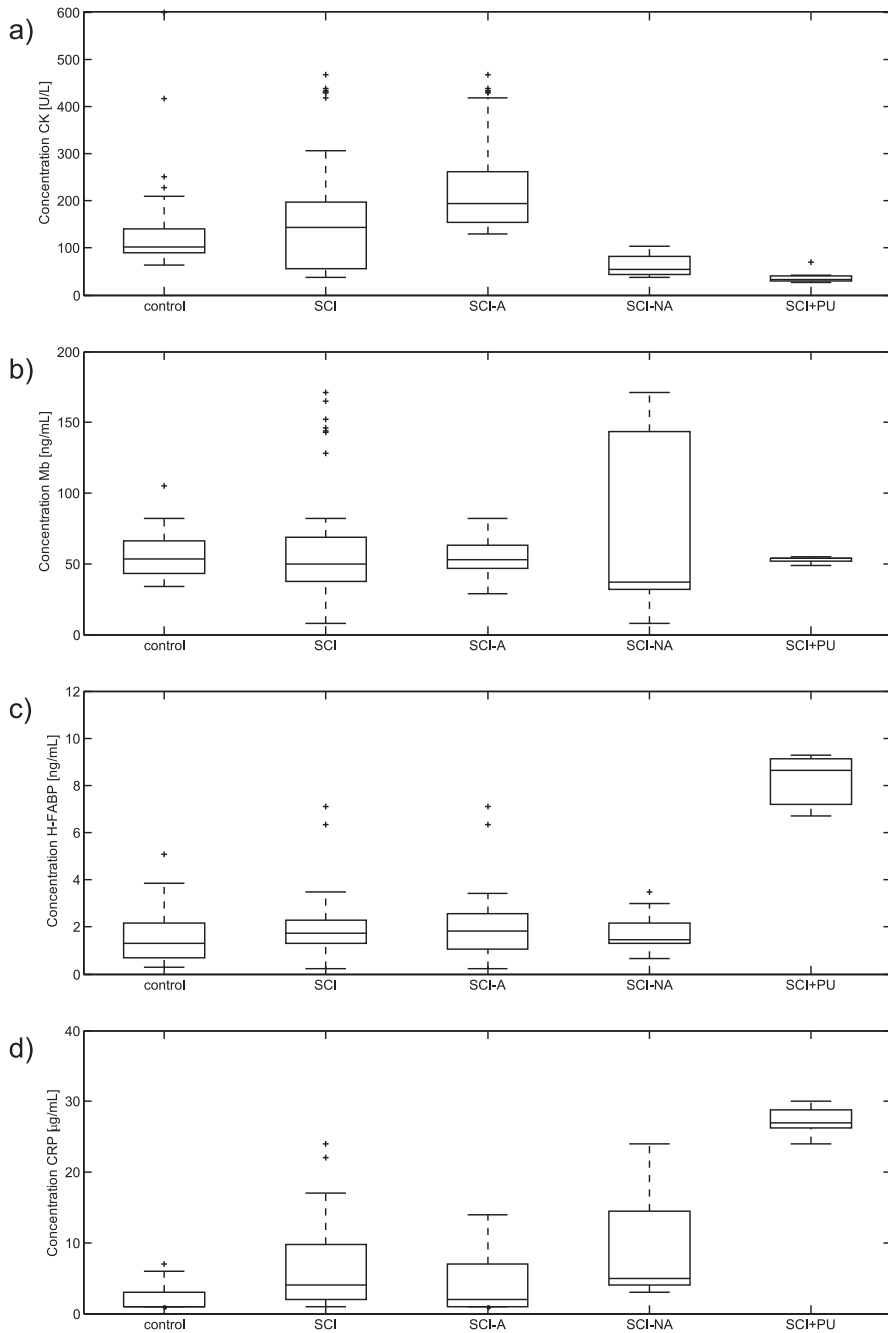firmed by statistical analysis ($p = 0.06$). The median Mb concentrations were comparable in all groups (figure 7.3b). For H-FABP, also comparable concentrations were present in the groups of the able-bodied and SCI subjects (figure 7.3c). The median ratio of Mb over H-FABP showed values within the range for skeletal muscle damage (20-70 (Van Nieuwenhoven et al., 1995)) for the control group and the SCI groups without pressure ulcers (table 7.1). The SCI+PU subject exhibited relatively high H-FABP concentrations, with a corresponding reduced value of the Mb/H-FABP ratio. However, similar values of this ratio were also observed for some individuals within the SCI group. In general, the CRP levels were higher in the SCI subjects than in the control group, although this result could not be confirmed by statistical analysis ($p = 0.14$). Furthermore, a trend toward higher CRP concentrations in the SCI-NA subjects compared to the SCI-A subjects was observed ($p = 0.23$) (figure 7.3d).

7.3.4   Correlations between marker concentrations

The Spearman rank correlation coefficient revealed significant correlations in four pairs of markers in the SCI group and three in the group of able-bodied volunteers (table 7.2). Positive correlations between CK and H-FABP and Mb and H-FABP were present in both groups. In addition, there was a positive correlation between CK and Mb in the control group. By contrast, there were negative correlations between CK and CRP and H-FABP and CRP in the SCI group.

Table 7.2: Significant Spearman rank correlation coefficients between combinations of markers for both the control and SCI group. The symbol 'ns' is shown if the correlation coefficient was not significant.

Combination	Control	SCI
CK – Mb	0.59	ns
CK – H-FABP	0.60	0.28
CK – CRP	ns	-0.61
Mb – H-FABP	0.74	0.68
Mb – CRP	ns	ns
H-FABP – CRP	ns	-0.29

7.4   Discussion

The present study was conducted to investigate the appropriateness of three markers of muscle damage and one marker of inflammation for the early detection of deep pressure ulcers in SCI subjects with a low thoracic or lumbar level lesion. Baseline concentrations and the variations of the markers were measured in three small groups of SCI, SCI+PU and control subjects. No significant differences were found between the groups of able-bodied and SCI subjects for any of the markers. The CRP levels in the SCI subjects were generally larger than in the able-bodied controls, although this result could not be confirmed by statistical analysis ($p = 0.14$). The one SCI+PU subject revealed relatively high H-FABP and CRP values compared to all other subjects. In addition, close examination of the SCI group revealed trends toward higher CK ($p = 0.06$) and lower CRP ($p = 0.23$) baseline values in those SCI subjects with motor function (SCI-A) compared to those lacking motor function (SCI-NA).

The results of this study reveal a small intra-subject range for all markers when compared to the inter-subject differences. It is clear that each subject has a different range of marker values, which could, in part, be explained by their different levels of activity as reported in the individual diaries. The present findings reveal significant diurnal variations within the SCI subjects for Mb and HFABP with morning values generally elevated compared to those collected later in the day, a similar trend to that previously reported with able-bodied subjects (Clerico et al., 1984; Pelsers et al., 1999). Although daily activities might have been expected to increase marker values, the observed decrease may be a direct result of an increased glomerular filtration rate during the day (Pelsers et al., 1999).

The SCI group demonstrated relatively high CRP levels compared to the control group, supporting findings from recent studies (Frost et al., 2005; Wang et al., 2007). CRP plasma levels are affected in multiple situations, increasing rapidly after both tissue damage and many forms of inflammation and infection. This marker has often been used with SCI subjects and its increase has also been reported in individuals with pressure ulcers (Scivoletto et al., 2004; Frost et al., 2005; Morse et al., 2008). However, other pro-inflammatory cytokines, such as IL-2R and IL-6, may also be appropriate as has recently been reported in studies with SCI subjects (Segal et al., 1997; Davies et al., 2007).

Close examination of the SCI group revealed trends toward higher baseline concentrations of CK for the SCI-A subjects compared to both the SCI-NA and control groups. The SCI-A group regularly walked with crutches or a parapodium during the week, which represents intensive and strenuous exercise for the muscles, thereby releasing relatively large amounts of CK into the circulation. This result is equivalent to the findings that able-bodied subjects who regularly exercise tend to have higher circulatory levels of CK

than their sedentary counterparts (Apple et al., 1984; Evans et al., 1986). In addition, relatively low CRP levels were present in the SCI-A group compared to the SCI-NA group, which is consistent with the findings of a recent study in which decreasing levels of CRP were reported with increasing levels of activity in a chronic SCI group (Morse et al., 2008).

Correlational analyses yielded positive relationships which were statistically significant between CK and H-FABP and Mb and H-FABP for both SCI and control groups and, additionally in the control group, a positive correlation between CK and Mb (table 7.2). These findings imply a simultaneous increase in Mb, H-FABP and CK, the former two markers being of similar molecular size (15-18 kDa). By contrast, the larger CK molecule (86 kDa) would lead to a predicted delay in its increase compared to H-FABP and Mb. Indeed, research examining myocardial infarction and exercise revealed an increase in Mb and H-FABP at similar time points and a delayed offset in CK (Adams et al., 1993; Glatz et al., 1998; Sorichter et al., 1998). In addition, in the SCI group a significant negative correlation was found between H-FABP and CRP and CK and CRP (table 7.2), corresponding to the results of Morse et al. (2008) in which CRP levels of SCI subjects were negatively correlated with their activity levels.

It is worthy of note that research focused on detection of acute myocardial infarction by using Mb and H-FABP showed a larger increase in concentration after myocardial infarction than the variations observed in the present study (Van Nieuwenhoven et al., 1995; Glatz et al., 1998). Additionally, considerable increases of CK levels in serum and wound exudate were reported in animal studies on deep pressure ulcers (Hagisawa et al., 1988; Sari et al., 2008; Minematsu et al., 2010). Furthermore, increased levels of CRP were present in SCI subjects with pressure ulcers compared to subjects without ulcers (Scivoletto et al., 2004; Frost et al., 2005; Morse et al., 2008). Since these elevations in marker levels were much larger than the intra- and inter-subject variations observed in the present study within a period of five days, it can be proposed that this combination of four markers may prove appropriate for the early detection of deep pressure ulcers.

In the present study, only one volunteer with a pressure ulcer was recruited. This subject showed relatively low CK concentrations compared to both the SCI and control subjects, which can be attributed to a decreased activity of this individual. The CRP levels were increased with respect to all individuals without ulcers, presumably as a result of the inflammatory response associated with the pressure ulcer. The H-FABP concentrations in this subject were also high compared to the SCI group and the able-bodied controls, whereas the Mb levels were comparable to the other subject groups. Therefore, the Mb/H-FABP ratio was very low, although it was still within the range reported by Pelsers et al. (1999). Most probably, the large H-FABP concentrations of this subject are still within the baseline variations. Indeed, it is unlikely that this increase was a di-

rect result of the pressure ulcer, as the category II ulcer associated with this subject does not involve muscle tissue. It would, therefore, be interesting to investigate the plasma concentrations of these four markers in subjects with a category IV ulcer or deep tissue injury, although the latter type of pressure ulcers is particularly difficult to identify.

The selected muscle damage markers are separately not unique indicators for skeletal muscle damage as they are also present in cardiac tissue. The ratio Mb/H-FABP has been reported to distinguish between damage in these two muscle tissues (Van Nieuwenhoven et al., 1995). In the present study, however, comparison between SCI and control subjects was unremarkable, both cases yielding considerable variations, as was evident in a study on healthy subjects with a wide age range (Pelsers et al., 1999). This large variation in the Mb/H-FABP ratio is probably caused by the fact that the baseline H-FABP concentration is relatively small, thereby having a large influence on the value of the ratio.

The results of this study raise a number of issues, if markers are to be used to assess early changes in the integrity of skeletal muscles. For example, the diurnal variations of Mb and H-FABP suggest the importance of withdrawing blood at a fixed time point. Indeed such a recommendation was made in a recent study measuring the release of muscle damage and inflammatory markers in response to eccentric exercise in young healthy subjects (Miles et al., 2008). Another important issue involves the time period between sample testing. Assuming that the rise in markers is a rapid process and, in the worst case scenario, the pressure ulcer develops very rapidly, it might therefore be advisable to test marker levels every day, particularly with high-risk subjects. For those more likely to be susceptible to slowly developing pressure ulcers, a longer time period between sample withdrawals may prove adequate. Finally, as the intra-subject variations in marker levels were smaller than the inter-subject variations, it is important to determine the baseline variations of an individual to be able to define a threshold above which an increase in marker levels may indicate the development of a pressure ulcer.

Only a small number of SCI subjects with a low level lesion participated in the present study. An extended study might also include subjects with higher level lesions, who generally present extended disuse atrophy leading to decreased muscle volume. In such cases, more adipose tissue is present and other more adipose or skin-related markers, such as hydroxylysine or hydroxyproline (Rodriguez and Claus-Walker, 1984, 1988; Rodriguez and Garber, 1994), could be included in the blood analysis. In addition, further studies might include female SCI subjects in which case the hormonal influence on muscle markers would need to be accommodated (Pelsers et al., 1999; Brancaccio et al., 2007).

In summary, in the present study it was shown that each subject had a personal range of concentrations for all four biomarkers which could, in part, be explained by their level

of physical activity. These intra-subject variations appeared to be smaller than the inter-subject variations. No differences in baseline concentrations were found in CK, Mb and H-FABP between the SCI and control group. For CRP, relatively high concentrations were observed in the SCI group when compared to the able-bodied controls, although this could not be confirmed by statistical analysis. The present study demonstrates the potential of a combination of muscle damage and inflammation markers for the early detection of deep pressure ulcers, although research in a larger group of subjects is necessary to confirm the findings. In assessing biochemical marker levels in the circulation, it is important to consider their relative molecular size, as this will undoubtedly influence their temporal profile. An ideal marker for deep pressure ulcers would be found in high concentrations in the muscle, is absent or present at very small concentrations in other tissues, and will be released rapidly after muscle damage and at levels proportional to the degree of damage.

In appendix A, the results of a pilot study are shown in which the concentrations of Mb and H-FABP in serum and urine were measured in an animal model after mechanical loading. In this study, it was shown that Mb levels increase considerably in case of muscle damage in both serum and urine, which further indicates that biochemical markers may indeed be used for the early detection of muscle damage induced by mechanical loading.

Acknowledgements

Chapter 8

General discussion

8.1   Introductory remarks

The main goal of the present thesis was to study the individual roles of deformation, ischaemia, and reperfusion in the development of deep tissue injury (DTI). Additionally, a series of explorative studies was performed to examine the potential use of biochemical markers that are present in the circulation for the early detection of DTI. Since DTI often arises in muscle tissue, the focus of this thesis was on the aetiology and early detection of pressure-induced skeletal muscle damage.

The contributions of the aetiological factors were investigated with an established animal model for DTI (Stekelenburg et al., 2006a,b), which has previously been used to study the damage process of skeletal muscle during 2 h of continuous loading. In this thesis, additional short loading protocols were applied to further investigate the role of deformation (chapter 3). For this a finite element (FE) model, that was previously developed by Ceelen et al. (2008a), was substantially improved to enable a local comparison of deformation with damage (chapter 2). Furthermore, the duration of the experiments was extended to periods of 6 h to investigate the contributions of ischaemia and reperfusion to the damage process (chapters 4-5). The previously developed numerical methods were also applied to a different animal model to investigate the effect of muscle stiffness on the internal deformations in the different tissue layers of the buttocks (chapter 6).

With reference to the early detection of DTI, the variation in baseline plasma levels of a number of markers for muscle damage and inflammation was investigated in groups of able-bodied and SCI subjects (chapter 7). In addition, a pilot study was performed during an internship at Northwestern University in which the concentrations of selected markers in both blood and urine were measured after muscle damage in an animal model (appendix A).

8.2   Model systems

Both experimental and computational models were used to study the aetiology of DTI and the potential for early detection. The benefits and limitations of these methods will be evaluated in this section.

8.2.1   Experimental models

In chapters 2-5, Brown-Norway rats were used to examine the damage process of skeletal muscle. The role of deformation was investigated by applying a mechanical load to the tibialis anterior muscle of the rat hindlimb using an indenter. An estimation of the internal local deformations in the muscle using animal-specific FE models (Ceelen et al. (2008b) and chapter 2), revealed that the applied deformations were similar to those recently reported in patient-specific FE models of the buttocks of healthy volunteers (Linder-Ganz et al., 2007, 2008). Changes in tissue integrity and perfusion were monitored with T_2-weighted and contrast-enhanced magnetic resonance imaging (MRI), respectively. Since these methods provided indirect measures of tissue integrity and perfusion, a frequent comparison of the results with histological analysis was required. In the present thesis, this histological analysis was focused on tissue morphology, whereas in future studies other techniques may be employed to study different aspects of cellular and tissue damage, such as apoptosis (Siu et al., 2009). The advantage of using MRI during the experiments over histology is that it enabled the investigation of spatial and temporal changes in the tissue. Moreover, with this approach it was possible to carefully monitor the experimental loading conditions which, in combination with numerical modelling, improved the interpretation of the experimental results.

Brown-Norway rats were also used in pilot studies involving biochemical markers for the early detection of DTI. For this, blood sampling was added to the experimental protocol to detect muscle damage induced by mechanical loading. However, due to limited size of the Brown-Norway rats and the difficulties with taking blood samples, this animal model proved unsuitable for this experimental approach. Therefore, additional experiments were performed with larger Sprague-Dawley rats, during an internship at Northwestern University, where the concentrations of biochemical markers of muscle damage in blood and urine after mechanical loading were determined (appendix A). Although the application of the mechanical load proved problematic, the results did reveal increases in biomarker levels in both blood and urine. This suggests that these larger rats are appropriate for use in future studies examining the early detection of muscle damage.

8.2.2   Numerical models

In chapters 2, 3, and 5, the role of deformation in the aetiology of DTI was investigated with an animal model in combination with FE modelling (figure 8.1). A dedicated approach was adopted for the FE models, where the individual geometry and loading conditions of each animal were derived from MR images of the experiments and incorporated in the model. This approach enabled the comparison of muscle deformation and

damage within the same experiment, and therefore resulted in an improved interpretation of the experimental results. In addition, by compensating for the differences in both tissue geometries and loading conditions that determine the level of tissue deformation, the animal-specific FE models could explain a large part of the variation in the degree of damage observed in the experiments. Moreover, the differences in the level of deformation between experiments could be used advantageously to study the relationship between deformation and damage.
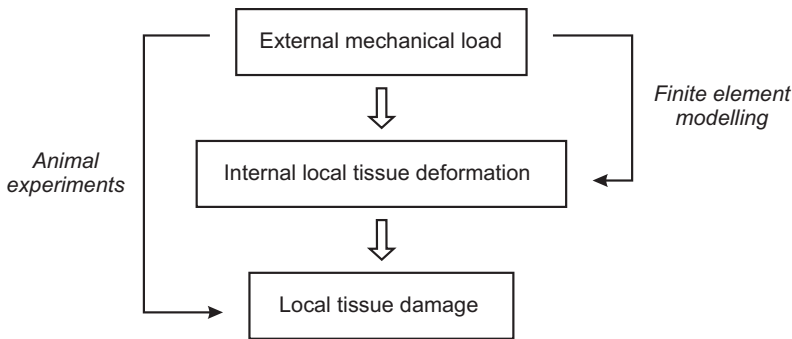
Figure 8.1: Schematic overview of the combined experimental-numerical approach that was used to investigate the role of deformation in the aetiology of DTI. Animal experiments were performed in which the damage evolution due to compressive loading was studied with MRI. Dedicated FE models were developed to estimate local tissue deformations during loading.

The developed numerical methods are also applicable to other animal models in which different loading conditions are applied. An example of this is illustrated in chapter 6, where these methods were applied to simulate experiments involving the compression of the buttocks in a porcine model for DTI.

8.2.3   Ethical considerations

In the present thesis, animal models have been used to study the aetiology of DTI and a possible method for its early detection. Although valuable results could be obtained using this approach, it is important to reduce and ultimately prevent the use of laboratory animals in scientific research. The degree of discomfort in the animals was kept to a minimum with the use of effective anaesthesia. Furthermore, since the goal of this thesis was to study the early development of DTI, only minor tissue damage was induced in the animals. Indeed, no pressure ulcers were created. The use of MRI enabled careful monitoring of the applied mechanical load in the experiments, which increased the

reproducibility of results. In addition, longitudinal changes in tissue integrity could be investigated noninvasively using each animal as its own control. Moreover, the use of animal-specific FE modelling in combination with the experiments enabled a better interpretation of the experimental results. This obviated the need for using a large number of animals which is, for both practical and ethical reasons, clearly beneficial to the scientific and wider communities.

8.3   Main findings and clinical implications

8.3.1   Role of deformation in the aetiology of DTI

In previous research, muscle damage due to 2 h mechanical loading was only found in experiments where a certain maximum shear strain threshold was exceeded (Ceelen et al., 2008b). The results of chapter 3 showed that a similar mechanical threshold was present for muscle damage induced by only 10 min loading, indicating that this strain threshold is a material property representing the susceptibility of skeletal muscle tissue to deformation alone. It is important to note that the deformations that were applied in this animal model are similar to those in the buttocks of seated individuals (Linder-Ganz et al., 2007, 2008). Consequently, it is most likely that muscle deformations as experienced in clinical practice are close to or can actually exceed this damage threshold, particularly in situations where people are positioned on hard surfaces such as stretchers or operating tables (Bader and White, 1998).

The results of chapter 3 also indicated that 2 h mechanical loading induced a larger area of tissue damage than 10 min loading, despite the fact that the damage threshold was similar. As a consequence, the time of load exposure will clearly influence the amount of tissue damage that develops due to deformation, which may be caused by either physiological effects or by a change in mechanical properties (Gefen et al., 2005; Nagel et al., 2009).

Intermittent load reliefs superimposed on a 2 h loading period did not affect the damage evolution (chapter 3). This result may be due to the fact that a 2 h loading period is unlikely to cause any ischaemic damage in muscle tissue (Stekelenburg et al., 2007). On the other hand, the off-loading period of 2 min could have been too brief to have a significant effect on the damage evolution (Coggrave and Rose, 2003; Makhsous et al., 2007). Nevertheless, these results do not imply that intermittent pressure reliefs are not necessary for preventing the development of pressure ulcers. Indeed, in clinical practice, intermittent load reliefs are also accompanied by a change in posture. It is expected that

the resulting redistribution of the mechanical load would inevitably influence the damage evolution and may therefore be more important during short loading periods than temporarily restoring tissue perfusion. Moreover, it is predicted that intermittent load reliefs are still necessary during prolonged loading to periodically restore tissue homeostasis and thereby prevent the occurrence of ischaemia-induced muscle damage.

Since muscle damage can develop rapidly once a deformation threshold is exceeded, it is important to minimise internal tissue deformations in subjects at risk of DTI. For example, in subjects with SCI, the internal tissue deformations during loading can be large due to a decrease in muscle thickness (Elsner and Gefen, 2008; Linder-Ganz et al., 2008). Additionally, the findings of chapter 6 indicate that a decrease in muscle stiffness after SCI may also considerably increase the internal strains. Such changes may be compensated for by the use of cushions or mattresses with appropriate thickness and stiffness, which can reduce the internal tissue deformations. Another possible solution to prevent high deformations is electrical stimulation of muscle tissue to preserve or increase thickness following muscle atrophy (Bogie et al., 2006).

8.3.2   Role of ischaemia in the aetiology of DTI

Compression-induced ischaemia causes a change in muscle metabolism, which results in an accumulation of waste products such as lactate and a decrease in pH. After a critical period of ischaemia, the accumulation of toxic metabolites and the decrease in pH have been shown to lead to tissue damage (Gawlitta et al., 2007b). In previous research, Stekelenburg et al. (2007) showed that ischaemia during a 2 h loading period did not cause any significant changes in muscle tissue. The results of chapters 4-5 showed that 4 h of ischaemia caused more severe changes in the muscle. These changes appeared to be reversible during a subsequent reperfusion period for certain areas of the rat leg. However, in specific areas of the leg where no-reflow was present, tissue damage was aggravated during the reperfusion period.

The present results indicate that ischaemia starts to cause significant changes in skeletal muscle between 2 and 4 h of loading. Up to a certain critical period, the changes that occur in the tissue during ischaemia may be reversible. Eventually, however, ischaemia will inevitably result in cell death. In situations where people are subjected to sustained mechanical loads, it is therefore important to frequently redistribute the load on the soft tissues to restrict the accumulation of ischaemic damage. In this way, subsequent reperfusion will restore tissue homeostasis instead of aggravating tissue damage.

8.3.3   The relative contributions of deformation and ischaemia

The results of chapter 5 indicate that deformation and ischaemia both contribute to the damage process during prolonged loading, each mechanism exhibiting a unique time profile. Based on these results, an hypothesis for the development of DTI can be proposed (figure 8.2). Deformations exceeding a certain threshold ϵ_i will cause the occlusion of blood vessels and thereby ischaemia. The changes in the tissue due to ischaemia will ultimately lead to tissue damage. Larger deformations where also a critical threshold ϵ_d ($\epsilon_d > \epsilon_i$) is exceeded will, apart from the ischaemia-related changes, also directly cause muscle damage.
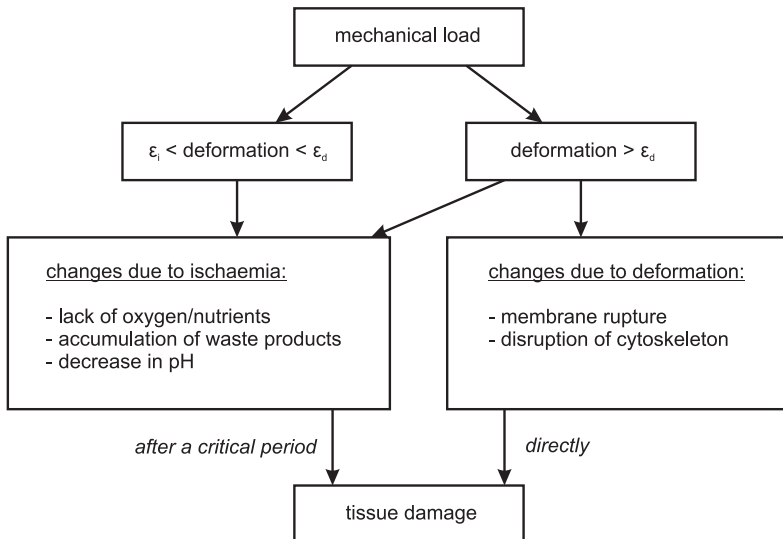
Figure 8.2: Hypothesis for the development of DTI. The damage process due to small deformations exceeding threshold ϵ_i will be determined by ischaemia and its subsequent reperfusion alone. Tissue damage induced by large deformations exceeding threshold ϵ_d ($\epsilon_d > \epsilon_i$) will be caused by both deformation and ischaemia.

The implications of this hypothesis can be explained by four separate conditions of loading (figure 8.3). Continuous loads with deformations exceeding threshold ϵ_i will lead to ischaemia-induced tissue damage when a critical threshold w_c, corresponding to the accumulation of waste products or the decrease in pH, is exceeded (figure 8.3a). This ischaemia-induced damage can be prevented by means of intermittent pressure reliefs, which enable the restoration of tissue homeostasis (figure 8.3b).
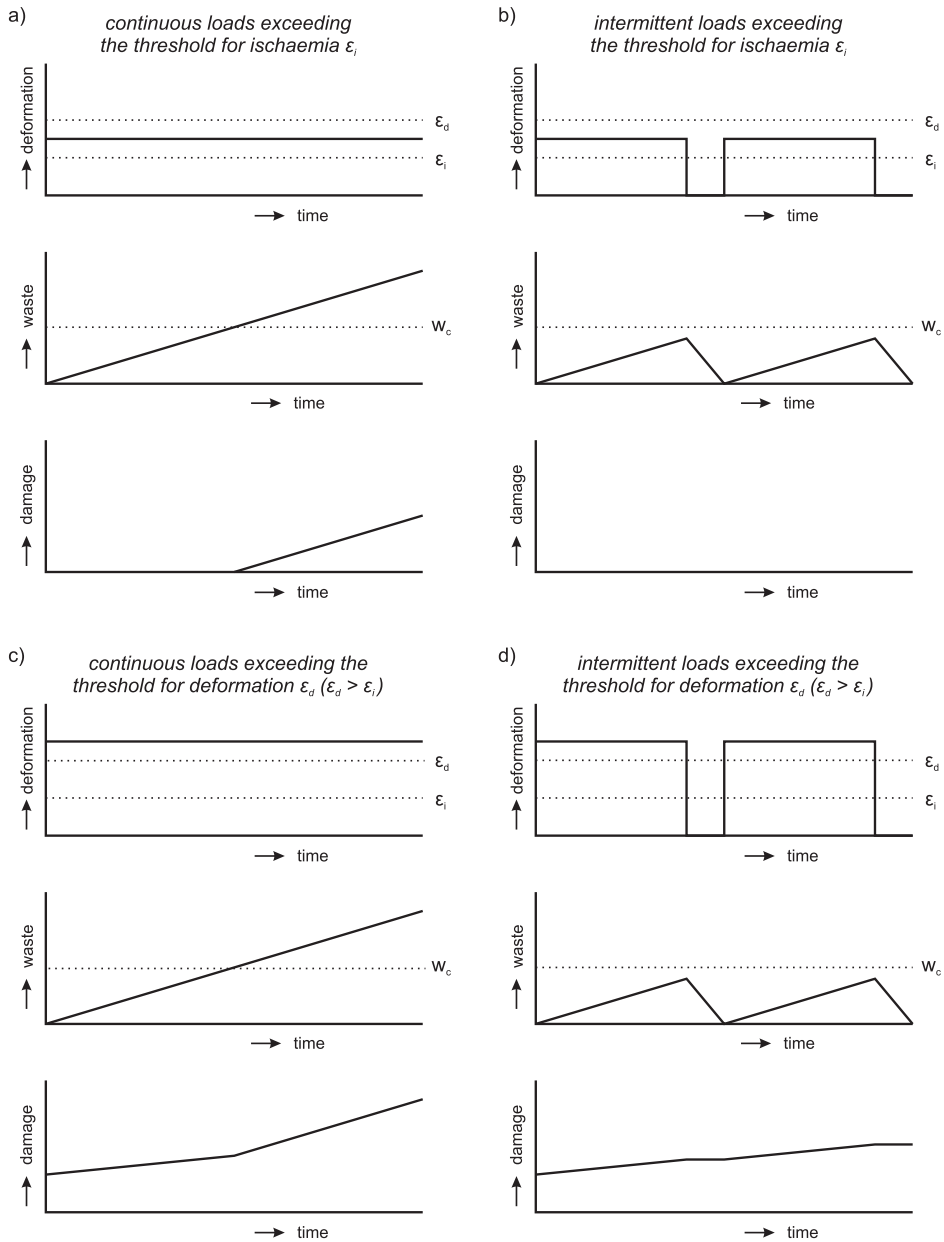
Figure 8.3: Schematic representation of the development of tissue damage resulting from four different loading conditions. a) Deformations exceeding threshold ϵ_i will lead to ischaemia, which will lead to tissue damage once a critical threshold w_c is exceeded. b) Intermittent load reliefs may prevent tissue damage when deformations only exceed threshold ϵ_i. c) Larger deformations that also exceed threshold ϵ_d will lead to tissue damage induced by deformation, and also by ischaemia if threshold w_c is exceeded. d) Intermittent load reliefs cannot prevent deformation-induced damage caused by deformations exceeding threshold ϵ_d.

In case of large continuous mechanical loads with deformations exceeding threshold ϵ_d, tissue damage will develop directly due to deformation and is subsequently aggravated by ischaemia (figure 8.3c). Indeed, the combined effects of deformation and ischaemia may even be more harmful than their individual contributions. Intermittent pressure reliefs for these loads are still beneficial to prevent ischaemia-related damage. However, the deformation-induced damage cannot be prevented (figure 8.3d). For clinical practice, these results imply that large deformations exceeding threshold ϵ_d should be prevented. Most probably, deformations as experienced in clinical settings will always exceed threshold ϵ_i and, therefore, it is important to use intermittent load reliefs to prevent tissue damage due to ischaemia. It is worthy of note that in the healthy state any tissue damage will usually be repaired. This effect is not included in figure 8.3, but it will certainly play an important role in pressure ulcer development.

8.3.4   Early detection of DTI

It is essential to develop a screening method for the early detection of DTI to improve the efficacy of healing, prevent complications, and reduce the financial and manpower burdens associated with treatment. In the present thesis, the appropriateness of using biochemical markers of muscle damage for this aim was investigated. The baseline plasma variations of a number of markers were investigated in small groups of able-bodied and SCI subjects, and in one SCI subject with a pressure ulcer (chapter 7). In this study, creatine kinase (CK), myoglobin (Mb), and heart fatty acid binding protein (H-FABP) were investigated as markers for skeletal muscle damage, and C-reactive protein (CRP) was included as an inflammatory marker. Subsequently, in a pilot study with an animal model for DTI, the marker levels of Mb and H-FABP after 6 h mechanical loading were investigated in serum and urine (appendix A).

The results of chapter 7 indicated that the intra-subject variations in marker levels were smaller than the inter-subject variations, indicating that each subject had a unique marker profile. Since the variations in marker concentrations were smaller than those reported due to the presence of either myocardial infarction or pressure ulcers, it is predicted that this combination of markers may prove appropriate for the early detection of DTI. The results of the animal study described in appendix A showed the presence of large increases in Mb levels in both serum and urine after muscle damage. Increased Mb concentrations were present up to 12 h after load removal, and were particularly marked in urine. For H-FABP, much smaller increases were evident. Therefore, Mb appeared to be a more sensitive marker for skeletal muscle damage induced by mechanical loading than H-FABP. For clinical practice, the observation of increased Mb concentrations in urine implies that a noninvasive screening method may be developed for the early

detection of DTI. Such a noninvasive method based on biomarker levels in urine would present a smaller burden for susceptible individuals than a method that includes blood sampling, in particular for subjects at high risk of DTI for which daily sampling may be necessary. Moreover, urine collection would also be easier for catheterised SCI subjects.

8.4   Recommendations for future research

In the present thesis, it was demonstrated that deformation is the primary trigger for muscle damage within short loading periods once a specific deformation threshold is exceeded (chapter 3). An estimation of the internal deformations in the buttocks in a porcine model for DTI indicated that the internal strains may be large in both the muscle and the fat layer (chapter 6). Therefore, the damage mechanisms of fat should be investigated as well to better understand the aetiology of DTI. In particular, it would be interesting to identify a deformation threshold for fat tissue, and investigate how this compares to the threshold of muscle tissue.

It was shown that a change in mechanical properties of muscle tissue can have a large influence on the internal tissue deformations (chapter 6). To date, there is a lack of data concerning these changes in mechanical properties associated with pathologies. For future research, it may therefore be interesting to monitor tissue properties in individuals with SCI, e.g. with MR or ultrasound elastography, to determine the changes in stiffness of the tissues and investigate to what extent these changes increase the risk of DTI. Furthermore, a better knowledge of the change in mechanical properties due to the presence of tissue damage can help to investigate the mechanical factors associated with the progression of existing tissue damage.

The aetiology of DTI was studied using healthy laboratory animals. The critical thresholds for deformation and ischaemia that will lead to tissue damage may be different for other animal species or humans. Moreover, these thresholds may vary between individuals and also for a specific individual in time. These variations are probably due to the presence of pathologies that change tissue properties, the circulation, and the immune system. For future research, it is therefore important to investigate the aetiology in animal models with specific pathologies, such as SCI or diabetes, to identify risk factors associated with the development of DTI. For example, both able-bodied and SCI animals were included in a study on the effects of electrical stimulation on the internal deformations in the buttocks (Solis et al., 2011b,c).

The results of appendix A demonstrated a clear increase in Mb concentrations in the blood and urine of Sprague-Dawley rats after mechanical loading. However, due to some limitations regarding the load application, a correlation between the amount of muscle damage and the release of biomarker could not be established or rejected. It would be interesting to perform new experiments with Sprague-Dawley rats to investigate the nature of this correlation. For this, an experimental setup comparable to the one used in chapters 2-5 should be used, which enables accurate monitoring of the applied load and the subsequent development of tissue damage. Furthermore, since biomarker concentrations in the circulation are determined by both the release from the injured tissue and the clearance by the kidneys, kinetic models may be used to estimate the release of markers from the injured tissue (appendix B).

8.5   Concluding remarks

In conclusion, the following results were obtained in this thesis:

- Deformation is the primary trigger for skeletal muscle damage for loading periods up to 2 h, either when applied continuously or superimposed with short periods of load relief. High deformations, such as present when individuals are positioned on hard surfaces such as stretchers and operating tables, should be prevented in order to reduce the risk of DTI.

- Changes in mechanical properties of muscle tissue after SCI may have a large influence on the internal tissue deformations.

- During prolonged loading, the damage development of skeletal muscle is determined by deformation, ischaemia, and reperfusion, each exhibiting a unique time profile. For long loading periods, it is predicted that ischaemia and its subsequent reperfusion will eventually become more important for the damage evolution than deformation.

- The baseline plasma variations of CK, Mb, H-FABP, and CRP in able-bodied and SCI subjects were small compared to the expected increase in biomarker concentrations during the development of DTI. This combination of markers may, therefore, prove appropriate for the early detection of DTI.

- After 6 h mechanical loading in an animal model, a considerable increase in Mb concentrations was observed in blood and urine. In particular, the Mb concentrations in urine exceeded those in blood, which indicates that a noninvasive screening method may be developed for the early detection of DTI.

Bibliography

J. E. Adams, D. R. Abendschein, and A. S. Jaffe. Biochemical markers of myocardial injury. Is MB creatine kinase the choice for the 1990s? *Circulation*, 88(2):750–763, 1993.

A. K. Akobeng. Understanding diagnostic tests 3: receiver operating characteristic curves. *Acta Paediatr.*, 96(5):644–647, 2007.

N. Al-Saadi, E. Nagel, M. Gross, A. Bornstedt, B. Schnackenburg, C. Klein, W. Klimek, H. Oswald, and E. Fleck. Noninvasive detection of myocardial ischemia from perfusion reserve based on cardiovascular magnetic resonance. *Circulation*, 101(12):1379–1383, 2000.

M. A. Ankrom, R. G. Bennett, S. Sprigle, D. Langemo, J. M. Black, D. R. Berlowitz, C. H. Lyder, and National Pressure Ulcer Advisory Panel. Pressure-related deep tissue injury under intact skin and the current pressure ulcer staging systems. *Adv. Skin Wound Care*, 18(1):35–42, 2005.

F. S. Apple, M. A. Rogers, W. M. Sherman, D. L. Costill, F. C. Hagerman, and J. L. Ivy. Profile of creatine kinase isoenzymes in skeletal muscles of marathon runners. *Clin. Chem.*, 30(3):413–416, 1984.

R. B. Armstrong and R. O. Phelps. Muscle fiber type composition of the rat hindlimb. *Am. J. Anat.*, 171(3):259–272, 1984.

D. L. Bader and S. H. White. The viability of soft tissues in elderly subjects undergoing hip surgery. *Age Ageing*, 27(2):217–221, 1998.

J. R. Basford, T. R. Jenkyn, K. N. An, R. L. Ehman, G. Heers, and K. R. Kaufman. Evaluation of healthy and diseased muscle with magnetic resonance elastography. *Arch. Phys. Med. Rehabil.*, 83(11):1530–1536, 2002.

B. M. Bates-Jensen, M. Guihan, S. L. Garber, A. S. Chin, and S. P. Burns. Characteristics of recurrent pressure ulcers in veterans with spinal cord injury. *J. Spinal Cord Med.*, 32 (1):34–42, 2009.

G. Bennett, C. Dealey, and J. Posnett. The cost of pressure ulcers in the UK. *Age Ageing*, 33(3):230–235, 2004.

S. Beraldo and S. R. Dodds. Lower limb acute compartment syndrome after colorectal surgery in prolonged lithotomy position. *Dis. Colon Rectum*, 49(11):1772–1780, 2006.

J. Black, M. Baharestani, J. Cuddigan, B. Dorner, L. Edsberg, D. Langemo, M.E. Posthauer, C. Ratliff, G. Taler, and NPUAP. National Pressure Ulcer Advisory Panel's updated pressure ulcer staging system. *Dermatol. Nurs.*, 19(4):343–349, 2007.

F. W. Blaisdell. The pathophysiology of skeletal muscle ischemia and the reperfusion syndrome: a review. *Cardiovasc. Surg.*, 10(6):620–630, 2002.

M. R. Bliss. Aetiology of pressure sores. *Rev. Clin. Gerontol.*, 3:379–397, 1993.

N. P. Blockley, L. Jiang, A. G. Gardener, C. N. Ludman, S. T. Francis, and P. A. Gowland. Field strength dependence of R_1 and R_2^* relaxivities of human whole blood to Pro-Hance, Vasovist, and deoxyhemoglobin. *Magn. Reson. Med.*, 60(6):1313–1320, 2008.

K. M. Bogie, X. Wang, and R. J. Triolo. Long-term prevention of pressure ulcers in high-risk patients: a single case-study of the use of gluteal neuromuscular electric stimulation. *Arch. Phys. Med. Rehabil.*, 87(4):585–591, 2006.

E. M. H. Bosboom, M. K. C. Hesselink, C. W. J. Oomens, C. V. C. Bouten, M. R. Drost, and F. P. T. Baaijens. Passive transverse mechanical properties of skeletal muscle under in vivo compression. *J. Biomech.*, 34(10):1365–1368, 2001.

E. M. H. Bosboom, C. V. C. Bouten, C. W. J. Oomens, F. P. T. Baaijens, and K. Nicolay. Quantifying pressure sore-related muscle damage using high-resolution MRI. *J. Appl. Physiol.*, 95(6):2235–2240, 2003.

G. J. Bours, R. J. Halfens, H. H. Abu-Saad, and R. T. Grol. Prevalence, prevention, and treatment of pressure ulcers: descriptive study in 89 institutions in the netherlands. *Res. Nurs. Health*, 25(2):99–110, 2002.

C. V. C. Bouten, M. M. Knight, D. A. Lee, and D. L. Bader. Compressive deformation and damage of muscle cell subpopulations in a model system. *Ann. Biomed. Eng.*, 29(2): 153–163, 2001.

C. V. Bouten, C. W. Oomens, F. P. Baaijens, and D. L. Bader. The etiology of pressure ulcers: skin deep or muscle bound? *Arch. Phys. Med. Rehabil.*, 84(4):616–619, 2003.

P. Brancaccio, N. Maffulli, and F. M. Limongelli. Creatine kinase monitoring in sports medicine. *Br. Med. Bull.*, 81-82(1):209–230, 2007.

H. Brem, J. Maggi, D. Nierman, L. Rolnitzky, D. Bell, R. Rennert, M. Golinko, A. Yan, C. Lyder, and B. Vladeck. High cost of stage IV pressure ulcers. *Am. J. Surg.*, 200(4): 473–477, 2010.

R. G. M. Breuls, C. V. C. Bouten, C. W. J. Oomens, D. L. Bader, and F. P. T. Baaijens. Compression induced cell damage in engineered muscle tissue: an in vitro model to study pressure ulcer aetiology. *Ann. Biomed. Eng.*, 31(11):1357–1364, 2003.

E. M. Carmo-Araújo, M. Dal-Pai-Silva, V. Dal-Pai, R. Cecchini, and A. L. Anjos Ferreira. Ischaemia and reperfusion effects on skeletal muscle tissue: morphological and histochemical studies. *Int. J. Exp. Pathol.*, 88(3):147–154, 2007.

K. K. Ceelen, A. Stekelenburg, J. L. J. Mulders, G. J. Strijkers, F. P. T. Baaijens, K. Nicolay, and C. W. J. Oomens. Validation of a numerical model of skeletal muscle compression with MR tagging: a contribution to pressure ulcer research. *J. Biomech. Eng.*, 130(6): 061015, 2008a.

K. K. Ceelen, A. Stekelenburg, S. Loerakker, G. J. Strijkers, D. L. Bader, K. Nicolay, F. P. T. Baaijens, and C. W. J. Oomens. Compression-induced damage and internal tissue strains are related. *J. Biomech.*, 41(16):3399–3404, 2008b.

R. K. Chan, W. G. Austen Jr, S. Ibrahim, G. Y. Ding, N. Verna, H. B. Hechtman, and F. D. Moore Jr. Reperfusion injury to skeletal muscle affects primarily type II muscle fibers. *J. Surg. Res.*, 122(1):54–60, 2004.

Y. Chen, M. J. DeVivo, and A. B. Jackson. Pressure ulcer prevalence in people with spinal cord injury: age-period-duration effects. *Arch. Phys. Med. Rehabil.*, 86(6):1208–1213, 2005.

W. W. Chow and E. I. Odell. Deformations and stresses in soft body tissues of a sitting person. *J. Biomech. Eng.*, 100(2):79–87, 1978.

P. M. Clarkson and M. J. Hubal. Exercise-induced muscle damage in humans. *Am. J. Phys. Med. Rehabil.*, 81(11 Suppl.):S52–S69, 2002.

A. Clerico, M. G. Del Chicca, O. Giampietro, M. Fantoni, and A. Boldrini. Factors affecting serum myoglobin levels in normal population. *Ric. Clin. Lab.*, 14(3):541–444, 1984.

M. J. Coggrave and L. S. Rose. A specialist seating assessment clinic: changing pressure relief practice. *Spinal Cord*, 41(12):692–695, 2003.

C. A. Curtis, S. L. Chong, I. Kornelsen, R. R. Uwiera, P. Seres, and V. K. Mushahwar. The effects of intermittent electrical stimulation on the prevention of deep tissue injury: varying loads and stimulation paradigms. *Artif. Organs*, 35(3):226–236, 2011.

P. A. Dabnichki, A. D. Crocombe, and S. C. Hughes. Deformation and stress analysis of supported buttock contact. *Proc Intstn Mech Engnrs - Part H, J Eng Med*, 208(1):9–17, 1994.

R. K. Daniel, D. L. Priest, and D. C. Wheatley. Etiologic factors in pressure sores: an experimental model. *Arch. Phys. Med. Rehabil.*, 62(10):492–498, 1981.

A. L. Davies, K. C. Hayes, and G. A. Dekaban. Clinical correlates of elevated serum concentrations of cytokines and autoantibodies in patients with spinal cord injury. *Arch. Phys. Med. Rehabil.*, 88(11):1384–1393, 2007.

S. M. Dinsdale. Decubitus ulcers: role of pressure and friction in causation. *Arch Phys Med Rehabil*, 55(4):147–152, 1974.

J. J. Elsner and A. Gefen. Is obesity a risk factor for deep tissue injury in patients with spinal cord injury? *J. Biomech.*, 41(16):3322–3331, 2008.

W. J. Evans, C. N. Meredith, J. G. Cannon, C. A. Dinarello, W. R. Frontera, V. A. Hughes, B. H. Jones, and H. G. Knuttgen. Metabolic changes following eccentric exercise in trained and untrained men. *J. Appl. Physiol.*, 61(5):1864–1868, 1986.

J. L. Fleckenstein. Skeletal muscle evaluated by MRI. In D. M. Grant and R. K. Harris, editors, *In: Encyclopedia of nuclear magnetic resonance*. John Wiley & Sons, 1996.

F. Frost, M.J. Roach, I. Kushner, and P. Schreiber. Inflammatory C-reactive protein and cytokine levels in asymptomatic people with chronic spinal cord injury. *Arch. Phys. Med. Rehabil.*, 86(2):312–317, 2005.

S. L. Garber, D. H. Rintala, K. A. Hart, and M. J. Fuhrer. Pressure ulcer risk in spinal cord injury: predictors of ulcer status over 3 years. *Arch. Phys. Med. Rehabil.*, 81(4):465–471, 2000.

S. L. Garber and D. H. Rintala. Pressure ulcers in veterans with spinal cord injury: a retrospective study. *J. Rehabil. Res. Dev.*, 40(5):433–441, 2003.

D. Gawlitta, W. Li, C. W. J. Oomens, F. P. T. Baaijens, D. L. Bader, and C. V. C. Bouten. The relative contributions of compression and hypoxia to development of muscle tissue damage: an in vitro study. *Ann. Biomed. Eng*, 35(2):273–284, 2007a.

D. Gawlitta, C. W. J. Oomens, D. L. Bader, F. P. T. Baaijens, and C. V. C. Bouten. Temporal differences in the influence of ischemic factors and deformation on the metabolism of engineered skeletal muscle. *J. Appl. Physiol*, 103(2):464–473, 2007b.

M. Geerligs, G. W. M. Peters, P. A. J. Ackermans, C. W. J. Oomens, and F. P. T. Baaijens. Linear viscoelastic behavior of subcutaneous adipose tissue. *Biorheology*, 45(6):677–688, 2008.

M. G. D. Geers, R. de Borst, and W. A. M. Brekelmans. Computing strain fields from discrete displacement fields in 2D solids. *Int. J. Solids Structures*, 33(29):4293–4307, 1996.

A. Gefen, N. Gefen, and E. Linder-Ganz. In vivo muscle stiffening under bone compression promotes deep pressure sores. *J. Biomech. Eng.*, 127(3):512–524, 2005.

A. Gefen and J. Levine. The false premise in measuring body-support interface pressures for preventing serious pressure ulcers. *J. Med. Eng. Technol.*, 31(5):375–380, 2007.

A. Gefen, B. van Nierop, D. L. Bader, and C. W. Oomens. Strain-time cell-death threshold for skeletal muscle in a tissue-engineered model system for deep tissue injury. *J. Biomech.*, 41(9):2003–2012, 2008.

A. Gefen. Reswick and Rogers pressure-time curve for pressure ulcer risk. Part 2. *Nurs. Stand.*, 23(46):40–44, 2009.

J. F. C. Glatz, G. J. van der Vusse, M. L. Simoons, J. A. Kragten, M. P. van Dieijen-Visser, and W. T. Hermens. Fatty acid-binding protein and the early detection of acute myocardial infarction. *Clin. Chim. Acta*, 272(1):87–92, 1998.

K. E. Groth. *Klinische Beobachtungen und experimentelle Studien über die Entstehung des Dekubitus.* 1942.

S. Gyawali, L. Solis, S. L. Chong, C. Curtis, P. Seres, I. Kornelsen, R. Thompson, and V. K. Mushahwar. Intermittent electrical stimulation redistributes pressure and promotes tissue oxygenation in loaded muscles of individuals with spinal cord injury. *J. Appl. Physiol.*, 110(1):246–255, 2011.

E. M. Haacke, C. L. Filleti, R. Gattu, C. Ciulla, A. Al-Bashir, K. Suryanarayanan, M. Li, Z. Latif, Z. DelProposto, V. Sehgal, T. Li, V. Torquato, R. Kanaparti, J. Jiang, and J. Neelavalli. New algorithm for quantifying vascular changes in dynamic contrast-enhanced MRI independent of absolute T_1 values. *Magn. Reson. Med.*, 58(3):463–472, 2007.

S. Hagisawa, M. W. Ferguson-Pell, V. R. Palmieri, and G. V. Cochran. Pressure sores: a biochemical test for early detection of tissue damage. *Arch. Phys. Med. Rehabil.*, 69(9):668–671, 1988.

M. Hashimoto, T. Kurose, and S. Kawamata. Comparison between a weight compression and a magnet compression for experimental pressure ulcers in the rat. Histological studies and effects of anesthesia. *Arch. Histol. Cytol.*, 71(5):303–316, 2008.

M. Hatoko, A. Tanaka, M. Kuwahara, S. Yurugi, H. Iioka, and K. Niitsuma. Difference of molecular response to ischemia-reperfusion of rat skeletal muscle as a function of ischemic time: study of the expression of p53, p21^{WAF-1}, Bax protein, and apoptosis. *Ann. Plast. Surg.*, 48(1):68–74, 2002.

F. M. Hendriks, D. Brokken, J. T. W. M. van Eemeren, C. W. J. Oomens, F. P. T. Baaijens, and J. B. A. M. Horsten. A numerical-experimental method to characterize the non-linear mechanical behaviour of human skin. *Skin Res. Technol.*, 9(3):274–283, 2003.

R. C. Hibbeler. *Engineering mechanics: statics.* Prentice-Hall, London, 2001.

D. A. Hobson. Comparative effects of posture on pressure and shear at the body-seat interface. *J. Rehabil. Res. Dev.*, 29(4):21–31, 1992.

D. W. Hosmer and S. Lemeshow. *Applied logistic regression.* John Wiley & Sons, 2nd edition, 2000.

T. Husain. An experimental study of some pressure effects on tissues, with reference to the bed-sore problem. *J. Pathol. Bacteriol.*, 66(2):347–358, 1953.

M. Jerosch-Herold, R. T. Seethamraju, C. M. Swingen, N. M. Wilke, and A. E. Stillman. Analysis of myocardial perfusion MRI. *J. Magn. Reson. Imaging*, 19(6):758–770, 2004.

M. Kosiak. Etiology and pathology of ischemic ulcers. *Arch. Phys. Med. Rehabil.*, 40(2): 62–69, 1959.

J. Kottner, T. Dassen, and N. Lahmann. Prevalence of deep tissue injuries in hospitals and nursing homes: two cross-sectional studies. *Int. J. Nurs. Stud.*, 47(6):665–670, 2010.

D. L. Kraitchman, N. Wilke, E. Hexeberg, M. Jerosch-Herold, Y. Wang, T. B. Parrish, C. N. Chang, Y. Zhang, R. J. Bache, and L. Axel. Myocardial perfusion and function in dogs with moderate coronary stenosis. *Magn. Reson. Med.*, 35(5):771–780, 1996.

T. A. Krouskop, N. P. Reddy, W. A. Spencer, and J. W. Secor. Mechanisms of decubitus ulcer formation – an hypothesis. *Med. Hypotheses*, 4(1):37–39, 1978.

S. A. Kruse, J. A. Smith, A. J. Lawrence, M. A. Dresner, A. Manduca, J. F. Greenleaf, and R. L. Ehman. Tissue characterization using magnetic resonance elastography: preliminary results. *Phys. Med. Biol.*, 45(6):1579–1590, 2000.

H. Kuipers. Exercise-induced muscle damage. *Int. J. Sports Med.*, 15(3):132–135, 1994.

S. Laurent, L. Vander Elst, and R. N. Muller. Comparative study of the physicochemical properties of six clinical low molecular weight gadolinium contrast agents. *Contrast Media Mol. Imaging*, 1(3):128–137, 2006.

C. Lavini, M. C. de Jonge, M. G. van de Sande, P. P. Tak, A. J. Nederveen, and M. Maas. Pixel-by-pixel analysis of DCE-MRI curve patterns and an illustration of its application to the imaging of the musculoskeletal system. *Magn. Reson. Imaging*, 25(5):604–612, 2007.

S. P. Levine, R. L. Kett, P. S. Cederna, and S. V. Brooks. Electric muscle stimulation for pressure sore prevention: tissue shape variation. *Arch. Phys. Med. Rehabil.*, 71(3): 210–215, 1990a.

S. P. Levine, R. L. Kett, M. D. Gross, B. A. Wilson, P. S. Cederna, and J. E. Juni. Blood flow in the gluteus maximus of seated individuals during electrical muscle stimulation. *Arch. Phys. Med. Rehabil.*, 71(9):682–686, 1990b.

F. Lin, A. Pandya, A. Cichowski, M. Modi, B. Reprogle, D. Lee, N. Kadono, and M. Makhsous. Deep tissue injury model for pressure ulcer research on spinal cord injury. *J. Tissue Viability*, 19(2):67–76, 2010.

E. Linder-Ganz and A. Gefen. Mechanical compression-induced pressure sores in rat hindlimb: muscle stiffness, histology, and computational models. *J. Appl. Physiol*, 96 (6):2034–2049, 2004.

E. Linder-Ganz, S. Engelberg, M. Scheinowitz, and A. Gefen. Pressure-time cell death threshold for albino rat skeletal muscles as related to pressure sore biomechanics. *J. Biomech.*, 39(14):2725–2732, 2006.

E. Linder-Ganz, N. Shabshin, Y. Itzchak, and A. Gefen. Assessment of mechanical conditions in sub-dermal tissues during sitting: a combined experimental-MRI and finite element approach. *J. Biomech.*, 40(7):1443–1454, 2007.

E. Linder-Ganz, N. Shabshin, Y. Itzchak, Z. Yizhar, I. Siev-Ner, and A. Gefen. Strains and stresses in sub-dermal tissues of the buttocks are greater in paraplegics than in healthy during sitting. *J. Biomech.*, 41(3):567–580, 2008.

M. Liu, P. Bose, G. A. Walter, F. J. Thompson, and K. Vandenborne. A longitudinal study of skeletal muscle following spinal cord injury and locomotor training. *Spinal Cord*, 46 (7):488–493, 2008.

S. Loerakker, A. Stekelenburg, G. J. Strijkers, J. J. M. Rijpkema, F. P. T. Baaijens, D. L. Bader, K. Nicolay, and C. W. J. Oomens. Temporal effects of mechanical loading on deformation-induced damage in skeletal muscle. *Ann. Biomed. Eng.*, 38(8):2577–2587, 2010.

S. Loerakker, C. W. J. Oomens, E. Manders, T. Schakel, D. L. Bader, F. P. T. Baaijens, K. Nicolay, and G. J. Strijkers. Ischemia-reperfusion injury in rat skeletal muscle assessed with T_2-weighted and dynamic contrast-enhanced MRI. *Magn. Reson. Med.*, 2011. doi: 10.1002/mrm.22801.

N. Logothetis and H. P. Wynn. *Quality through design: experimental design, off-line quality control and Taguchi's contributions.* Clarendon Press, Oxford, 1989.

A. van Londen, M. Herwegh, C. H. van der Zee, A. Daffertshofer, C. A. Smit, A. Niezen, and T. W. Janssen. The effect of surface electric stimulation of the gluteal muscles on the interface pressure in seated people with spinal cord injury. *Arch. Phys. Med. Rehabil.*, 89(9):1724–1732, 2008.

M. van Loocke, C. G. Lyons, and C. K. Simms. Viscoelastic properties of passive skeletal muscle in compression: stress-relaxation behaviour and constitutive modelling. *J. Biomech.*, 41(7):1555–1566, 2008.

Y. Luo, K. M. Mohning, V. P. Hradil, J. L. Wessale, J. A. Segreti, M. E. Nuss, C. D. Wegner, S. E. Burke, and B. F. Cox. Evaluation of tissue perfusion in a rat model of hind-limb muscle ischemia using dynamic contrast-enhanced magnetic resonance imaging. *J. Magn. Reson. Imaging*, 16(3):277–283, 2002.

A. F. Mak, M. Zhang, and E. W. Tam. Biomechanics of pressure ulcer in body tissues interacting with external forces during locomotion. *Annu. Rev. Biomed. Eng.*, 12:29–53, 2010.

M. Makhsous, M. Priebe, J. Bankard, D. Rowles, M. Zeigler, D. Chen, and F. Lin. Measuring tissue perfusion during pressure relief maneuvers: insights into preventing pressure ulcers. *J. Spinal Cord Med.*, 30(5):497–507, 2007.

Y. K. Mariappan, K. J. Glaser, and R. L. Ehman. Magnetic resonance elastography: a review. *Clin. Anat.*, 23(5):497–511, 2010.

R. J. Marino, T. Barros, F. Biering-Sorensen, S. P. Burns, W. H. Donovan, D. E. Graves, M. Haak, L. M. Hudson, M. M. Priebe, and ASIA Neurological Standards Committee 2002. International standards for neurological classification of spinal cord injury. *J. Spinal Cord Med.*, 26 Suppl 1:S50–S56, 2003.

J. M. McCord. Oxygen-derived free radicals in postischemic tissue injury. *N. Engl. J. Med.*, 312(3):159–163, 1985.

W. O. McKinley, A. B. Jackson, D. D. Cardenas, and M. J. DeVivo. Long-term medical complications after traumatic spinal cord injury: a regional model systems analysis. *Arch. Phys. Med. Rehabil.*, 80(11):1402–1410, 1999.

M. P. Miles, J. M. Andring, S. D. Pearson, L. K. Gordon, C. Kasper, C. M. Depner, and J. R. Kidd. Diurnal variation, response to eccentric exercise, and association of inflammatory mediators with muscle damage variables. *J. Appl. Physiol.*, 104(2):451–458, 2008.

G. E. Miller and J. Seale. Lymphatic clearance during compressive loading. *Lymphology*, 14(4):161–166, 1981.

T. Minematsu, G. Nakagami, Y. Sari, T. Akase, J. Sugama, T. Nagase, and H. Sanada. Candidate biomarkers for deep tissue damage from molecular biological and biochemical aspects. *J. Tissue Viability*, 19(2):77–83, 2010.

S. Morikawa, C. Kido, and T. Inubushi. Observation of rat hind limb skeletal muscle during arterial occlusion and reperfusion by ^{31}P MRS and ^{1}H MRI. *Magn. Reson. Imaging*, 9(3):269–274, 1991.

L. R. Morse, K. Stolzmann, H. P. Nguyen, N. B. Jain, C. Zayac, D. R. Gagnon, C. G. Tun, and E. Garshick. Association between mobility mode and C-reactive protein levels in men with chronic spinal cord injury. *Arch. Phys. Med. Rehabil.*, 89(4):726–731, 2008.

T. Nagel, S. Loerakker, and C. W. J. Oomens. A theoretical model to study the effects of cellular stiffening on the damage evolution in deep tissue injury. *Comput. Methods Biomech. Biomed. Engin.*, 12(5):585–597, 2009.

O. W. Neumark. Deformation, not pressure, is the prime cause of pressure sores. *Care. Sci. Pract.*, 1:41–43, 1981.

F. A. van Nieuwenhoven, A. H. Kleine, K. W. H. Wodzig, W. T. Hermens, H. A. Kragten, J. G. Maessen, C. D. Punt, M. P. Van Dieijen, G. J. Van der Vusse, and J. F. C. Glatz. Discrimination between myocardial and skeletal muscle injury by assessment of the plasma ratio of myoglobin over fatty acid-binding protein. *Circulation*, 92(10):2848–2854, 1995.

G. T. Nola and L. M. Vistnes. Differential response of skin and muscle in the experimental production of pressure sores. *Plast. Reconstr. Surg.*, 66(5):728–733, 1980.

NPUAP and EPUAP. *Prevention and treatment of pressure ulcers: clinical practice guideline.* Washington DC: National Pressure Ulcer Advisory Panel, 2009.

R. W. Ogden. Large deformation isotropic elasticity – on the correlation of theory and experiment for incompressible rubberlike solids. *Proc. R. Soc. Lond. A*, 326(1567):565–584, 1972.

R. W. Ogden, G. Saccomandi, and I. Sgura. Fitting hyperelastic models to experimental data. *Computational Mechanics*, 34(6):484–502, 2004.

C. W. J. Oomens, O. F. J. T. Bressers, E. M. H. Bosboom, C. V. C. Bouten, and D. L. Bader. Can loaded interface characteristics influence strain distributions in muscle adjacent to bony prominences? *Comput. Methods Biomech. Biomed. Engin.*, 6(3):171–180, 2003.

C. W. J. Oomens, S. Loerakker, and D. L. Bader. The importance of internal strain as opposed to interface pressure in the prevention of pressure related deep tissue injury. *J. Tissue Viability*, 19(2):35–42, 2010.

K. J. Parker, M. M. Doyley, and D. J. Rubens. Imaging the elastic properties of tissue: the 20 year perspective. *Phys. Med. Biol.*, 56(1):R1–R29, 2011.

S. M. Peirce, T. C. Skalak, and G. T. Rodeheaver. Ischemia-reperfusion injury in chronic pressure ulcer formation: a skin model in the rat. *Wound Repair Regen.*, 8(1):68–76, 2000.

M. M. A. L. Pelsers, J. P. Chapelle, M. Knapen, C. Vermeer, A. M. M. Muijtjens, W. T. Hermens, and J. F. C. Glatz. Influence of age and sex and day-to-day and within-day biological variation on plasma concentrations of fatty acid-binding protein and myoglobin in healthy subjects. *Clin. Chem.*, 45(3):441–443, 1999.

M. B. Pepys and G. M. Hirschfield. C-reactive protein: a critical update. *J. Clin. Invest.*, 111(12):1805–1812, 2003.

A. Polliack, R. Taylor, and D. Bader. Analysis of sweat during soft tissue breakdown following pressure ischaemia. *J. Rehabil. Res. Dev.*, 30(2):250–259, 1993.

A. Polliack, R. Taylor, and D. Bader. Sweat analysis following pressure ischaemia in a group of debilitated subjects. *J. Rehabil. Res. Dev.*, 34(3):303–308, 1997.

R. J. Probst, J. M. Lim, D. N. Bird, G. L. Pole, A. K. Sato, and J. R. Claybaugh. Gender differences in the blood volume of conscious Sprague-Dawley rats. *J. Am. Assoc. Lab. Anim. Sci.*, 45(2):49–52, 2006.

L. M. Rappl. Physiological changes in tissues denervated by spinal cord injury tissues and possible effects on wound healing. *Int. Wound J.*, 5(3):435–444, 2008.

N. P. Reddy and G. V. Cochran. Interstitial fluid flow as a factor in decubitus ulcer formation. *J. Biomech.*, 14(12):879–881, 1981.

J. B. Reswick and J. E. Rogers. Experience at rancho los amigos hospital with devices and techniques that prevent pressure sores. In R. M. Kenedi and J. M. Cowden, editors, *Bedsore biomechanics*, pages 301–310. The Macmillan Press, 1st edition, 1976.

D. H. Rintala, S. L. Garber, J. D. Friedman, and S. A. Holmes. Preventing recurrent pressure ulcers in veterans with spinal cord injury: impact of a structured education and follow-up intervention. *Arch. Phys. Med. Rehabil.*, 89(8):1429–1441, 2008.

G. P. Rodriguez and J. Claus-Walker. Measurement of hydroxylysine glucosides in urine and its application to spinal cord injury. *J. Chromatogr.*, 308:65–73, 1984.

G. P. Rodriguez and J. Claus-Walker. Biochemical changes in skin composition in spinal cord injury: a possible contribution to decubitus ulcers. *Paraplegia*, 26(5):302–309, 1988.

G. P. Rodriguez and S. L. Garber. Prospective study of pressure ulcer risk in spinal cord injury patients. *Paraplegia*, 32(3):150–158, 1994.

B. Rosner. *Fundamentals of biostatistics*. Thomson Brooks/Cole, 6th edition, 2006.

B. B. Rubin, A. Romaschin, P. M. Walker, D. C. Gute, and R. J. Korthuis. Mechanisms of postischemic injury in skeletal muscle: intervention strategies. *J. Appl. Physiol.*, 80(2): 369–387, 1996.

E. Rubin, F. Gorstein, R. Rubin, R. Schwarting, and D. Strayer. *Rubin's pathology: clinico-pathologic foundations of medicine*. Lippincott Williams & Wilkins, 4th edition, 2005.

R. Salcido, J. C. Donofrio, S. B. Fisher, E. K. LeGrand, K. Dickey, J. M. Carney, R. Schosser, and R. Liang. Histopathology of pressure ulcers as a result of sequential computer-controlled pressure sessions in a fuzzy rat model. *Adv. Wound. Care*, 7(5):23–4, 26, 28, 1994.

Y. Sari, G. Nakagami, A. Kinoshita, L. Huang, K. Ueda, S. Iizaka, H. Sanada, and J. Sugama. Changes in serum and exudate creatine phosphokinase concentrations as an indicator of deep tissue injury: a pilot study. *Int. Wound J.*, 5(5):674–680, 2008.

R. Scelsi. Skeletal muscle pathology after spinal cord injury: our 20 year experience and results on skeletal muscle changes in paraplegics, related to functional rehabilitation. *Basic Appl. Myol.*, 11(2):75–85, 2001.

L. Schoonhoven, M. T. Bousema, E. Buskens, and prePURSE-study group. The prevalence and incidence of pressure ulcers in hospitalised patients in The Netherlands: a prospective inception cohort study. *Int. J. Nurs. Stud.*, 44(6):927–935, 2007.

G. Scivoletto, U. Fuoco, B. Morganti, E. Cosentino, and M. Molinari. Pressure sores and blood and serum dysmetabolism in spinal cord injury patients. *Spinal Cord*, 42(8): 473–476, 2004.

J. L. Segal, E. Gonzales, S. Yousefi, L. Jamshidipour, and S. R. Brunnemann. Circulating levels of IL-2R, ICAM-1, and IL-6 in spinal cord injuries. *Arch. Phys. Med. Rehabil.*, 78 (1):44–47, 1997.

N. Shabshin, G. Zoizner, A. Herman, V. Ougortsin, and A. Gefen. Use of weight-bearing MRI for evaluating wheelchair cushions based on interal soft-tissue deformations under ischial tuberosities. *J. Rehabil. Res. Dev.*, 47(1):31–42, 2010.

A. Singh, R. K. Singh Rathore, M. Haris, S. K. Verma, N. Husain, and R. K. Gupta. Improved bolus arrival time and arterial input function estimation for tracer kinetic analysis in DCE-MRI. *J. Magn. Reson. Imaging*, 29(1):166–176, 2009.

P. M. Siu, E. W. Tam, B. T. Teng, X. M. Pei, J. W. Ng, I. F. Benzie, and A. F. Mak. Muscle apoptosis is induced in pressure-induced deep tissue injury. *J. Appl. Physiol.*, 107(4): 1266–1275, 2009.

L. R. Solis, D. P. Hallihan, R. R. Uwiera, R. B. Thompson, E. D. Pehowich, and V. K. Mushahwar. Prevention of pressure-induced deep tissue injury using intermittent electrical stimulation. *J. Appl. Physiol.*, 102(5):1992–2001, 2007.

L. R. Solis, S. Gyawali, P. Seres, C. A. Curtis, S. L. Chong, R. B. Thompson, and V. K. Mushahwar. Effects of intermittent electrical stimulation on superficial pressure, tissue oxygenation, and discomfort levels for the prevention of deep tissue injury. *Ann. Biomed. Eng.*, 39(2):649–663, 2011a.

L. R. Solis, A. Liggins, P. Seres, R. Uwiera, N. Poppe, E. Pehohwich, R. B. Thompson, and V. K. Mushahwar. Distribution of internal pressure around bony prominences: implications to deep tissue injury and effectiveness of intermittent electrical stimulation. *Submitted*, 2011b.

L. R. Solis, A. Liggins, P. Seres, R. Uwiera, N. Poppe, E. Pehohwich, R. B. Thompson, and V. K. Mushahwar. Internal muscle strains as a result of external loading in deep tissue injury development. *Submitted*, 2011c.

R. Sopher, J. Nixon, C. Gorecki, and A. Gefen. Exposure to internal muscle tissue loads under the ischial tuberosities during sitting is elevated at abnormally high or low body mass indices. *J. Biomech.*, 43(2):280–286, 2010.

R. Sopher, J. Nixon, C. Gorecki, and A. Gefen. Effects of intramuscular fat infiltration, scarring, and spasticity on the risk of sitting-acquired deep tissue injury in spinal cord injury patients. *J. Biomech. Eng.*, 133(2):021011, 2011.

S. Sorichter, J. Mair, A. Koller, M. M. A. L. Pelsers, B. Puschendorf, and J. F. C. Glatz. Early assessment of exercise induced skeletal muscle injury using plasma fatty acid binding protein. *Br. J. Sports Med.*, 32(2):121–124, 1998.

S. Sorichter, B. Puschendorf, and J. Mair. Skeletal muscle injury induced by eccentric muscle action: muscle proteins as markers of muscle fiber injury. *Exerc. Immunol. Rev.*, 5:5–21, 1999.

B. Sotgia, R. Sciagrà, I. Olivotto, G. Casolo, L. Rega, I. Betti, A. Pupi, P. G. Camici, and F. Cecchi. Spatial relationship between coronary microvascular dysfunction and delayed contrast enhancement in patients with hypertrophic cardiomyopathy. *J. Nucl. Med.*, 49(7):1090–1096, 2008.

A. Stekelenburg, C. Oomens, and D. Bader. Compression-induced tissue damage: animal models. In D.L. Bader, C.V.C. Bouten, D. Colin, D. Colin, and C.W.J. Oomens, editors, *Pressure ulcer research; current and future perspectives.*, pages 187–204. Springer-Verlag, 2005.

A. Stekelenburg, C. W. J. Oomens, G. J. Strijkers, L. de Graaf, D. L. Bader, and K. Nicolay. A new MR-compatible loading device to study in-vivo muscle damage development in rats due to compressive loading. *Med. Eng. Phys.*, 28(4):331–338, 2006a.

A. Stekelenburg, C. W. J. Oomens, G. J. Strijkers, K. Nicolay, and D. L. Bader. Compression-induced deep tissue injury examined with magnetic resonance imaging and histology. *J. Appl. Physiol.*, 100(6):1946–1954, 2006b.

A. Stekelenburg, G. J. Strijkers, H. Parusel, D. L. Bader, K. Nicolay, and C. W. Oomens. Role of ischemia and deformation in the onset of compression-induced deep tissue injury: MRI-based studies in a rat model. *J. Appl. Physiol.*, 102(5):2002–2011, 2007.

A. Stekelenburg, D. Gawlitta, D. L. Bader, and C. W. J. Oomens. Deep tissue injury: how deep is our understanding? *Arch. Phys. Med. Rehabil.*, 89(7):1410–1413, 2008.

C. Then, J. Menger, G. Benderoth, M. Alizadeh, T. J. Vogl, F. Hübner, and G. Silber. A method for a mechanical characterisation of human gluteal tissue. *Technol. Health Care*, 15(6):385–398, 2007.

C. Then, J. Menger, T. J. Vogl, F. Hübner, and G. Silber. Mechanical gluteal soft tissue material parameter validation under complex tissue loading. *Technol. Health Care*, 17 (5-6):393–401, 2009.

D. R. Thomas. Prevention and treatment of pressure ulcers: What works? What doesn't? *Cleve. Clin. J. Med.*, 68(8):704–722, 2001.

R. B. Thompson, R. J. Aviles, A. Z. Faranesh, V. K. Raman, V. Wright, R. S. Balaban, E. R. McVeigh, and R. J. Lederman. Measurement of skeletal muscle perfusion during postischemic reactive hyperemia using contrast-enhanced MRI with a step-input function. *Magn. Reson. Med.*, 54(2):289–298, 2005.

B. A. Todd and J. G. Thacker. Three-dimensional computer model of the human buttocks, in vivo. *J. Rehabil. Res. Dev.*, 31(2):111–119, 1994.

P. S. Tofts, B. Berkowitz, and M. D. Schnall. Quantitative analysis of dynamic Gd-DTPA enhancement in breast tumors using a permeability model. *Magn. Reson. Med.*, 33(4): 564–568, 1995.

P. S. Tofts, G. Brix, D. L. Buckley, J. L. Evelhoch, E. Henderson, M. V. Knopp, H. B. Larsson, T. Y. Lee, N. A. Mayr, G. J. Parker, R. E. Port, J. Taylor, and R. M. Weisskoff.

Estimating kinetic parameters from dynamic contrast-enhanced T_1-weighted MRI of a diffusable tracer: standardized quantities and symbols. *J. Magn. Reson. Imaging*, 10(3): 223–232, 1999.

S. Tsuji, S. Ichioka, N. Sekiya, and T. Nakatsuka. Analysis of ischemia-reperfusion injury in a microcirculatory model of pressure ulcers. *Wound Repair Regen.*, 13(2):209–215, 2005.

S. Ünal, S. Ozmen, Y. DemIr, R. Yavuzer, O. LatIfoglu, K. Atabay, and M. Oguz. The effect of gradually increased blood flow on ischemia-reperfusion injury. *Ann. Plast. Surg.*, 47 (4):412–416, 2001.

J. R. Urbaniak, A. V. Seaber, and L. E. Chen. Assessment of ischemia and reperfusion injury. *Clin. Orthop. Relat. Res*, 334:30–36, 1997.

C. VanGilder, G. D. MacFarlane, P. Harrison, C. Lachenbruch, and S. Meyer. The demographics of suspected deep tissue injury in the United States: an analysis of the International Pressure Ulcer Prevalence Survey 2006-2009. *Adv. Skin Wound Care*, 23 (6):254–261, 2010.

P. G. A. Volders, M. M. Vork, J. F. C. Glatz, and J. F. M. Smits. Fatty acid binding proteinuria diagnoses myocardial infarction in the rat. *Mol. Chem. Biochem.*, 123(1-2): 185–190, 1993.

T. D. Wang, Y. H. Wang, T. S. Huang, T. C. Su, S. L. Pan, and S. Y. Chen. Circulating levels of markers of inflammation and endothelial activation are increased in men with chronic spinal cord injury. *J. Formos. Med. Assoc.*, 106(11):919–928, 2007.

T. E. Yankeelov and J. C. Gore. Dynamic contrast enhanced magnetic resonance imaging in oncology: theory, data acquisition, analysis, and examples. *Curr. Med. Imaging Rev.*, 3(2):91–107, 2009.

Appendix A

Suitability of myoglobin and heart-type fatty acid binding protein as early markers for deep tissue injury – a pilot study

A.1   Introduction

Deep tissue injury (DTI) is a specific form of pressure ulcer that starts in deep tissue layers, such as skeletal muscle, initially under intact skin (Ankrom et al., 2005; Black et al., 2007). DTI is hard to detect in an early stage due to this intact skin, and tissue damage can therefore often progress until it finally becomes visible when it reaches the skin. At that stage, extensive necrosis may be present, associated with poor healing and a range of complications (Thomas, 2001). It is important to detect DTI in an early stage, so that appropriate wound treatment strategies can be applied to prevent progression of DTI. It is hypothesised that early detection can be achieved by measuring concentrations of biochemical markers of skeletal muscle damage in blood or urine. Myoglobin (Mb) and heart-type fatty acid binding protein (H-FABP) are two relatively small proteins that are present in the cytoplasm of muscle fibres. In case of muscle damage, these proteins leak out of the cells into the circulation and are subsequently excreted by the kidneys. The benefit of measuring these small proteins is that their concentrations in blood and urine increase much more rapidly than other muscle damage markers such as creatine kinase. Furthermore, skeletal muscle damage can be distinguished from cardiac muscle damage by calculating the ratio of Mb over H-FABP, which is considerably higher in case of skeletal muscle damage (20-70) when compared to cardiac muscle damage ($\sim$5) (Van Nieuwenhoven et al., 1995).

The goal of this pilot study was to evaluate the suitability of Mb and H-FABP as early markers of DTI in blood and urine in an animal model for DTI. First, the kinetics of H-FABP were studied in rats using bolus injections. Secondly, the tibialis anterior (TA) muscle of rats was compressed for 6 h to induce muscle damage, where the amount of damage was assessed using magnetic resonance imaging (MRI). Serum and urine concentrations of Mb and H-FABP due to this injury were determined during 48 h after load removal.

A.2   Materials & Methods

A.2.1   Animal experiments

A previously developed animal model was used, as described in Lin et al. (2010). In total, ten 12-14 week old female Sprague-Dawley rats were used. Animals were housed under a normal light cycle at 23 °C with access to standard food and water ad libitum. In five animals, complete transection of the spinal cord at T10 was performed under anaesthesia

to create a spinal cord injury (SCI) condition. Additionally, in all animals a hemispheric implant was positioned at the bone-muscle interface between the tibia and the TA muscle to simulate the presence of a bony prominence (Lin et al., 2010). Bolus injection and compression experiments were performed at least six weeks after SCI surgery and two weeks after implant surgery. All procedures were approved by the Institutional Animal Care and Use Committee of Northwestern University.

Blood and urine samples were collected under anaesthesia (1-2 % isoflurane mixed with oxygen) in uncoated micro-tubes before and after the experiments. Blood was collected in 150-200 μL samples from the tail vein using a 26.5 gauge needle. The loss in blood volume due to the sample collection was compensated for by injecting a similar volume of sterile saline into the tail vein. Urine was collected by manual bladder expression or by using a catheter. Thirty minutes after sample collection, the blood and urine samples were centrifuged for 12 min at 7200 rpm, after which the serum was obtained from the blood samples. Serum and urine samples were stored at -20 °C until analysed. The concentration of Mb and H-FABP in the serum and urine samples was determined using solid phase enzyme-linked immunosorbent assays (ELISAs) based on the sandwich principle (Life Diagnostics, Inc., catalog numbers 2110-2-N (Mb) and 2310-2-HS (H-FABP)).

A.2.2   Bolus injection experiments

Four able-bodied and four SCI rats were used for the bolus injection experiments. The animals were anaesthetised with 2-3 % isoflurane mixed with oxygen. Hairs of the right hindlimb were removed by shaving, after which the leg was cleaned with iodine and ethanol. Subsequently, 5 μg of purified rat H-FABP (0.2 g/L; Life Diagnostics, Inc.) was injected into the lateral saphenous vein using a 100 μL Hamilton syringe (Hamilton Company). The time course of the H-FABP concentration in serum after bolus injection was determined by taking blood samples at 5 min, 15 min, 30 min, 1 h, 2 h, 4 h, 8 h, and 24 h after bolus administration.

A.2.3   Compression experiments

At least two weeks after the bolus injection experiments, the TA muscle of the right hindlimb of four able-bodied and three SCI rats was compressed with an indenter for 6 h to measure the rise in Mb and H-FABP levels as a result of muscle damage. Changes in muscle structural integrity were monitored using T_2-weighted MRI, where an increase in T_2 was used as a measure of muscle pathology related to oedema, necrosis, and inflammation (Fleckenstein, 1996).

Three to four days prior to the compression experiments, blood and urine samples were obtained to establish the baseline concentrations of Mb and H-FABP. Before compression, the animals were anaesthetised with isoflurane (2-3 % for induction, 1-2 % for maintenance) mixed with oxygen, after which an MR-compatible loading device (figure A.1a) was tightly positioned around the hips of the animal. Cushions were used to support and constrain the leg during loading.
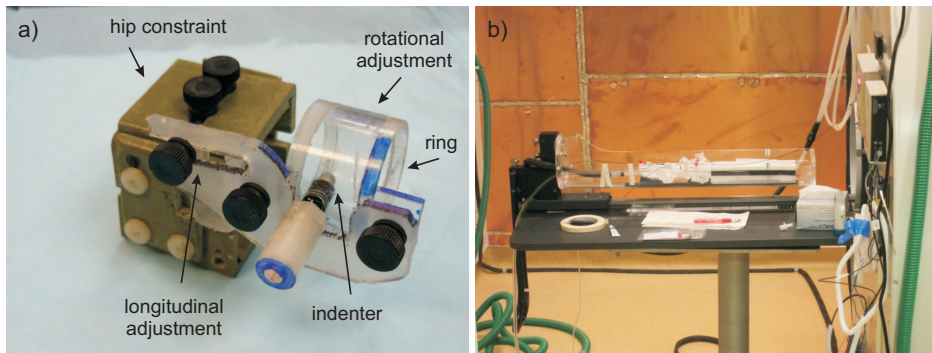

Figure A.1: Experimental setup for the compression experiments. a) MR-compatible loading device to compress the TA muscle of the right leg: the green part was used to tightly position the device around the hips of the animals with the right leg positioned through the ring. The location and angle of the indenter could be adjusted. b) Setup that was used to position the rats inside a 7.0 T MR scanner (Bruker ClinScan system).

The animal was placed supine in a setup that was used to position animals inside a 7.0 T MR scanner (Bruker ClinScan system), as shown in figure A.1b. T_2-weighted scout images were obtained (FOV = 80×80 mm^2, matrix size = 256×256, slice thickness = 1 mm, 17 slices, TR = 2.3 s, TE = 8.5 ms, NSA = 1) to adjust the indenter location and angle until it was positioned over the implant. A T_2 map of the legs before compression was obtained using a multi-echo spin echo sequence (FOV = 80×80 mm^2, matrix size = 256×256, slice thickness = 1 mm, 15 slices, TR = 2 s, TE = 11.1-44.4 ms, 4 echoes, NSA = 2). Subsequently, compression was applied by moving down the indenter until the thickness of the TA muscle underneath the indenter was 50 % reduced, as determined from scout images.

After the compression was applied, the animal was placed in a restraining jacket, and it was allowed to recover from anaesthesia. After 6 h compression, the indenter and restraining jacket were removed. Blood and urine samples were collected at 15 min before the removal of the indenter, and at 30 min, 2 h, 4 h, 6 h, 8 h, 12 h, 24 h, and 48 h after load removal. At 24 h after load removal, a T_2 map of the legs was obtained to assess the amount of damage caused by compression.

A.2.4   Data analysis

Quantitative T_2 maps were obtained by fitting the T_2-weighted signal intensity S to:

$$S = S_0 e^{-TE/T_2} \tag{A.1}$$

In the T_2 maps before compression, four consecutive slices around the implant were selected. In each slice, a region of interest (ROI) of 10×10 pixels was selected for both the left and the right leg in which the mean T_2 and standard deviation (SD) were determined. To define a threshold for significantly increased T_2 values, the mean $T_2 + 3 \times$ SD was calculated for each ROI and averaged over the legs and the four slices for each animal. Subsequently, this threshold was applied to the T_2 maps 24 h after load removal to identify areas with significantly increased T_2 values. The areas of muscle damage were then manually selected in each slice. The affected volume within the region of the T_2 maps was calculated as the volume of significantly increased T_2 within the region of the four MR slices. The total amount of damage per animal was then divided into three categories: none (no T_2 increase observed), small (0-50 mm³ with significant T_2 increase), and large (>500 mm³ with significant T_2 increase). The damage category of each animal was compared with the peak concentrations of Mb and H-FABP in serum and urine, where the peak concentrations were normalised to the maximum baseline concentration.

A.3   Results

A.3.1   Bolus injection experiments

The results of the bolus injection experiments are depicted in figure A.2. Three out of four able-bodied rats showed a rapid decrease in H-FABP serum concentration after bolus injection, and a slower decrease thereafter. A different pattern was observed for one able-bodied and three out of four SCI rats, consisting of a slow increase in serum concentration after bolus injection followed by a slow decrease. For the other SCI rat, also a slow decrease in H-FABP concentration was present.
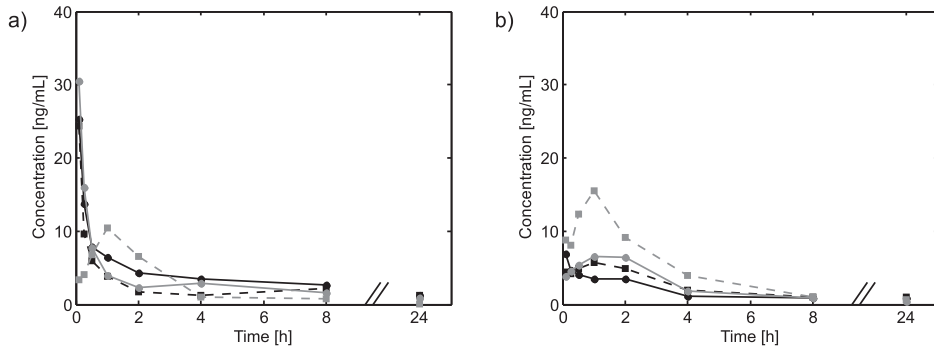
Figure A.2: Serum concentration of H-FABP after 5 μg injection of purified H-FABP in four able-bodied (a) and three SCI rats (b).

A.3.2   Compression experiments

Figure A.3 shows a transversal T_2 map for each animal 24 h after load removal. There were large differences in size of the affected region in the leg between the animals. In one animal (SCI 2), no region with significantly increased T_2 was observed. In three animals (AB 1, AB 4, and SCI 3), the affected volume was categorised as mild, and in the other three (AB 2, AB 3, and SCI 1), it was categorised as severe.
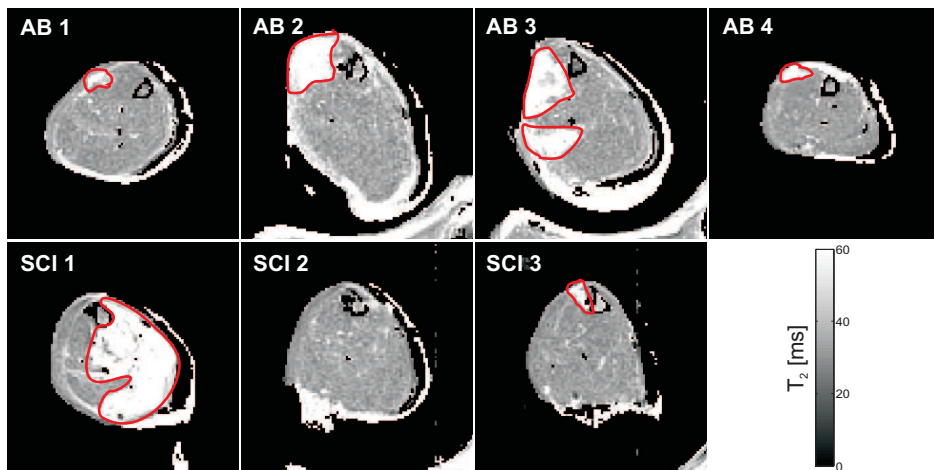

Figure A.3: Transversal T_2 maps for each animal 24 h after load removal. The affected region was manually selected (red line), and the pixels with significantly increased T_2 within this area were considered damaged.

The serum and urine concentrations of Mb and H-FABP after 6 h compression are shown in figure A.4 for the able-bodied rats, and in figure A.5 for the SCI rats. In general, a clear increase in Mb concentrations was observed after loading, whereas for H-FABP much smaller increases were present. Mb concentrations were already elevated before load removal, and peak levels occurred very rapidly after load removal (within 30 min to 2 h). Furthermore, Mb concentrations were much higher in urine than in serum.
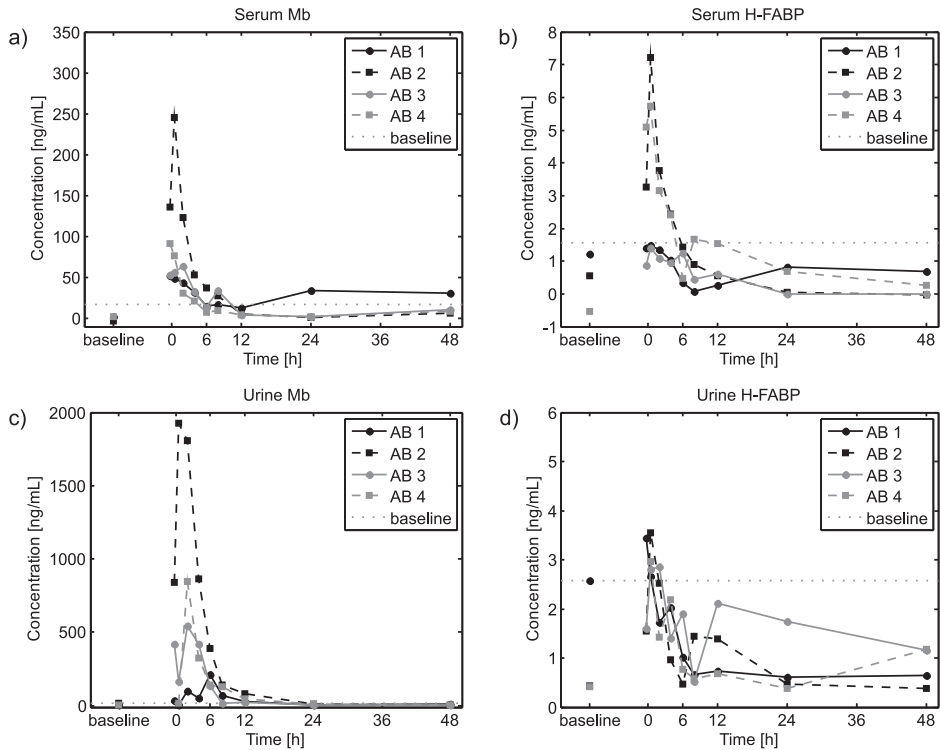

Figure A.4: Serum and urine concentrations of Mb and H-FABP for the able-bodied rats: a) Mb concentration in serum; b) H-FABP concentration in serum; c) Mb concentration in urine; d) H-FABP concentration in urine.
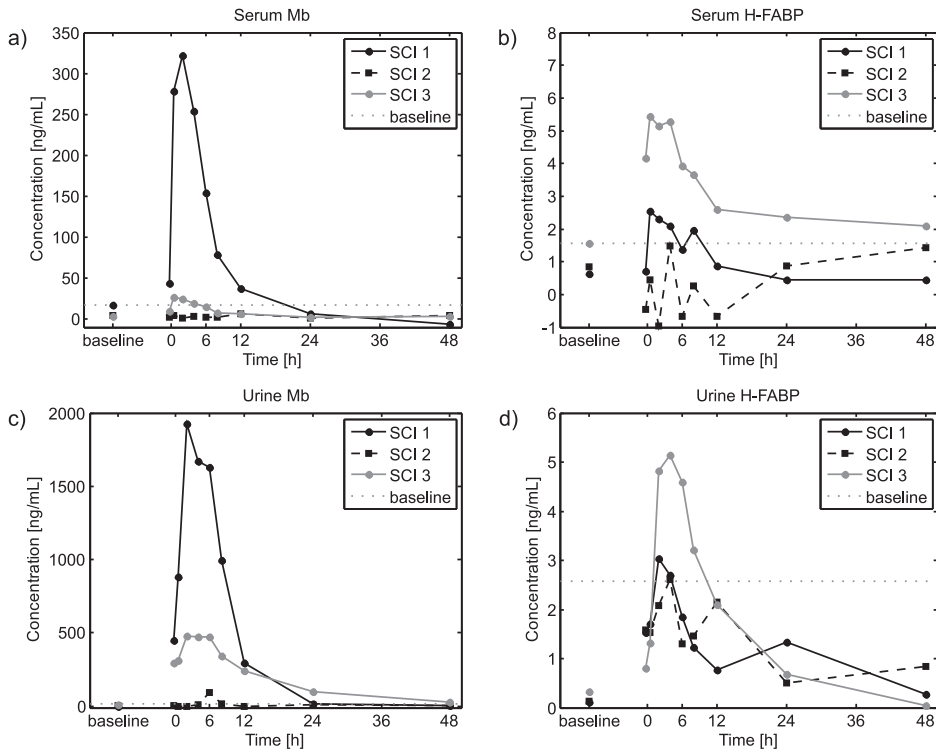
Figure A.5: Serum and urine concentrations of Mb and H-FABP for the SCI rats: a) Mb concentration in serum; b) H-FABP concentration in serum; c) Mb concentration in urine; d) H-FABP concentration in urine.

To investigate if there is a correlation between the volume of affected tissue and the increase in Mb and H-FABP concentrations, the peak concentrations in each damage category normalised to the maximum baseline concentration are shown in figure A.6. No clear increase for both proteins in serum and urine was observed for the animal without any damage. For Mb, the two highest peak levels in serum and urine were in animals with severe damage (figure A.6a,c). Also, Mb was more elevated with respect to baseline levels in urine than in serum. For H-FABP, much smaller increases with respect to baseline were present, which were also less related to the size of the affected region (figure A.6b,d).
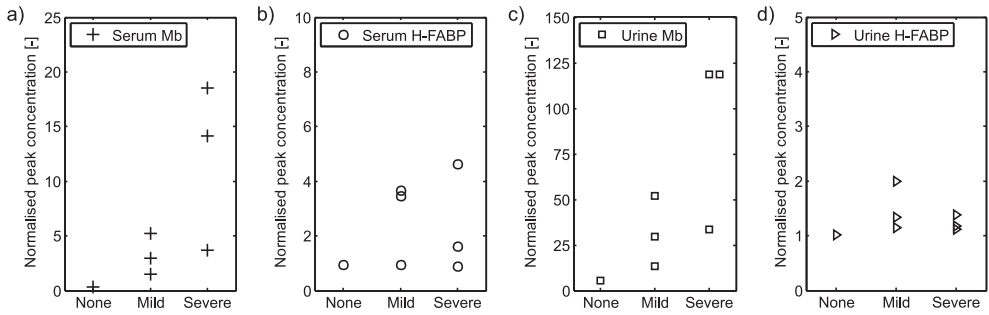
Figure A.6: Peak concentrations normalised to the maximum baseline concentration for: a) Mb in serum; b) H-FABP in serum; c) Mb in urine; d) H-FABP in urine.

A.4   Discussion

In the present pilot study, the suitability of Mb and H-FABP as early markers for DTI was investigated. For this, an animal model was used in which damage was created using an MR-compatible loading device. T_2-weighted MRI was used to assess the amount of damage in the tissue, which was compared with the serum and urine concentrations of both proteins after loading. There were large differences in the amount of damaged tissue between animals, and also in the resulting biomarker concentrations. In general, Mb was considerably increased after loading, whereas H-FABP concentrations hardly exceeded baseline levels. Moreover, Mb elevations were larger in urine than in serum.

The muscle damage that was created using the loading device was not limited to the TA muscle that was compressed by the indenter. Apparently, the cushions that were used to support and constrain the leg during loading were able to cause additional damage. Therefore, it is possible that tissue damage was not restricted to the region where the MRI acquisitions were applied, and the real amount of damage may have been larger than the values determined from the T_2 maps. For this reason, the amount of damage was not used quantitatively, but was divided into three categories.

Mb concentrations showed a large increase after loading, whereas H-FABP concentrations were hardly elevated. Therefore, H-FABP appeared to be a less sensitive marker for skeletal muscle damage when compared to Mb, which is probably due to the larger abundance of Mb with respect to H-FABP in skeletal muscle (Van Nieuwenhoven et al., 1995). In most animals, Mb concentrations were already elevated before load removal, indicating that part of the total release already occurred during loading. Peak levels occurred within 30 min to 2 h after load removal, after which concentrations remained elevated up to 6-12 h after load removal. Since the bolus injection experiments showed a much faster decrease in three out of four able-bodied rats, there may have been a continued release of

Mb during compression that caused the relatively long period of elevated concentrations. On the other hand, this longer period may also be a result of the high concentrations that were reached after compression, due to which renal clearance would take longer.

The peak serum and urine concentrations of both Mb and H-FABP were compared between the damage categories. For this, no distinction was made between able-bodied and SCI rats, due to the small number of animals. For H-FABP, only small deviations from baseline levels were observed, without any clear relation with the amount of damage. For Mb, a clear increase was observed in serum as well as in urine for both mild and severe damage. The largest peak concentrations occurred for two animals that were classified as severely damaged. Therefore, there might be a correlation between the amount of damage and the elevations in Mb concentrations in both serum and urine. This could, however, not be confirmed in the present study due to the small number of animals, and the inaccuracy related to the estimation of the damaged volume. Furthermore, the Mb peak levels were much larger in urine than in serum. From a clinical perspective, this is an important observation, since urine samples can be obtained noninvasively.

In summary, it was shown that Mb levels in serum and urine after 6 h compression are clearly elevated up to 6-12 h after load removal. H-FABP hardly showed any deviations from baseline. Therefore, Mb appeared to be a more sensitive marker for skeletal muscle damage than H-FABP. Additionally, Mb levels in urine reached much higher values than in serum. Since urine can be collected noninvasively, this is an important result that could be used in the design of future studies.

Acknowledgements

Appendix B

Modelling the kinetics of biomarkers

B.1   Background

The concentrations of biomarkers in the circulation are determined by the release of markers from the injured tissue and the clearance by the kidneys. Compartment models can be used to describe these kinetics. Subsequently, by measuring the marker concentrations after tissue damage in time, these models can be used to estimate the release of markers from injured tissue. Depending on the distribution volume of the protein under investigation, a one- or two-compartment model may be used (figure B.1). In the one-compartment model, it is assumed that the biomarkers are released into the circulation and subsequently cleared by the kidneys. In the two-compartment model, the extravascular space is included as an additional compartment. The parameters of the kinetic models can be determined with bolus injection experiments. In these experiments, a specific amount of protein is injected into the circulation. Subsequently, the decrease in concentration in time is measured to determine the parameters of the model.
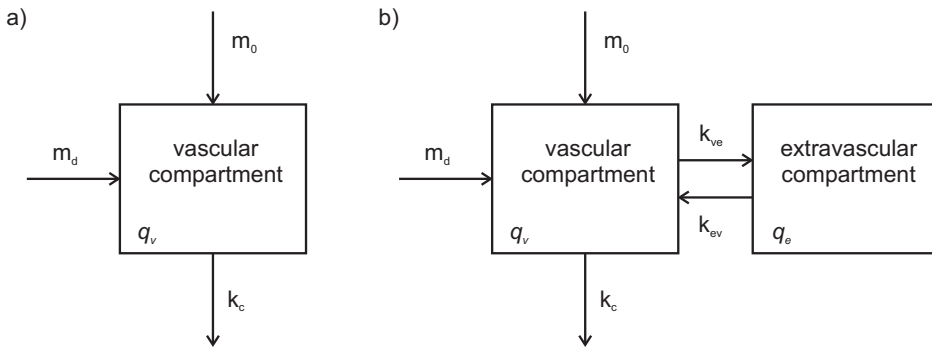

Figure B.1: a) One-compartment model to describe the kinetics of biomarkers. The quantity q_v of a protein in the circulation is determined by the release from the tissues, which consists of a baseline release m_0 and possibly an additional release m_d from a damaged area, and the clearance rate k_c by the kidneys. b) Two-compartment model to describe the kinetics of biomarkers. Here, the quantity q_e of the protein in the extravascular compartment and the exchange of proteins (with rates k_{ve} and k_{ev}) between the two compartments is included as well.

B.2   One-compartment model

To determine the parameters of the one-compartment model using bolus injection experiments, it is assumed that there is no release from a damaged area ($m_d = 0$). Furthermore, it is assumed that the baseline release of markers is constant in time. Then, the

differential equation for the amount of protein in the vascular compartment is:

$$\frac{dq_v(t)}{dt} = m_0 - k_c q_v(t) \tag{B.1}$$

This equation can be solved using the Laplace transform (indicated with a capital letter):

$$sQ_v(s) - q_v(0) = \frac{m_0}{s} - k_c Q_v(s) \tag{B.2}$$

By rewriting this equation, an analytical solution can be obtained:

$$(s + k_c)Q_v(s) = q_v(0) + \frac{m_0}{s} = \frac{sq_v(0) + m_0}{s} \tag{B.3}$$

$$\rightarrow \quad Q_v(s) = \frac{sq_v(0) + m_0}{(s + k_c)s} = \frac{A}{s + k_c} + \frac{B}{s} \tag{B.4}$$

The analytical solution of this equation is:

$$q_v(t) = Ae^{-k_c t} + B \tag{B.5}$$

Finally, with the following expression:

$$\frac{A}{s + k_c} + \frac{B}{s} = \frac{As + B(s + k_c)}{(s + k_c)s} = \frac{(A + B)s + Bk_c}{(s + k_c)s} \tag{B.6}$$

it can be derived that $A + B = q_v(0)$ and $Bk_c = m_0$. The model thus assumes a mono-exponential decay of the biomarker concentration in the circulation after the bolus injection. The parameters of the model can be determined by fitting the experimental results to equation B.5 to obtain parameters A, B, and k_c. From A and B, parameter $q_v(0)$ can be determined, and from B and k_c, parameter m_0 can be calculated.

B.3   Two-compartment model

The differential equations for the two-compartment model (figure B.1b) are:

$$\frac{dq_v(t)}{dt} = m_0 + k_{ev}q_e(t) - k_{ve}q_v(t) - k_c q_v(t) = m_0 + k_{ev}q_e(t) - (k_{ve}+k_e)q_v(t) \quad \text{(B.7)}$$

$$\frac{dq_e(t)}{dt} = k_{ve}q_v(t) - k_{ev}q_e(t) \quad \text{(B.8)}$$

With the assumptions of a constant baseline release m_0 and no release from damaged tissues ($m_d = 0$), the Laplace transform of equation B.7 is as follows:

$$sQ_v(s) - q_v(0) = \frac{m_0}{s} + k_{ev}Q_e(s) - (k_{ve}+k_c)Q_v(s) \quad \text{(B.9)}$$

For equation B.8, the Laplace transform reads:

$$sQ_e(s) - q_e(0) = k_{ve}Q_v(s) - k_{ev}Q_e(s) \quad \text{(B.10)}$$

$$\rightarrow \quad (s + k_{ev})Q_e(s) = q_e(0) + k_{ve}Q_v(s) \quad \text{(B.11)}$$

$$\rightarrow \quad Q_e(s) = \frac{q_e(0) + k_{ve}Q_v(s)}{s + k_{ev}} \quad \text{(B.12)}$$

By substituting $Q_e(s)$ in equation B.9 with the expression in equation B.12:

$$sQ_v(s) - q_v(0) = \frac{m_0}{s} + \frac{k_{ev}(q_e(0) + k_{ve}Q_v(s))}{s + k_{ev}} - (k_{ve}+k_c)Q_v(s) \quad \text{(B.13)}$$

$$\rightarrow \quad \left(s + k_{ve} + k_c - \frac{k_{ev}k_{ve}}{s + k_{ev}}\right)Q_v(s) = q_v(0) + \frac{m_0}{s} + \frac{k_{ev}q_e(0)}{s + k_{ev}} \quad \text{(B.14)}$$

the left side of equation B.14 can be written as:

$$\left(s + k_{ve} + k_c - \frac{k_{ev}k_{ve}}{s + k_{ev}}\right)Q_v(s) = \left(\frac{s^2 + (k_{ev}+k_{ve}+k_c)s + k_c k_{ev}}{s + k_{ev}}\right)Q_v(s) \quad \text{(B.15)}$$

The right side of equation B.14 is equal to:

$$q_v(0) + \frac{m_0}{s} + \frac{k_{ev}q_e(0)}{s + k_{ev}} = \frac{q_v(0)s^2 + (q_v(0)k_{ev} + m_0)s + m_0k_{ev} + k_{ev}q_e(0)}{s(s + k_{ev})} \tag{B.16}$$

Combining equations B.15 and B.16 leads to:

$$Q_v(s) = \frac{q_v(0)s^2 + (q_v(0)k_{ev} + m_0)s + m_0k_{ev} + k_{ev}q_e(0)}{s(s^2 + (k_{ev} + k_{ve} + k_c)s + k_ck_{ev})} \tag{B.17}$$

The denominator of this equation can also be written as:

$$s(s^2 + (\alpha + \beta)s + \alpha\beta) = s(s + \alpha)(s + \beta) \tag{B.18}$$

with:

$$k_{ev} + k_{ve} + k_c = \alpha + \beta \tag{B.19}$$

$$k_ck_{ev} = \alpha\beta \tag{B.20}$$

Using the following expression:

$$\frac{A}{s + \alpha} + \frac{B}{s + \beta} + \frac{C}{s} = \frac{(A + B + C)s^2 + (A\beta + B\alpha + C(\alpha + \beta))s + C\alpha\beta}{(s + \alpha)(s + \beta)s} \tag{B.21}$$

where:

$$q_v(0) = A + B + C \tag{B.22}$$

$$q_v(0)k_{ev} + m_0 = A\beta + B\alpha + C(\alpha + \beta) \tag{B.23}$$

$$m_0k_{ev} + k_{ev}q_e(0) = C\alpha\beta \tag{B.24}$$

the analytical solution of equation B.17 then reads:

$$q_v(t) = Ae^{-\alpha t} + Be^{-\beta t} + C \tag{B.25}$$

Thus, in the two-compartment model, a bi-exponential decay of the biomarker concentration in the circulation is assumed. Similar to the one-compartment model, the parameters of the two-compartment model can be determined by fitting experimental results to equation B.25 to obtain parameters A, B, C, α and β. Since there are five equations and six unknown parameters (k_c, k_{ve}, k_{ev}, m_0, $q_v(0)$, $q_e(0)$), an extra equation is needed. Therefore, based on the equilibrium situation (when $t \to \infty$) where the baseline release equals the baseline clearance, it was stated that:

$$m_0 = k_c C \tag{B.26}$$

From equation B.22, parameter $q_v(0)$ can be calculated. From equations B.20, B.26, and B.23 (in that order), parameter k_{ev} can be derived:

$$k_c = \frac{\alpha\beta}{k_{ev}} \tag{B.27}$$

$$\rightarrow \quad m_0 = k_c C = \frac{\alpha\beta C}{k_{ev}} \tag{B.28}$$

$$\rightarrow \quad q_v(0)k_{ev} + \frac{\alpha\beta C}{k_{ev}} = A\beta + B\alpha + C(\alpha + \beta) = D \tag{B.29}$$

$$\rightarrow \quad q_v(0)k_{ev}^2 - Dk_{ev} + \alpha\beta C = 0 \tag{B.30}$$

This results in two solutions for parameter k_{ev}:

$$k_{ev,1,2} = \frac{D \pm \sqrt{(-D)^2 - 4q_v(0)\alpha\beta C}}{2q_v(0)} \tag{B.31}$$

With both solutions for k_{ev}, the other parameters can be determined. From equation B.20, parameter k_c can be calculated:

$$k_c = \frac{\alpha\beta}{k_{ev}} \tag{B.32}$$

Subsequently, from equation B.19, parameter k_{ve} can be determined:

$$k_{ve} = \alpha + \beta - k_{ev} - k_c \tag{B.33}$$

Parameter m_0 is derived from equation B.23:

$$m_0 = A\beta + B\alpha + C(\alpha + \beta) - q_v(0)k_{ev} \tag{B.34}$$

Finally, equation B.24 is used to determine $q_e(0)$:

$$q_e(0) = \frac{C\alpha\beta - m_0 k_{ev}}{k_{ev}} \tag{B.35}$$

Now, two sets of solutions have been obtained, depending on the value of k_{ev}. Since usually one of the two sets contains unrealistic (negative) values, it is easy to decide upon which set contains the best estimation of the parameters.

B.4   Application to experimental data

As an example, both the one- and two-compartment models were fitted to the experimental data of three rats in which 5 μg heart-type fatty acid binding protein (H-FABP) was injected into the lateral saphenous vein, as described in appendix A. The time course of the H-FABP concentration in serum was determined at 5 min, 15 min, 30 min, 1 h, 2 h, 4 h, 8 h, and 24 h after injection. To estimate the kinetic parameters, the measured concentrations were converted to quantities. For this, it was assumed that the serum volume of Sprague-Dawley rats was similar to the plasma volume, equal to 4.86 mL/100 g body weight (Probst et al., 2006), and that the protein was equally distributed over the total volume.

The experimental results for each of the rats are shown in figure B.2, together with the model fits. For each rat, the two-compartment model resulted in a better fit of the results than the one-compartment model, indicating that the H-FABP concentration follows a bi-exponential decay after bolus injection.
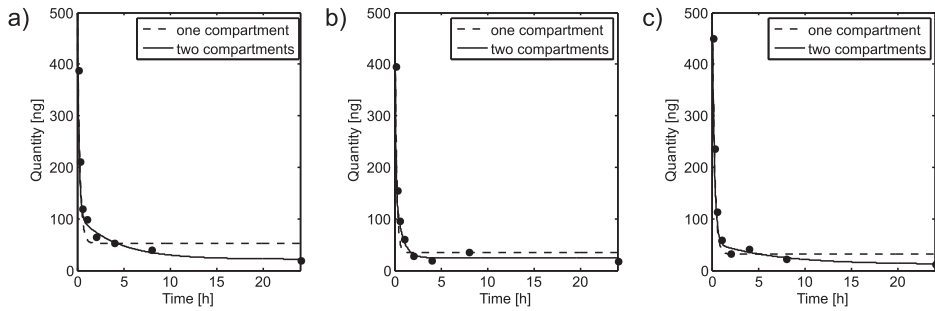
Figure B.2: Experimental results of rat 1 (a), 2 (b), and 3 (c) after H-FABP bolus injection. The results were fitted with both the one- (dashed) and two-compartment (solid) models.

The parameter values that were derived from the model fits are displayed in table B.1. Large differences are present between the results of the one- and two-compartment model, and also between the different rats. In future research, the sensitivity of the model results for the individual parameter values should be investigated, as well as the influence of the model fit on the estimated parameter values.

Table B.1: Parameter values of the one- and two-compartment models and the R^2 value of the model fits.

	$q_v(0)$ [ng]	$q_e(0)$ [ng]	m_0 [ng h^{-1}]	k_c [h^{-1}]	k_{ve} [h^{-1}]	k_{ev} [h^{-1}]	R^2 [-]
rat 1, one-comp.	509	-	205	3.9	-	-	0.971
rat 1, two-comp.	564	0	23	1.1	3.7	1.2	0.998
rat 2, one-comp.	605	-	198	5.6	-	-	0.980
rat 2, two-comp.	899	0	130	5.4	5.8	3.8	0.998
rat 3, one-comp.	613	-	128	4.0	-	-	0.994
rat 3, two-comp.	632	0	16	1.3	2.8	0.5	0.999

Dankwoord

Er zijn veel mensen die ik graag wil bedanken voor hun bijdrage aan dit proefschrift. Cees, ik wil je hartelijk bedanken voor de begeleiding de afgelopen vier jaar. Ik heb jouw nuchtere en positieve blik op mijn werk altijd erg gewaardeerd, en daar kan ik waarschijnlijk nog veel van leren. Ik vond het fijn dat jouw deur altijd open stond. Frank, bedankt voor de vrijheid die je me gegeven hebt om mijn eigen gang te gaan. Dan, I would like to thank you very much for all the discussions that we had, and of course for your excellent improvements and corrections of my English (I will never ask about prepositions again). Klaas, bedankt voor je kritische blik op mijn werk. Gustav, bedankt voor alle hulp tijdens de MRI-metingen. I would also like to thank Arthur Mak (The Hong Kong Polytechnic University), Vivian Mushahwar (University of Alberta), and Aart Nederveen (AMC Amsterdam) for taking place in my committee.

Anke, bedankt voor de leuke samenwerking tijdens de eerste twee jaar van mijn promotie. Ik heb veel van je geleerd, vooral als het op experimenteel werk aankomt, en ik ben blij dat ik jouw opstelling heb kunnen gebruiken om nieuwe experimenten mee te doen. Karlien, ik vond het fijn dat ik aan het begin van mijn promotie meteen met jouw numerieke model aan de slag kon.

Jo en Leonie, zonder jullie hulp had ik de experimenten die beschreven staan in hoofdstuk 4 en 5 niet kunnen uitvoeren. Ik weet dat deze experimenten niet altijd op ideale tijdstippen plaatsvonden, dus ik heb het zeer gewaardeerd dat jullie altijd voor me klaar stonden. Koo, bedankt dat ik voor al mijn vragen over statistiek bij jou terecht kon.

Ik wil mijn kamergenootjes van WH 4.108 ook graag bedanken voor de gezelligheid de afgelopen jaren. Lieke, ik vond het heel prettig dat we ons proefschrift tegelijkertijd hebben afgerond waardoor we de laatste drukke maanden allebei veel tijd op de TU doorbrachten. Het is toch fijner als je niet de enige bent. Mieke, ik heb veel bewondering voor jouw doorzettingsvermogen. Ik wens je veel succes en geluk toe. Petra, jij ook veel

succes met het afronden van je promotie en uiteraard met fietsen. Daarnaast wil ik ook de andere collega's van vloer 4 bedanken voor de gezellige koffiepauzes en de prettige werksfeer.

Tijdens mijn promotie heb ik veel mogelijkheden gehad om te reizen en met andere groepen samen te werken. Vivian and Leandro, I enjoyed our cooperation in which we combined your experimental work and our numerical work, which has resulted in chapter 6 of this thesis. I would also like to thank the department of Physical Therapy and Human Movement Sciences of Northwestern University for the opportunity to spend three months of my PhD in Chicago. Thanks to all the Chicago colleagues (Jules, Mohsen, Amanda, Mauli, Daniel, Charmi, Yagna, Atek, Chris, and Sam) for helping with the experiments or for showing me some nice places in Chicago. A special thanks goes to Charmi and Yagna for the frozen yogurt and kitchen field trips.

De afgelopen jaren heb ik veel studenten mogen begeleiden tijdens hun stages. Agnese, Anne, Emmy, Tim, Yabin, Merel, and Alex, thank you for the work that you did that directly or indirectly contributed to this thesis. Verder heb ik ook een aantal afstudeerders mogen begeleiden. Thomas, I really appreciated the large amount of work that you did for your master's thesis during your relatively short stay in Eindhoven. It's nice to meet up again at conferences. Emmy, bedankt voor jouw grote bijdrage aan hoofdstuk 4 en 5. Ik ben blij dat jij voor je afstuderen experimenteel werk wilde doen, anders was ik er misschien wel nooit aan begonnen. Ik ben blij dat ik de experimenten samen met jou heb kunnen doen. Elise, bedankt voor jouw grote bijdrage aan hoofdstuk 7. Er bleek bij jouw afstudeeropdracht toch wel meer te komen kijken dan we van tevoren verwacht hadden. Ik heb veel bewondering voor de manier waarop je alles aangepakt en geregeld hebt. Verder wil ik ook graag alle vrijwilligers bedanken die aan deze studie hebben meegewerkt.

Verder wil ik Caroline, Edith, Evelinda, Greetje, Lieke, Linda, Loes, Petra, en Willemijn bedanken voor de gezellige activiteiten en de jaarlijkse weekendjes. Ook de mensen van korfbalvereniging Rust Roest wil ik graag bedanken voor de gezelligheid. Mark en Denise, fijn dat jullie mijn broertje en zusje zijn. Ik vind het leuk dat jullie ook mijn paranimfen willen zijn. Papa en mama, bedankt voor de mogelijkheden die jullie me altijd gegeven hebben. En ook bedankt voor alle reisjes naar de zon. Hans, Lucie, Suzanne, Lonneke, en Koen, jullie zijn intussen wel een soort tweede 'thuis' voor mij geworden. Bedankt voor alle gezelligheid. Lieve Bart, bedankt voor al je begrip, hulp, steun, liefde en gezelligheid. Ik vind het heel fijn dat jij altijd voor me klaar staat!

Sandra,
Eindhoven, juli 2011

Curriculum vitae

Sandra Loerakker is geboren op 14 december 1982 in Alkmaar. In 2001 behaalde zij haar VWO diploma aan het Koningin Wilhelmina College in Culemborg. Aansluitend studeerde zij Biomedische Technologie aan de Technische Universiteit Eindhoven. Tijdens haar studie heeft zij stage gelopen aan het Texas Heart Institute in Houston, USA, waar zij onderzoek deed naar het effect van mechanische ondersteuning van het hart op de circulatie. Haar afstudeerwerk richtte zich op het ontwikkelen van een numeriek model waarmee de vloeistofstroming in het hart en de veranderingen hierin tijdens ziekte en mechanische ondersteuning bestudeerd kunnen worden. Na haar afstuderen in 2007, cum laude, besloot zij promotieonderzoek te doen binnen het decubitusonderzoek van de faculteit Biomedische Technologie van de Technische Universiteit Eindhoven, resulterend in dit proefschrift. Als onderdeel van haar promotie heeft zij drie maanden onderzoek gedaan aan Northwestern University, Chicago, USA.

List of publications

- S. Loerakker, E.S. Huisman, H.A.M. Seelen, J.F.C. Glatz, F.P.T. Baaijens, C.W.J. Oomens, D.L. Bader. Plasma variations of biochemical markers for deep pressure ulcers in able-bodied and spinal cord injured subjects. *Submitted.*

- S. Loerakker, L.R. Solis, D.L. Bader, F.P.T. Baaijens, V.K. Mushahwar, C.W.J. Oomens. How does muscle stiffness affect the internal deformations within the soft tissue layers of the buttocks under constant loading? *Submitted.*

- S. Loerakker, D.L. Bader, F.P.T. Baaijens, C.W.J. Oomens. Which factors influence the ability of a computational model to predict the in vivo deformation behaviour of skeletal muscle? *Submitted.*

- S. Loerakker, E. Manders, G.J. Strijkers, K. Nicolay, F.P.T. Baaijens, D.L. Bader, C.W.J. Oomens. The effects of deformation, ischemia, and reperfusion on the development of muscle damage during prolonged loading. *Journal of Applied Physiology*, in press.

- S. Loerakker, C.W.J Oomens, E. Manders, T. Schakel, D.L. Bader, F.P.T. Baaijens, K. Nicolay, G.J. Strijkers. Ischemia-reperfusion injury in rat skeletal muscle assessed with T_2-weighted and dynamic contrast-enhanced MRI. *Magnetic Resonance in Medicine*, doi: 10.1002/mrm.22801.

- S. Loerakker, A. Stekelenburg, G.J. Strijkers, J.J.M. Rijpkema, F.P.T. Baaijens, D.L. Bader, K. Nicolay, C.W.J. Oomens. Temporal effects of mechanical loading on deformation-induced damage in skeletal muscle tissue. *Annals of Biomedical Engineering*, 38(8):2577-2587, 2010.

- C.W.J. Oomens, S. Loerakker, D.L. Bader. The importance of internal strain as opposed to interface pressure in the prevention of pressure related deep tissue injury. *Journal of Tissue Viability*, 19(2):35-42, 2009.

- B.J. van Nierop, A. Stekelenburg, S. Loerakker, C.W. Oomens, D. Bader, G.J. Strijkers, K. Nicolay. Diffusion of water in skeletal muscle is not influenced by compression in a rat model of deep tissue injury. *Journal of Biomechanics*, 43(3):570-575, 2009.

- L.G.E. Cox, S. Loerakker, M.C.M. Rutten, B.A.J.M. de Mol, F.N. van de Vosse. A mathematical model to evaluate control strategies for mechanical circulatory support. *Artificial Organs*, 33(8):593-603, 2009.

- T. Nagel, S. Loerakker, C.W.J. Oomens. A theoretical model to study the effects of cellular stiffening on the damage evolution in deep tissue injury. *Computer Methods in Biomechanics and Biomedical Engineering*, 12(5):585-597, 2009.

- K.K. Ceelen, A. Stekelenburg, S. Loerakker, G.J. Strijkers, D.L. Bader, K. Nicolay, F.P.T. Baaijens, C.W.J. Oomens. Compression-induced damage and internal tissue strains are related. *Journal of Biomechanics*, 41(16):3399-3404, 2008.

- S. Loerakker, L.G.E. Cox, G.J.F. van Heijst, B.A.J.M. de Mol, F.N. van de Vosse. Influence of dilated cardiomyopathy and a left ventricular assist device on vortex dynamics in the left ventricle. *Computer Methods in Biomechanics and Biomedical Engineering*, 11(6):649-660, 2008.